SAPIENZA
UNIVERSITÀ DI ROMA

Ph.D. Course in Mathematical Models for
Engineering, Electromagnetics and Nanosciences

Curriculum in Materials Science

Cycle XXIX

"Investigation of the reactivity of Li- and Na- alanates as conversion anodes for lithium ion batteries"

Supervisor: prof. Stefania Panero

Co-supervisor: dr. Priscilla Reale

Ph.D. student: Laura Silvestri

Once you eliminate the impossible, whatever remains, no matter how improbable, must be the truth.

Arthur Conan Doyle

Index

INTRODUCTION

Lithium ion batteries (LIBs) are lightweight and compact devices, exhibiting operating voltages of the order of 4 V and specific energy ranging between 100 $Whkg^{-1}$ and 150 $Whkg^{-1}$. Current commercial LIBs basically consist of a cathode formed by a lithium metal oxide ($LiMO_2$, e.g. $LiCoO_2$), an anode typically formed by graphite, and an electrolyte consisting of a solution of a lithium salt (e.g. $LiPF_6$) in a mixed organic solvent (e.g. ethylene carbonate-dimethyl carbonate, EC-DMC) embedded in a separator felt (figure 1). The separator prevents the electrical contact between the electrodes and, at the same time, it allows the diffusion of Li-ions from cathode to anode during the charging and the reverse discharging process. In this way, when the battery is charging, Li de-intercalates from the cathode and intercalates into the anode. Conversely, Li intercalates into the cathode via the electrolyte upon discharging. During charge/discharge, Li ions flow between the anode and the cathode, enabling the conversion of chemical energy into electrical energy and the storage of electrochemical energy within the battery. The chemical reactions involved in a typical LIB cell can be described as follows:

Anode: $6C + xLi^+ + xe^- \leftrightarrows Li_xC_6$

Cathode: $LiCoO_2 \leftrightarrows Li_{(1-x)}CoO_2 + xLi^+ + xe^-$

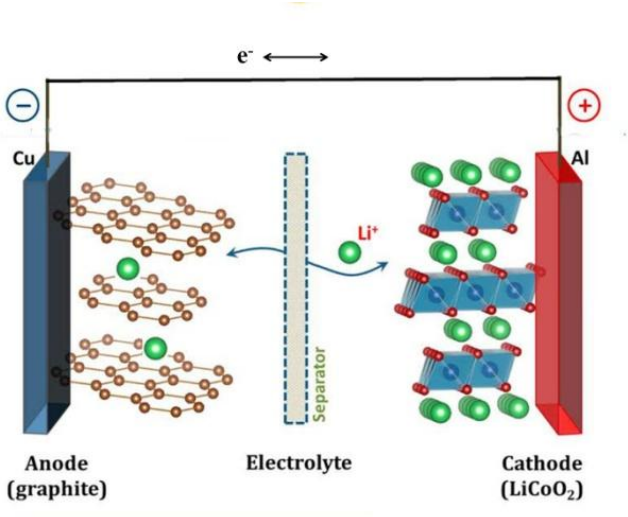

Figure 1. Schematic illustration of a typical Li-ion battery ($LiCoO_2/Li^+$ electrolyte/graphite).

Rechargeable lithium-ion batteries (LIBs) have been considered as the most promising energy storage system for a wide variety of applications. Hitherto, their use is limited to the field of electronic portable devices. For instance, they are commonly used to power laptop, mobile phones, digital cameras etc. To extend their use to power hybrid or electric vehicles and to

storage clean energy, these systems require further improvements in terms of energy density, cycle life performance and safety hazards.

The adopted strategies for improving the technology of Li-ion devices are basically focused on modifying the chemical nature of its main components. While many high-voltage and/or safer positive electrode materials have been successfully developed and commercialized in the last years, such as $LiNi_{0.8}Co_{0.15}Al_{0.05}O_2$, carbon-coated nano-$LiFePO_4$ and $LiNi_{1/3}Co_{1/3}Mn_{1/3}O_2$, the replacement of the carbon graphite negative electrode has been relatively less successful [1].

Graphite has the advantage of high electronic conductivity, low cost and abundance, a good capacity retention and very good cycle life. However, graphite allows the intercalation of only one Li-ion every six carbon atoms, with a resulting stoichiometry of LiC_6 and thus an equivalent reversible capacity of 372 $mAhg^{-1}$. In addition, the diffusion rate of lithium into carbon materials is between 10^{-12} and 10^{-6} cm^2s^{-1} (for graphite it is between 10^{-9} and 10^{-7} cm^2s^{-1}), which results in batteries with low power density [2]. Recently, Sony has prompted an interest in the Sn-Co-C alloy composite anode and is now manufacturing this new generation of Li-ion batteries called Nexelion^{TM}. This battery leads to much higher gravimetric and volumetric capacities but to a lower long-term reversibility compared to graphite. Sony reported a capacity increase of about 30% compared to their conventional battery, good rate capability and good temperature performance. Other companies, such as Toshiba, chose a safer and "zero-strain" insertion anode material, the nano $Li_4Ti_5O_{12}$ (LTO) in the super-charge ion battery (SCiB^{TM}) with an output voltage of 2.4 V. LTO has a very good cycle life and high rate capability that allows quick charge/discharges. In addition, its high delithiation voltage (1.5 V vs. Li/Li^+) makes it safer than other anode materials; indeed, there is no risk of lithium plating and presumably no SEI formation. However, its drawback is the low theoretical specific capacity (175 $mAhg^{-1}$/612 mAh mL^{-1}) and the low deliverable power linked to the high lithium insertion voltage [1]. Another alternative to the common anode material is to use elements, preferably nanometric in size, that can alloy with lithium, such as aluminum, silicon, or tin, capable to provide high specific capacities theoretically ranging from 1000 to 4000 $mAhg^{-1}$. However, there is a large volume change between their unlithiated and their lithiated state: 100 % for LiAl, 300-400 % for Li_xSi (x=3.5 or 4.2), and 260% for $Li_{4.4}Sn$. That gives rise to mechanical stresses that lead to cracks, eventual disintegration of the electrode, and failure of the Li-ion batteries [1]. Seeking other examples of reactions in the solid state that are not constrained by the requirements of intercalation, it has been shown that lithium can react with a range of transition-metal oxides by a process

termed conversion. The full electrochemical reduction of such oxides versus lithium, involves two or more electrons per 3*d*-metal and lead to composite materials consisting of nanometric-scale metallic clusters dispersed in an amorphous Li_2O matrix. Owing to the nanocomposite nature of these electrodes, these conversion reactions are highly reversible, providing large capacities that can be maintained for hundreds of cycles [3]. The conversion reaction turns out to be widespread; since the original discovery, many other examples of conversion reactions including sulfides, nitrides, fluorides, and phosphides have been reported. They have been shown to involve, depending on the oxidation state of the 3d metal, one (Cu_2O), two (CoO), three (Fe_2O_3), or four (RuO_2) electrons per 3d metal, thus offering the possibility of achieving negative electrodes with high capacity improvements over the existing ones. Another advantage of such conversion reactions lies in the internally nanostructured character of the electrode that is created during the first electrochemical reduction. Because of the internal nanostructure rather than individual nanoparticles, low-packing densities associated with the latter do not exist. Furthermore, the chemical versatility of such conversion reactions provides a unique opportunity to control the redox potential by tuning the electronegativity of the anion. A major drawback of conversion reactions is their poor kinetics (that is, the rate at which lithium ions and electrons can reach the interfacial regions within the nanoparticle and react with the active domains). This drawback manifests itself as a large separation of the voltage on charge and discharge, implying poor energy efficiency of the electrodes. This polarization may be associated with the energy barrier to trigger the breaking of the M-X bonds and was shown to be sensitive to the nature of the anion, for example decreasing from $\Delta E \approx 0.9$ V to ≈ 0.4 V on moving from an oxide to a phosphide [4].

Following chapters describes the main features of conversion materials and the factors that influence their performance. In particular, the focus is on the behavior of metal hydrides as conversion anodes for lithium batteries. Finally, in the last chapter is reported an introduction of sodium and lithium alanates, which are the subjects of this dissertation.

1

Conversion materials for electrochemical application

In 2000, Poizot et al. [5] for the first time reported that lithium can be stored reversibly in transition metal oxides through a heterogeneous conversion reaction:

$$M_xO_y + 2yLi^+ + 2ye^- \leftrightarrows yLi_2O + xM^0 \qquad (1)$$

where M is Co, Fe, Ni, and Cu [6].

The mechanism of the reaction with lithium of these metal oxides differs considerably from the classical mechanisms, which are based either on reversible insertion/de-insertion of lithium into host structures or on lithium alloying reactions. This difference is due to the fact that most of these materials crystallize in a rock-salt structure that does not contain any available empty sites for Li ions, and also that none of the 3d metals considered forms alloys with Li [4].

According to reaction 1, this conversion reaction implies the reversible formation and decomposition of Li_2O. While the formation of Li_2O is thermodynamically feasible, the ability to drive its decomposition electrochemically is surprising. Indeed, Li_2O has always been reported to be electrochemically inactive. In this case, reversibility seems to lie in the internally nanostructured character of the electrode that is created during the first electrochemical reduction. On this basis, the electrochemically driven size confinement of the metal particles is thus believed to enhance their electrochemical activity towards the formation/decomposition of Li_2O. With decreasing particle size, an increasing proportion of the total number of atoms lies near or on the surface making the electrochemical reactivity of the particles more and more important [5].

Since the original discovery, many other examples of conversion reactions including sulfides, nitrides, fluorides, phosphides etc… have been reported [7–10]. The reaction (1) can be generalized as follow:

$$M_aX_b + (b{\cdot}n)\ Li \leftrightarrows aM^0 + bLi_nX \qquad (2)$$

Where M is the transition metal, X is O, N, F, S, P and H and *n* the formal oxidation state of X [11].

The main advantage of such conversion mechanism is the high capacity improvements provided by the exchange of more than one electron to reduce a formula unit of oxidized transition metal to the metallic state. Furthermore, such conversion reactions offer numerous opportunities to 'tune' the voltage and capacity of the cell owing to the fact that the cell potential is directly linked to the strength of the M–X bonding. Weaker M–X bonding gives larger potentials. The theoretical capacity is directly linked to the oxidation state of the transition metal in the M_aX_b starting material and can be formally as high as $b \cdot n$ (*n* being the formal charge of the ligand). Thus, by selecting the nature of M and its oxidation state, as well as the nature of the anion, one can obtain reactions with a specific potential within the range 0 to 3.5 V, and based on low-cost elements such as Mn or Fe [12].

However several issues, mostly connected to reaction mechanism, affect these conversion materials and constitute an obstacle to the practical implementation of conversion electrode materials in commercial batteries. The most relevant regard i) the strong structural re-organization that take place to accommodate the chemical transformations induces large volume changes that, as in the case of the alloys, result in particle decohesion and unsatisfactory cycling performance, ii) a large voltage hysteresis is observed between the discharge and recharge steps, iii) a large Coulombic inefficiency occurs in the first cycle [11].

1.1 Characteristic performance of conversion materials

Figure 1.1 show the typical voltage profile of a conversion material highlighting the issues correlated with the displacement reaction mechanism.

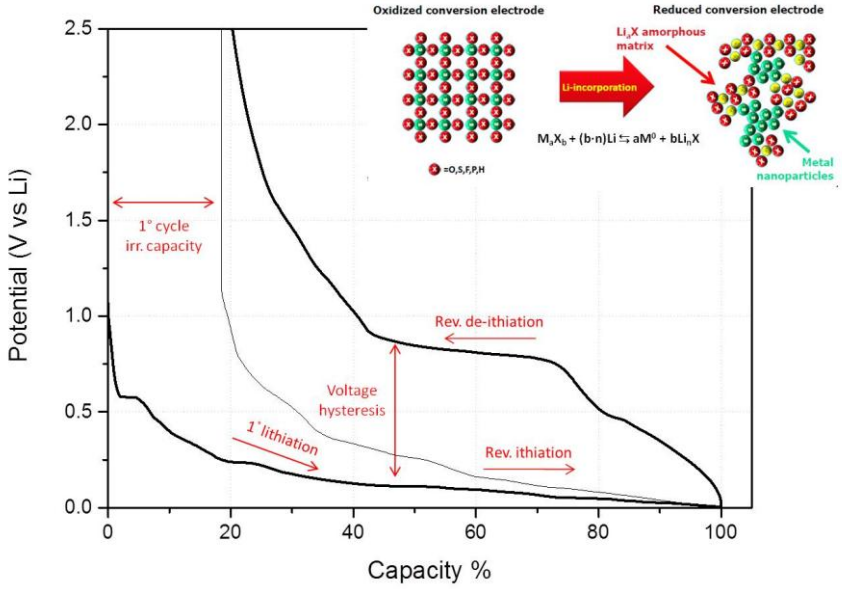

Figure 1.1 - Example of voltage profile obtained with a half-cell made of a lithium metal counter electrode and a conversion working electrode.

Typically, first discharge exhibits an extended conversion plateau and it is characterized by a large experimental potential deviation from the theoretical value. This energy penalty is required to transform the microsized starting electrode into a nanosized discharged electrode $aM^0 + bLi_nX$. After the first cycle, however, the M_aX_b material remains in nanosized form rather than returning to the microsized morphology. The latter explains why the first lithiation (discharge) exhibits, almost without exception, a different voltage pattern than the next lithiations [11]. In fact, after first discharge, oxidation exhibits a much less defined plateau and it is replaced by a mostly sloping curve.

The result is a relatively wide gap between the charge and discharge voltages (figure 1.1). In all cases, this gap persists at several hundreds of mV even when the kinetics is slowed down to rates as low as C/100 [13]. This hysteresis of conversion electrode materials range from several hundred mV to ~2 V, comparable to that of a Li-O_2 battery but much higher than that of a Li-S battery (200−300 mV) or a typical intercalation electrode material (several tens mV)

at similar rates. It leads to a high degree of round-trip energy inefficiency (< 80% energy efficiency) that is unacceptable in practical applications [14].

So far, various authors have recognized one rule as regards the extent of hysteresis: it depends on the nature of the M-X chemical bonds in the starting material (ionic vs. covalent) which is directly linked to the material electronic behavior [15]. Its magnitude has been found to increase with the electronegativity of the anion and decrease with the increasing ionic conductivity of the lithiated matrix. This effect is more prominent in the first cycle, which seems to be related to the high crystallinity of the pristine material with respect to the amorphous nature of the binary compound formed after the first re-oxidation [13,15]. Recently, Li et al. [14] reported a study on iron fluoride (FeF_3), to explore the origin of voltage hysteresis on conversion materials. By integrating experimental and theoretical simulation results, they identified three components that contribute to the voltage hysteresis. The first one is the iR voltage drop, which is the sudden voltage jump after the current is removed (i.e. < 100 mV for FeF_3). The second component is the reaction overpotential that is required to nucleate and grow new phases, drive mass transport, and overcome the interfacial penalty for making nanophases. The third component that leads to the hysteresis is the difference in spatial distribution of electrochemically active phases during discharge and charge as well as the way these phases are connected in the electrochemical system (i.e. access to Li^+ and electron) [14].

1.2 Efficiency of the conversion process

Usually, conversion materials show specific capacity recovered upon the first charge (i.e., the Coulombic efficiency) drastically lower than that generated upon discharge. In the best of cases, the efficiency can approach 80%, but it can easily be as low as 40%, with the typical range being between 60% and 75%. Exceptions are RuO_2 and some metal fluorides such as FeF_3 [11]. Three causes for Coulombic inefficiency can be envisaged: i) irreversible or non-electrochemical electrolyte decomposition, ii) incomplete de-conversion due to the presence of inactive or electrically disconnected Li_nX/M regions, and iii) incomplete de-conversion to the initial binary compound, but to other lower phases. The latter has been observed, for instance, in the case of Co_3O_4, CuO, or NiS, in which lower formal oxidation states of the metal (i.e., CoO, Cu_2O, and Ni_3S_2, respectively) are observed upon the first charge. The Coulombic efficiencies are remarkably improved beyond the first cycle, with the values close to 100% in a variety of cases. An argument could be made that this improvement could be explained thanks to an increased yield of the conversion reaction after an initial, formatting cycle of the electrode into nanoparticles, yet first cycle losses are observed even when the initial electrode material is already in the form of nanoparticles [11].

1.3 Improvements of electrochemical performance

An important obstacle in the way toward application of this type of electrodes is certainly cycle life. The conversion processes entail massive structural reorganization and volumetric changes (for instance, 100% for Cr_2O_3 to Cr/Li_2O). These changes can lead to particle isolation and cracking as a result of electrode grinding, and to a subsequent fading of the capacity after a few cycles. Attempts to address this issue through the engineering of the electrode have been made for conversion reaction materials, using a number of strategies such as forming nanocomposites with a considerable proportion of carbon or increasing the amount of polymeric binder [11]. In general, these approaches result in remarkable improvements, indicating that an opportune amount of carbon coupled with adequate choice of binder might be a suitable baseline strategy for conversion-based electrodes. Also, multiple efforts have been directed toward solving the cycle life problem through the nanoscale tailoring of the initial M_aX_b particles. The use of engineered nanoparticles may not only offer the advantage of shortening diffusion paths for lithium, resulting in enhanced capacity and rate capability in the first few cycles, but it may also by-pass or at least limit the first cycle textural formatting. In parallel, several researchers have proposed the use of integrated nanostructured electrodes, in which the active phases are grown on metallic foams, nanopillared and foil substrates. These designs allow for the improvement and preservation of the substrate material contact, resulting not only in better cycling stabilities, but also enhanced rate capabilities [11].

2

Metal hydrides as high capacity anodes for lithium ion batteries

Oumellal et al. [16] reported for the first time that MgH_2 can react electrochemically with lithium according to the following reaction:

$$MgH_2 + 2Li^+ + 2e^- \leftrightarrows 2LiH + Mg \qquad (1)$$

MgH_2 was investigated thanks to its high theoretical capacity versus Li^+/Li^0 ($2e^-$ per unit formula, that is 2038 $AhKg^{-1}$, 2878 Ahl^{-1}) and both high gravimetric (7.6 wt.%) and volumetric capacities (108g H_2/l) for H_2 [16]. Compared to other conversion compounds, MgH_2 exhibits remarkable properties such as the high capacities values in a safe potential window of 0.1-0.5 V versus Li^+/Li^0 and the lowest polarization ever reported for conversion reactions electrodes. For example, the measured charge/discharge polarization (ΔV) for MgH_2 is $\approx$ 0.25 V in comparison to ΔV for fluorides, oxides, sulphides, nitrides and phosphides is $\approx$ 1.1 V, $\approx$ 0.9 V, $\approx$ 0.7 V, $\approx$ 0.6 V and $\approx$ 0.4 V, respectively. This result has been rationalized by the fact that the mobility of the ionic species in the solid state is, among other chemical/physical parameters, mainly governed by the electronegativity and polarizability of the anion species. Bearing in mind these considerations, H^- species are expected to diffuse faster than the O^{2-} or F^- ones, enabling faster transport and therefore a lower polarization [16].

This discover opened the way for a series of studies on hydrides as high capacity anodes for lithium ion batteries either on binary and ternary hydrides. The reversible lithium-controlled conversion reaction mechanism of MgH_2, can be extended to others hydrides and generalized as:

$$M_xM'_yH_z + zLi^+ + ze^- \leftrightarrows M_xM'_y + zLiH \qquad (2)$$

In 2012, Brutti et al. [17] calculated the theoretical capacity for a selection of metal hydrides assuming de-hydrogenated states identical to those obtained in H_2 thermal desorption reaction ($M_xM'_yH_z \leftrightarrows M_xM'_y + z/2H_2\uparrow$). Although these were only estimates, they demonstrated that the

potential of the hydride conversion reaction is enormous, their theoretical capacities overcome in the best cases thousands of $mAhg^{-1}$.

As a consequence, hydrides could represent a real breakthrough in Li-ion technology: they have the theoretical capability to overcome the performance limits of the current state-of-the-art negative electrodes (i.e. graphite, $Li_4Ti_5O_{12}$) and probably to improve safety. In fact lithium insertion into graphite mainly occurs at potential below 100 mV vs. Li^+/Li^0, where it could deposit on the anode surface, thus leading to a catastrophic dendrite growth and an internal short circuiting of the cell, on the contrary, hydride conversion processes occur above 100 mV vs. Li^+/Li^0 and therefore they are intrinsically safer compared to graphite [17].

2.1 State of the art

Starting from the studies of Oumellal et al. [16-18], MgH_2 still remain the most studied material of the hydrides family for electrochemical application. The reaction mechanism was confirmed to proceed through the formation of Mg and LiH, and lead to the reformation of MgH_2 during charge, according to reaction 1. Furthermore, at a low potential Mg formed upon discharge can react with lithium ions to form alloys. MgH_2 displays a full discharge capacity in the first cycle at an average voltage of 0.4 V versus Li^+/Li^0, with a reversible capacity of only 1480 $mAhg^{-1}$. Improvements in MgH_2 electrodes performance has been achieved either by the use of mechanochemical treatments [17] and nanoconfinements strategies [19].

After the promising results on MgH_2, other binary systems have been studied. Selection has been carried out on the basis of costs, environmental compatibility, safety and expected performance.

TiH_2 represents a good candidate for electrochemical application [18,20] thanks to its high theoretical capacity (1074 $mAhg^{-1}$) and low potential versus Li^+/Li^0. In addition, an improvement of the conversion process kinetics is expected because of good electrode conductivity due to the metallic properties of titanium hydride. Furthermore, Ti does not form alloy with lithium and consequently no parasitic reactions are present [21]. Capacity values close to the theoretical were achieved ball milling the hydride with carbon [20,22]. Interestingly, the reaction mechanism of TiH_2 with lithium consists of a complex reaction path and could not be described with the simple conversion of TiH_2 to form LiH and Ti. Instead, it consists of three different steps involving the initial formation of a solid solution δ-TiH_{2-x} (fcc) and LiH, followed by its transformation in a distorted orthorhombic phase δ-TiH (fco) and LiH. Finally, conversion reaction occurs with the reaction of δ-TiH_{2-x} (fcc) and δ-TiH (fco) with Li to form α-Ti (hcp) and LiH [20].

Beyond binary metallic hydrides MH_x, also more complex systems demonstrated to undergo a conversion reaction with lithium according to more complex reaction paths. First attempt to use ternary metallic hydrides was found in the original Oumellal paper [16]. They observed the conversion reaction for two ternary hydrides: $LaNi_{4.25}Mn_{0.75}H_5$ and $MgNiH_{3.7}$ for which electrochemical reactions leads to the conversion of 4.6 and 3.7 Li, respectively, in fairly good agreement with the hydrogen content of both hydrides. Afterwards, three Mg-based

complex hydrides (Mg_2FeH_6, Mg_2CoH_5 and Mg_2NiH_4) were investigated toward lithium conversion [20]. According to their initial hydrogen content, $MgM'H_x$ exhibits large theoretical capacities: 1455 $mAhg^{-1}$ for Fe; 1190 $mAhg^{-1}$ for Co and 963 $mAhg^{-1}$ for Ni, but of course lower than pure MgH_2, for their high formula weight. The three complex hydrides react with lithium approximately at the same potential (around 0.25 V vs. Li^+/Li^0). Their first discharge takes place readily, leading to the full conversion of hydrogen into lithium hydride [21], but unfortunately, practical reversibility has not yet proved.

Among complex hydrides, borohydrides [23] and alanates [24–27] deserve particular attention thanks to their lightweight and therefore higher theoretical gravimetric specific capacity, their environmental friendliness and low cost. They were subject of focus of our laboratory.

Borohydrides are polyanionic materials in which hydrogen is covalently bonded to central atoms in "complex" anions. Through a full reduction to metallic elements and LiH, specific capacity values on the order of 2000–4000 $mAhg^{-1}$ can be theoretically obtained thanks to the very low formula unit weight. Our study demonstrated the general thermodynamic feasibility of borohydrides conversion. Experimental capacities obtained are far from the theoretical ones, but it can be tuned by altering the sample morphology, because the optimal condition apparently consisting in small and poorly aggregate crystalline particles [23].

2.2 Aim and structure of the present work

As for borohydrides, the alanate family promises very interesting capacities due to the light molar weight of aluminum and the high hydrogen content of these complex hydrides. In fact, in view of a full conversion reaction in LiH and metal elements, they can theoretically achieve more than 1000 $mAhg^{-1}$ exchanging at least 3 electrons for redox center. Furthermore, their thermal stability makes these compounds feasible candidates for practical applications (details are in chapter 3).

The interest in them has been supported from pioneering DFT calculation performed in our laboratory few years ago [25,26], with the task to theoretically demonstrate the feasibility of alanates conversion reaction and its exploitability for application in lithium ion batteries. Besides our investigations, also Trepovich et al. [24] recently reported the use of $LiAlH_4$ and $NaAlH_4$ as anodes in lithium cells, furnishing a reference for comparison of our results and conclusions.

This PhD thesis provides the experimental evidences of the electrochemical activity of sodium and lithium alanates in lithium cells. The focus is on the properties and reaction mechanism of tetrahydro-alluminates ($LiAlH_4$ and $NaAlH_4$). Beside them, further three hexa-alanates phases (Li_3AlH_6, Na_3AlH_6 and $LiNa_2AlH_6$) have been investigated. In fact, the electrochemical reaction mechanism is expected to involve the formation of these compounds in the intermediate steps. Therefore, their behavior in electrochemical cells have been used to delineate a full picture of the conversion mechanism of the corresponding tetrahydro-alluminates compounds.

The work has been structured in three sections. The first section is focused on lithium alanates ($LiAlH_4$ and Li_3AlH_6). Chapter 4 reports the studies conducted on $LiAlH_4$. After confirming the electrochemical activity of this compound, mechanochemical treatments have been used to improve its performance. It's well known that mechanical grinding causes the reduction of the particles and induces strains that could lead to a better diffusion of hydrogen and lithium by increasing the number of diffusion paths. Comparisons with pristine sample have been made to evaluate the effects of the performed treatments on the structure, morphology and electrochemical performance. The electrochemical reaction mechanism has been elucidated by ex-situ diffraction experiments on $LiAlH_4$ based electrodes at different state of charge. The chapter ends with the study of the reactivity of $LiAlH_4$ with the carbonate based electrolyte

used for electrochemical tests. Chapter 5 provides the results for Li_3AlH_6. In this case, mechanochemistry has been used to synthesize the compound.

Second section describes the sodium alanates compounds ($NaAlH_4$, Na_3AlH_6 and $LiNa_2AlH_6$). As already did for lithium alanates, mechanochemical treatments have been used both to activate the bare $NaAlH_4$ (chapter 6) and to synthesize hexa-alanates phases (chapter 7). Then, for the obtained samples the physical-chemical and the electrochemical properties have been studied. Finally, in the chapter 8, the conversion reactions of the three phases have been described by in situ diffraction experiments during discharge/charge cycling. Further investigations have been addressed on $NaAlH_4$, in view of the encouraging results obtained.

In conclusion, the last section is dedicated to the performance improvements of the alanates based electrodes. In fact, for all the samples poor cell efficiency and cyclability have been observed. This could be mainly ascribed to the big volumetric expansion observed with conversion reaction as well to the high reactivity of this materials with the common solvents used as electrolytes, due to the high reducing power of alanates. Two main strategies have been adopted to reduce these effects: the nanoconfinement in a nanoporous carbon matrix, as described in chapter 9 and the replacement of carbonates based electrolyte with an ionic liquid, as in chapter 10.

3

Light-weight complex hydrides: Alanates

3.1 General aspects

Alanates (also called aluminohydrides) refer to the complex hydrides consisting of aluminum and hydrogen. Alkali metal aluminohydrides are ionic-covalent compounds, in which Al-H are covalent bonds and form polyanions collecting the negative charge. The negative charge of the anions is compensated by cations, e.g. Li^+ or Na^+ [28], and (M^+ - $[AlH_4]^-$) and ($3M^+$ - $[AlH_6]^{3-}$) are ionic bonds.

Mainly known as reducing agents in organic chemistry, during the last decade complex aluminum hydrides have received increasing attention as potential candidates for hydrogen storage. In fact, they possess high gravimetric hydrogen densities thanks to the large number of hydrogen atoms per metal atom. The advantageous properties of complex aluminum hydrides are the low price of the compounds, their low weight and their no toxicity [29]. Furthermore, they are known to be stable and decompose only at elevated temperatures, often above the melting point of the complex.

3.1-1 Lithium alanates: structure and decomposition

$LiAlH_4$ was first synthesized by a treatment of lithium hydride with an ether solution of aluminum chloride in 1947 [30] and the Li_3AlH_6 compound was first reported in 1966 [31].

The crystal structure of $LiAlH_4$ was first proposed by Sklar and Post [32] by using single crystal XRD and it was found a monoclinic structure with space group $P2_1/C$. Each aluminum atom is surrounded by 4 hydrogen atoms to form isolated $[AlH_4]^-$ tetrahedra with Al-H bond lengths of 1.55 Å. The lithium ion is surrounded by 5 hydrogen atoms, four at distances between 1.88 and 2.00 Å and a fifth one at 2.16 Å (figure 3.1). They suggested to perform neutron diffraction to confirm the slight distortion of the tetrahedra from the ideal configuration as seen from the individual H-Al-H angles. An accurate structure determination was again made by Hauback et al. [33] on the deuterated homologue, using XRD and neutron

diffraction at 8 K and 295 K. According to these authors, the Li atoms coordinate one deuterium atom from every of the 5 surrounding well separated AlD_4 tetrahedra and adopt trigonal bipyramidal coordination. The distortion in the tetrahedral configuration was found to be as suggested by Sklar and Post [32] and it increases on cooling. The Al-D distances are in the range 1.603-1.633 Å at 295K and 1.596-1.645 Å at 8K [34].

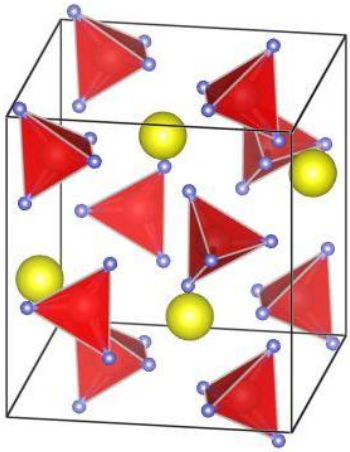

Figure 3.1 - Crystal structure of $LiAlH_4$. The $[AlH_4]^-$ anions are depicted as red tetrahedra and the Li cations as yellow spheres.

The structure of Li_3AlD_6 was determined by Brinks et al. through X-ray and neutron diffraction [35]. The structure is described as a distorted bcc of $[AlD_6]^{3-}$ units. The space group was found to be *R*3h, and the structure (Figure 3.2) consisted of isolated $[AlD_6]^{3-}$ octahedra connected by six-coordinated Li atoms (each Li atom is coordinated to two corners and two edges of the octahedra, six hydrogen atoms total). The Al-D distances were 1.734 and 1.754 Å, which are comparable to the 1.758 Å (average) found for the sodium analogue. The D-Al-D bond angles were in the range from 86.98° to 93.02°. The Li-D distances ranged from 1.892 to 2.120 Å, and the shortest Al-Al distance was 4.757 Å [28].

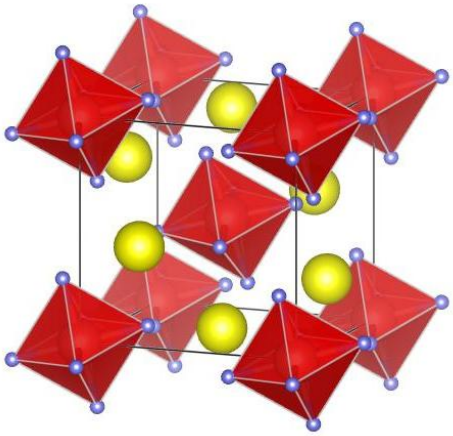

Figure 3.2 - Crystal structure of Li_3AlH_6, showing $[AlH_6]^-$ octahedra (red) and 6 six-coordinated Li (yellow).

Lithium alanates have high hydrogen content. For instance, the total hydrogen content is 10.5 and 11.2 wt.% for $LiAlH_4$ and Li_3AlH_6, respectively. The decomposition of $LiAlH_4$ takes place in three stages with 5.3, 2.6 and 2.6 wt.% release of hydrogen, respectively:

$3LiAlH_4 \rightarrow Li_3AlH_6 + 2Al + 3H_2\uparrow$

$Li_3AlH_6 \rightarrow 3LiH + Al + 3/2\ H_2\uparrow$

$3LiH + 3Al \rightarrow 3LiAl + 3/2\ H_2\uparrow$

The first dehydrogenation process occurs exothermically with ΔH= -10 kJ mol^{-1} H_2 at 160-180 °C releasing 5.3 wt.% of H_2. The second reaction occurs endothermically with ΔH= 25 kJ mol^{-1} H_2 at 180-220 °C with 2.6 wt.% of H_2 evolution. Finally the third reaction is completed at much higher temperature around at 400 °C with an enthalpy of 140 kJ mol^{-1} H_2 [34].

3.1-2 Sodium alanates: structure and decomposition

Sodium tetrahydroaluminate ($NaAlH_4$) was first synthesized in the late 1940s by Finholt et al. [36] and trisodium hexahydroaluminate (Na_3AlH_6) about 15 years later by Zakharin and Gavrilenko [37]. The crystal structure of $NaAlH_4$ was first discussed by Lauher et al. [38] using single crystal X-ray diffraction in 1979. The structure was suggested to be tetragonal with space group $I4_1/a$ consisting of isolated $[AlH_4]^-$ tetrahedra. Sodium atoms are surrounded by eight nearest $[AlH_4]^-$ tetrahedra (figure 3.3) with an Al-H bond length of

1.532(7) Å [34]. Based on IR spectroscopy data, Bel'skii et al. [39] pointed out in 1983 that the Al-H distances should be longer in $NaAlH_4$. Therefore, they re-determined the structure from single-crystal X-ray diffraction data. The refinements were again carried out within the space group $I4_1/a$ and the data converged to give an Al-H distance of 1.61(4) Å that is in agreement with the IR data. To calculate the coordinates of hydrogen atoms more accurately, a neutron diffraction study was performed on the deuterated compound i.e. $NaAlD_4$ at 8 and 295 K [40]. It was found that no significant change in the Al-D bond length occurred with the change in temperature and it was found to be 1.627(2) Å and 1.626(2) Å at 8 and 295 K, respectively. The two Na-D bond lengths were found to be equal, i.e. 2.403(2) Å and 2.405(2) Å at 8 K and 2.431(2) Å and 2.439(2) Å at 295 K. The shortest distance (Al-Al) was found to be 3.737(1) Å and 3.779(1) Å at 8 and 295 K, respectively. The angles of the $[AlD_4]^-$ tetrahedron were distorted and equal to 107.32° and 113.86° [34].

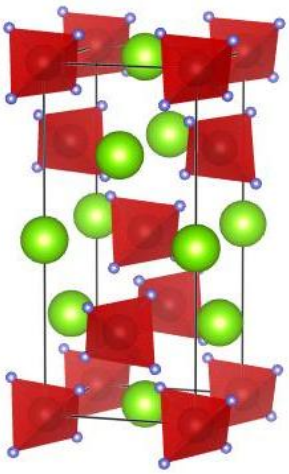

Figure 3.3 - Crystal structure of $NaAlH_4$. The $[AlH_4]^-$ anions are depicted as red tetrahedra and the Na cations as green spheres.

The crystal lattice of metal hexahydroaluminates is built of isolated octahedral anions $[AlH_6]^{3-}$ and metal cations M^+. Two structural modifications are known for sodium hexahydroaluminate Na_3AlH_6: the monoclinic α phase with space group $P2_1/n$ (a = 5.410 Å, b = 5.539 Å, c = 7.766 Å, β = 90.18°) [41] and the cubic (fcc) β phase (a = 7.755 Å). The transition from the stable α phase to the metastable β phase occurs at 525 K. Aluminum is surrounded by an octahedron of hydrogen atoms (figure 3.4). Sodium occupies two crystallographically nonequivalent positions Na(I) and Na(II). The Na(I) coordination

polyhedron is a hydrogen octahedron, while the hydrogen environment of Na(II) is a distorted Archimedean antiprism. The complete crystal structure of α-Na_3AlD_6, with the location of the deuterium atoms, was determined at 295 K on the basis of synchrotron X-ray and neutron diffraction data [28]. Crystal symmetry was confirmed monoclinic, space group $P2_1/n$ with a = 5.390 Å, b = 5.514 Å, c = 7.725 Å, β = 89.86°, and z = 2. The octahedral anion is slightly distorted. The Al-D distances are 1.746-1.770 Å. Despite the different coordination, the Na(I)-D and Na(II)-D distances are nearly the same, 2.267-2.307 Å [28].

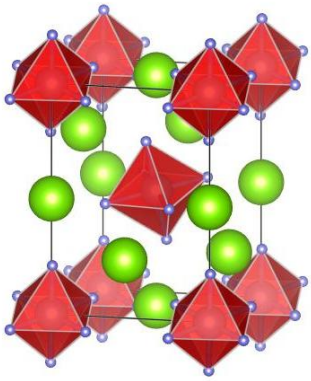

Figure 3.4 - Crystal structure of monoclinic α-Na_3AlH_6. The complex $[AlH_6]^{3-}$ anions are depicted as red octahedra and the Na cations as green spheres.

$NaAlH_4$ and Na_3AlH_6 contain large amounts of hydrogen (7.4 and 5.9 wt.% respectively). The release of hydrogen does not occur in a single-step reaction but the decomposition of $NaAlH_4$ proceeds as follows:

$3NaAlH_4 \rightarrow Na_3AlH_6 + 2Al + 3H_2\uparrow$

$Na_3AlH_6 \rightarrow 3NaH + Al + 3/2\ H_2\uparrow$

$NaH \rightarrow Na + 1/2\ H_2\uparrow$

$NaAlH_4$ first decomposes evolving molecular hydrogen and forming metallic Al and an intermediate compound, Na_3AlH_6. This intermediate phase then decomposes to NaH with additional metallic Al formation and hydrogen evolution. Stoichiometrically, the first step consists of 3.7 wt.% H_2 release and the second step 1.9 wt.%, for a theoretical net reaction of 5.6 wt.% reversible gravimetric hydrogen storage. The equilibrium pressure calculated from the enthalpy values, 37 kJ mol^{-1} H_2 and 47 kJ mol^{-1} H_2 for the first and second step

respectively, were found to be 1 bar for the first step at 30 °C and 1 bar for the second step at 100 °C [42]. However the processes are characterized by slow kinetics and reversibility only under severe conditions. The operating temperatures are between 185 and 230 °C, and 260 °C for the first and the second reaction, respectively [37]. Finally, the decomposition of NaH occurs at a much higher temperature (> 400 °C), with the total hydrogen release of 7.4 wt.% [43]. It should be note that decomposition is characterized also by the melting of the $NaAlH_4$ (at about 185 °C) and the conversion of monoclinic α-Na_3AlH_6 into cubic β-Na_3AlH_6 (≈ 282 °C). Re-hydrogenation of these complexes is very difficult to achieve. Dymova et al. [44] reported the complete conversion to $NaAlH_4$ under 17.5 MPa hydrogen pressure at 270 °C for 3 hours. These conditions were improved by Bogdanovic and Schwickardi [45]. Their pioneering studies demonstrated that, upon doping with selected titanium compounds, the dehydriding of anionic aluminum hydrides could be kinetically enhanced and rendered reversible under moderate conditions in the solid state. Since the discovery by Bogdanovic and Schwickardi of the reversible hydrogen storage of $NaAlH_4$ with Ti-containing catalysts (dopants), this compound and similar $Mn^+[AlH_4]_n^-$ have been in focus.

3.1-3 The mixed alanate $LiNa_2AlH_6$: structure and decomposition

Complex hydrides based on $[AlH_6]^{3-}$ also have a considerable hydrogen content. In addition to Li_3AlH_6 (5.6 wt.% for desorption to LiH and Al) and Na_3AlH_6 (3.0 wt.%), the mixed hexahydrides $LiNa_2AlH_6$ has to be considered thanks to its high hydrogen content (3.5 wt.%). $LiNa_2AlH_6$ was synthesized in 1982 by Claudy et al. [46] and it was found [45] to be more stable than either the Li_3- and Na_3- hexahydride phases [47].

The structure of Na_2LiAlD_6 (Figure 3.5) was determined by Brinks et al [47]. The structure was well defined in a cubic unit cell with a space group of *Fm*3*m*. The compound had a perovskite-type structure best described as a distorted fcc of $[AlD_6]^{3-}$ units with Li in the octahedral sites and Na in the tetrahedral sites. The Al-D bond distances were found to be 1.760-(0.03) Å. The Al-D bond distances of the $[AlD_6]^{3-}$ octahedra were significantly shorter in size than the octahedra of Li_3AlD_6 (average of 1.774 Å) [35] and longer than the octahedra of Na_3AlD_6 (1.756 Å) [41]. The AlD_6 octahedra of Na_2LiAlD_6 are ideal, having equal Al-D distances and ideal angles. The shortest Al-Al distance was 5.222 Å [48].

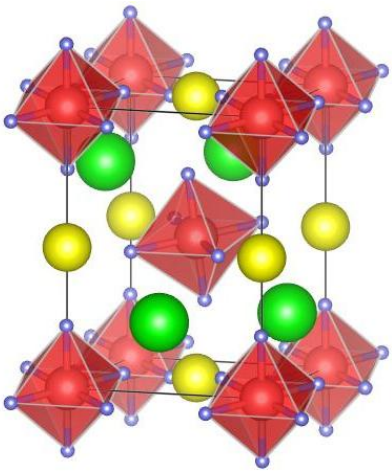

Figure 3.5 - Crystal structure of monoclinic $LiNa_2AlH_6$. The complex $[AlH_6]^{3-}$ anions are depicted as red octahedra and the Li and Na cations as yellow and green spheres, respectively.

Only few results of thermodynamics of $LiNa_2AlH_6$ are reported in the literature [49-50]. The mixed aluminum hydride decomposes in one endothermic step between 220 and 230 °C:

$$LiNa_2AlH_6 \rightarrow 2NaH + LiH + Al + 3/2\ H_2\uparrow$$

The decomposition enthalpy was measured using a Van't Hoff plot and found to be 53.5±1.2 kJ mol^{-1} H_2 [50].

3.2 Alanates as anodes for lithium ion batteries

The advantageous properties that made alanates suitable for H_2 storage, make them very interesting for electrical storage. In view of their light-weight, high hydrogen content and considering a full conversion reaction to LiH and metal elements, alanates can theoretically exchange at least 3 electrons per redox center, providing high capacities and energy values. Furthermore, low cost and abundance of the basic elements and thermal stability make them suitable for practical use in a lithium-ion device.

Theoretical capacity can be derived from Faraday's law, using the following equation:

$$C = \frac{F \cdot ne}{MW \cdot 3.6}\left[\frac{mAh}{g}\right]$$

Where:

F = Faraday's constant, with value 96487 C/mole. Equal to Avogadro's number *charge of electron

ne = number of electrons involved in the reaction

MW = molecular weight of hydride

3.6 = conversion factor from C (A*s) to mAh (1 Ah = 1 Amp*hour = 1 C/s *3600s = 3600C)

Table 3.1. reports possible complete conversion reactions and resumes the theoretical capacity values calculated for alanates under investigation. Values ranging from 2119 $mAhg^{-1}$ for $LiAlH_4$ down to 1493 $mAhg^{-1}$ for Li_3AlH_6 can be achieved by conversion with lithium. These values exceed more than 3 times that of the current anode materials (i.e. graphite 372 $mAhg^{-1}$). However, it should be noted that although $LiAlH_4$ easily decomposes exothermically to Li_3AlH_6, it preserves some relevance thanks to the high residual theoretical capacity.

Table 3.1 - Theoretical capacity of the alanates under investigation.

Conversion reaction	MW	ne	Theoretical Capacity ($mAhg^{-1}$)
$LiAlH_4 + 3Li^+ + 3e^- \rightleftarrows Al + 4LiH$	37.95	3	2119
$Li_3AlH_6 + 3Li^+ + 3e^- \rightleftarrows Al + 6LiH$	53.85	3	1493
$NaAlH_4 + 4Li^+ + 4e^- \rightleftarrows Na + Al + 4LiH$	54	4	1985
$Na_3AlH_6 + 6Li^+ + 6e^- \rightleftarrows 3Na + Al + 6LiH$	102	6	1576
$LiNa_2AlH_6 + 5Li^+ + 5e^- \rightleftarrows 2Na + Al + 6LiH$	85.95	5	1871

DFT calculation demonstrated the theoretical feasibility of the conversion reaction in alanates compounds [25,26]. Specifically, the predictions of the electrochemical potentials versus Li of the possible conversion reactions involving the alanates phases have been reported. Different reaction paths have been considered for all the alanates under investigation. In fact, in analogy with the thermal desorption process, alanates conversion reaction is expected to involve the formation of intermediate compounds before the complete reduction.

The results obtained for lithium alanates phases are listed in table 3.2. Different reaction paths have been computed and the corresponding Nernst potentials for the processes calculated [25].

Speaking of $LiAlH_4$, four reaction paths have been taken into account: (R1) the overall conversion of $LiAlH_4$ to give LiH + Al, (R2) the formation of the intermediate Li_3AlH_6 , (R3) the formation of metastable AlLi phase, instead of simple metallic aluminum and (R4) the simultaneous conversion in Li_3AlH_6 and AlLi. Reaction (R1), i.e. the one-step process, is predicted to occur at 0.82 V vs. Li, largely above the plating potential of lithium, thus suggesting a thermodynamic driving force to incorporate lithium in a $LiAlH_4$ electrode through a conversion reaction mechanism. But, as expected, (R2) is thermodynamically favoured (0.84 V vs. Li).

Furthermore, the conversion of Li_3AlH_6 in LiH and Al (R5) is thermodynamically favoured respect to the formation of alloy and it is predicted to occur at 0.74 V. In this view, from the thermodynamic point of view, a two steps mechanism (R2)-(R5) should occur preferentially in lithium cells [25].

Besides conversion reactions, also the alloying of lithium in the aluminum metallic lattice has been modelled by computing the formation of the AlLi phase upon reduction (reaction R7).

The predicted e.m.f. of (R7) is 0.29 V vs. Li. Apparently the alloying reaction occurs in a potential range well separated from the conversion reaction ones [25].

In conclusions, from the thermodynamic point of view, $LiAlH_4$ reacts with lithium through the formation of Li_3AlH_6 followed by its decomposition in LiH and Al. Finally, metallic aluminum can further react through alloying. Therefore reaction sequence should be: (R2)-(R5)-(R7).

Table 3.2 - DFT predicted redox potentials of the possible conversion reactions for lithium alanates phases.

Conversion Reaction	**Electrochemical potentials (V vs. Li)**
(R1) $3\ LiAlH_4 + 3Li \rightleftarrows 4LiH + Al$	0.82
(R2) $3\ LiAlH_4 + 6Li \rightleftarrows Li_3AlH_6 + 2Al + 6LiH$	0.86
(R3) $LiAlH_4 + 4Li \rightleftarrows AlLi + 4\ LiH$	0.69
(R4) $3\ LiAlH_4 + 8Li \rightleftarrows Li_3AlH_6 + 2AlLi + 6LiH$	0.71
(R5) $Li_3AlH_6 + 3Li \rightleftarrows 6LiH + Al$	0.74
(R6) $Li_3AlH_6 + 4Li \rightleftarrows AlLi + 4LiH$	0.63
(R7) $Al + Li \rightleftarrows AlLi$	0.29

Table 3.3 reports the calculation for the sodium alanates compounds [26]. Concerning the $NaAlH_4$ phase, four different reduction paths have been considered (e.g. Reactions R8-R11). The calculated voltages of the partial reduction of $NaAlH_4$ to form Na_3AlH_6 or $LiNa_2AlH_6$ phases are very similar, 0.70 V and 0.73 V, respectively, nevertheless the formation of $LiNa_2AlH_6$ is slightly more favoured. The direct conversions of $NaAlH_4$ to give NaH (R10) or Na (R11) without formation of other intermediates are predicted to occur, as expected, at an electrochemical potential lower than the two reactions (R8) and (R9). This picture suggests a thermodynamically-driven multistep conversion for the $NaAlH_4$ phase. In particular reactions (R9) is likely the first step of the overall process.

Turning to Na_3AlH_6, the reaction thermodynamics of the sodium hexahydride suggests a favoured path through a direct conversion reaction (R13-R14) rather than the formation of the intermediate $LiNa_2AlH_6$ (R12). Between the two overall conversions, as expected the partial

reaction to give NaH is thermodynamically more favoured in comparison to the deeper conversion to Na metal. On the other hand, the mixed Li-Na hexahydride is predicted to undergo to a partial conversion reaction (R15) to Na_3AlH_6 as intermediate product phase. Finally, the reduction of NaH (R18) has been predicted to occur at 0.43 V [26].

Table 3.3 - DFT Calculated voltages vs. Li of the electrochemical conversion processes involving the $NaAlH_4$, Na_3AlH_6 and $LiNa_2AlH_6$ phases.

Conversion Reaction	**Electrochemical potentials (V vs. Li)**
(R8) 3 $NaAlH_4$ + 6 Li ⇄ Na_3AlH_6 + 6 LiH + 2 Al	0.70
(R9) 2 $NaAlH_4$ + 3 Li ⇄ $LiNa_2AlH_6$ + 2 LiH + Al	0.73
(R10) $NaAlH_4$ + 3 Li ⇄ NaH + Al + 3 LiH	0,68
(R11) $NaAlH_4$ + 4 Li ⇄ Na + Al + 4 LiH	0.62
(R12) Na_3AlH_6 + Li ⇄ $LiNa_2AlH_6$ + Na	0.41
(R13) Na_3AlH_6 + 3 Li ⇄ 3 NaH + Al + 3 LiH	0.61
(R14) Na_3AlH_6 + 6 Li ⇄ 3 Na + Al + 6 LiH	0.53
(R15) 3/2 $LiNa_2AlH_6$ + 3/2 Li ⇄ 3 LiH + 1/2 Al + Na_3AlH_6	0.66
(R16) $LiNa_2AlH_6$ + 3 Li ⇄ 2 NaH + Al + 4 LiH	0.64
(R17) $LiNa_2AlH_6$ + 5 Li ⇄ 2 Na + Al + 6 LiH	0.56
(R18) NaH + Li ⇄ Na + LiH	0.43

In summary, DFT calculations suggest that sodium alanates can react in a lithium cell through a conversion reaction mechanism. As expected, the electrochemically driven lithium incorporation involve the formation of intermediates before the full reduction in Na, Al and LiH. Considering $NaAlH_4$, the theoretical conversion reaction consists of a complex four-step mechanism according to the sequence (R9)-(R15)-(R13)-(R18). This reaction sequence occurs starting from $NaAlH_4$ by forming subsequently $LiNa_2AlH_6$, Na_3AlH_6 and NaH as reaction intermediates before leading to a complete conversion to a mixture of metallic aluminium and sodium with lithium hydride. Partial identical (R15)-(R13)-(R18) and (R13)-(R18) reaction sequences are predicted to occur starting from $LiNa_2AlH_6$ and Na_3AlH_6 hexahydrides [26]. Another important consideration that needs to be evaluated regards the possible occurrence of the Na stripping reaction upon charge. DFT calculations predicted that the reduction reaction $Na(s) \rightarrow Na^+(solv) + e^-$ occurs at 0.41 V. Therefore, once reduced to metallic Na(s), upon

charge, the electrode is expected to strip sodium instead of convert back through the reverse (R18) reaction. This complex asymmetric reactivity may also be complicated by the unavoidably different charge transfer kinetics of the (R18) conversion reaction compared sodium stripping. The final net effect of this charge reaction mechanism may be the Na-depletion of the electrode and therefore the irreversible loss of capacity [26].

It is worth noting both in the case of lithium and in that of sodium alanates, all considered reactions from (R1) to (R18) occur within few hundreds if not tens Ohms. As a consequence, it may be predicted that, as effect of overvoltages, several reactions could occur on the same time and the alanates conversion mechanism could follow different paths respect what expected by thermodynamic.

LITHIUM ALANATES

4

$LiAlH_4$

4.1 Samples preparation

Bulk $LiAlH_4$ powder (hydrogen storage grade) purchased from Sigma Aldrich has been used to prepare all samples. Lithium alanate powder has been used both as received and after mechanochemical activation treatments of 1 and 15 hours.

Mechanochemical methods are a useful tool to reduce the particle size, break oxidized shallow layers, increase the atomic disorder and induce high level of elastic shears and other defects, in order to facilitate the diffusion of hydrogen and lithium.

This activation step has been performed grinding pristine $LiAlH_4$ by High Energy Ball Milling (HEBM), using an 8000M Spex Shaker (1080 cycles per minute). Under the inert Ar atmosphere of the glove box, the powder has been placed into a stainless steel jar box and 10 mm diameter stainless steel balls have been added in order to obtain powder to balls weight ratio of 1:20. Milling sessions have been carried out at room temperature, intermittently for 15 minutes followed by 30 minutes of rest to avoid samples overheating.

The bare alanate samples have been further mixed with Super P, a conductive carbon used as additive in electrode realization, in order to obtain $NaAlH_4$:C weight ratio of 0.625:0.375.

The conductive carbon Super P has been added either by mixing with mortar and pestle or by further HEBM. The addition of carbon by ball milling is supposed to have a double effect on the properties of metal hydrides. It acts as conductive additive, which increases the electronic conductivity of the electrode, and as coating agent, which prevents the agglomeration of the hydride particles during electrochemical processes.

In table 4.1 there is the list of prepared samples and labeling adopted to identify them.

Table 4.1 - Scheme of lithium alanates samples under investigation

Name	Label	Time of HEBM (h)	Addition of SuperP	Time of HEBM with SuperP (h)
$LiAlH_4$	LB0	0	no	/
	LB0D0	0	yes	0
	LB1	1	no	/
	LB1D0	1	yes	0
	LB1D05	1	yes	0.5
	LB15	15	no	/
	LB15D5	15	yes	5

Samples are labeled as BxDy, for which x indicates the duration in hours of the mechanochemical activation and y indicates the subsequent milling time, in hours, with Super P.

4.2 Physical-chemical characterization

The structural properties of lithium alanate samples has been investigated by X-ray diffraction (XRD) and Fourier Transformed Infrared Spectroscopy (FTIR).

XRD pattern of pristine sample is given in figure 4.1. The halo observed in the pattern shown in figure is due to the glass capillary used as a holder in the diffraction experiment. Phase purity and lattice parameters have been determined by the use of Maud program [51]. ICSD-22247 pattern was used as reference. As purchased sample consists of pure $LiAlH_4$ characterized by monoclinic $P2_1/c$ space group. Calculated lattice parameters are a = 4.835 ± 0.001 Å, b = 7.824 ± 0.003 Å, c = 7.931 ± 0.003 Å and β = 112.3 ± 0.1. The average crystallites size is about 76 nm.

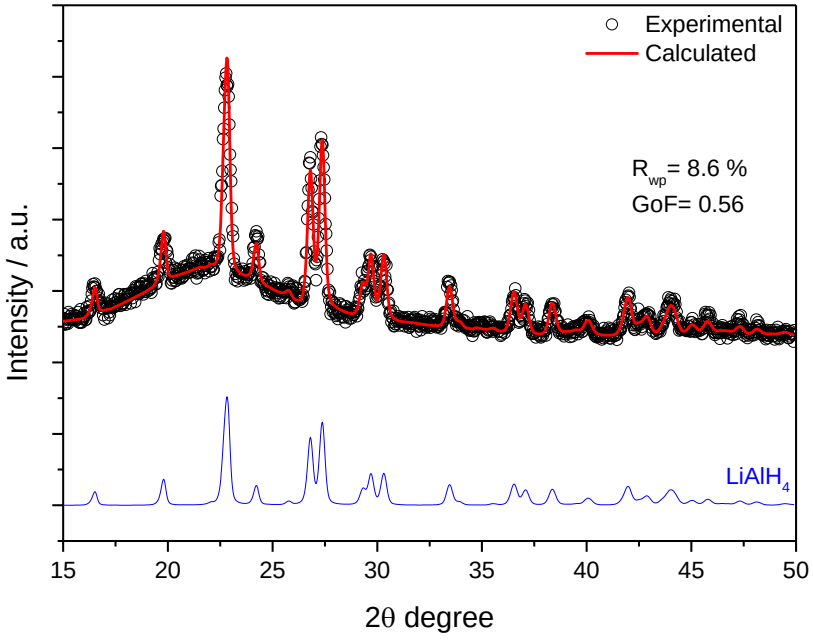

Figure 4.1 - Pattern refinement of the as purchased $LiAlH_4$ sample (LB0). Black circle represent the experimental pattern, red line the calculated pattern.

Figure 4.2 highlights the effect of ball milling on crystal structure. The XRD data are compared with the expected reference patterns of $LiAlH_4$ and Li_3AlH_6 calculated by Powdercell [52] from the reported experimental structures of the deuterated alanates [53]. Pristine sample was reported for comparison (LB0 sample in figure).

After 1 hour of ball milling, sample LB1 doesn't show any difference respect the pristine alanate. On the contrary, prolonged time of ball milling (LB15) causes partial decomposition of the sample. Peaks relating to the $LiAlH_4$ phase slightly decrease in intensity and two peaks at 38.5° and 44.7° 2θ attributable to (111) and (200) reflections of cubic aluminum (S.G.: Fm-3m) appear. However, no Li_3AlH_6 diffraction lines can be clearly observed.

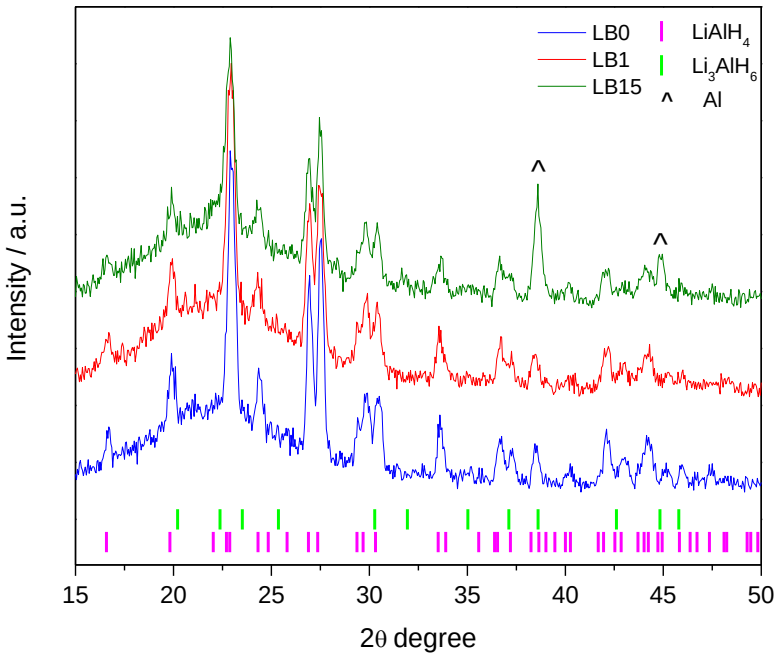

Figure 4.2 - X-ray powder diffraction of LB0, LB1 and LB15 samples, respectively after 0, 1 and 15 hours of mechanochemical activation treatment. $LiAlH_4$ and Li_3AlH_6 Bragg reflections positions are reported as reference.

Figures 4.3 and 4.4 illustrate Infrared spectra of samples after 1 and 15 hours of ball milling. FTIR spectra have been acquired in transmission mode, by a JascoFTIR-300 apparatus. All spectra have been recorded at room temperature, in the wave number range between 2000 and 400 cm^{-1}. Samples, as fine powders, have been mixed with CsI in a ratio of 1:100 mg (powder to CsI respectively) and then pressed in pellets by a Pike die set and hand-press. FTIR assignments were done by comparing with data reported by Ares Fernandez et al. [54] and Bureau et al. [55].

Pristine sample (LB0 in figure 4.3) exhibits the characteristic vibrational frequencies of $LiAlH_4$: Al-H stretching modes at 1780 and 1645 cm^{-1} and at lower frequencies the Li-Al-H bending modes of $LiAlH_4$ at 895 and 700 cm^{-1} respectively. Furthermore, weak vibrational

signals of Li_3AlH_6 are also visible: Al-H stretching modes of $[AlH_6]^{3-}$ octahedron at 1415 and 1260 cm^{-1} and the Li-Al-H bending mode at 1013, 960 and 812 cm^{-1}. After 1 hour of ball milling (LB1 sample) the spectrum doesn't show any different vibrational features. Additional 30 minutes of ball milling with carbon (LB1D05) enhance vibrational signals of Li_3AlH_6, while the $LiAlH_4$ bending modes at 895 and 700 cm^{-1} slightly shift at 870 and 715 cm^{-1}. Finally, the peak at 539 cm^{-1} in the LB1D05 sample is associated to Al-O stretching mode of AlO_4, which forms when the decomposition product Al reacts with O_2 during brief exposure to the air upon sample transfer.

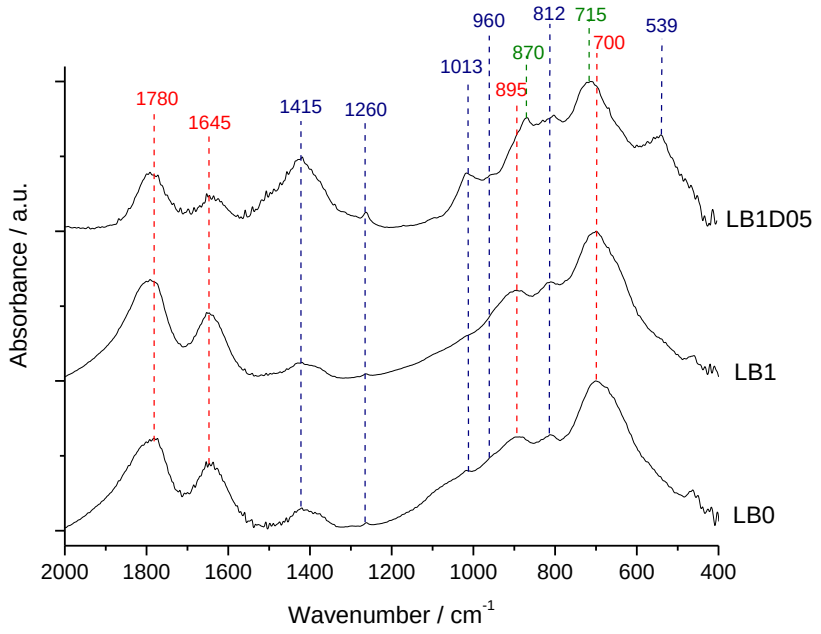

Figure 4.3 - FTIR spectra of $LiAlH_4$ samples: LB0, after 1 hours of activation (LB1) and additional 30 minutes of ball milling with SuperP (LB1D05).

The effect of prolonged time of ball milling is shown in figure 4.4. After 15 hours of ball milling (LB15), Al-H stretching modes of $LiAlH_4$ decrease in intensity. Conversely, the peaks at 1415 and 1260 cm^{-1} become predominant, indicating a huge presence of Li_3AlH_6. In the bending region of Li-Al-H group, the peak at 700 cm^{-1} decreases in intensity and appear a peak at 866 cm^{-1}. Also in this sample the peak of aluminum oxide can be recognized. Sample with additional ball milling step with carbon (LB15D5) doesn't exhibit vibrational feature of $LiAlH_4$.

Morphological analysis has been performed by transmission electronic microscopy. Figures 4.5b-c show the TEM images of the sample subjected to 1 hours of ball milling in comparison to pristine material (figure 4.5a).

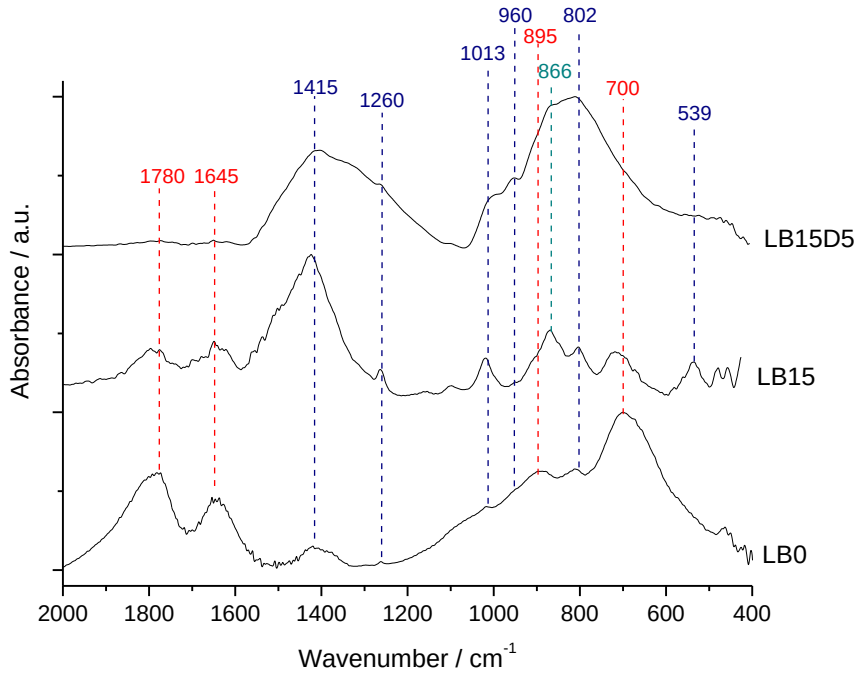

Figure 4.4 - FTIR spectra of $LiAlH_4$ samples: LB0, after 15 hours of activation (LB15) and additional 5 hours of ball milling with Super P (LB15D5).

Pristine $LiAlH_4$ (LB0) exhibits irregular particles of variable dimension. The smallest particles have a 50 nm size and contain inside brighter regions that could be related to voids left from H_2 desorption, undesired side-effect of the TEM analysis. In fact local overheating occurs in consequence of the interaction between the electronic beam and the alanate particles, favoring hydrogen release. 1 hour of ball milling leads to drastic nanometrization and homogenization of the particles size thus forming aggregated round-shaped nanoparticles (some of them apparently hollow) with diameters in the range 50-100 nm that are quickly damaged by the electron beam during the TEM analysis. Sample LB1D05, milled with Super P, shows a rather different morphology. Very dark and compact regions can be observed, probably constituted by aggregates of $LiAlH_4/Li_3AlH_6$ and carbon, covered by a 10-20 nm thick layer on the surface. This material is apparently less reactive under the electron-beam and noticeable alteration of the morphologies has not been observed during the TEM experiments. Finally, figure 4.6 shows the features of $LiAlH_4$ after 15 hours of ball milling. In the LB15 sample irregular particles lower than 100 nm can be observed. After additional 5 hours of ball milling with carbon (LB15D5 sample), morphology is again characterized by compact aggregates where the pristine hydride is hardly recognizable.

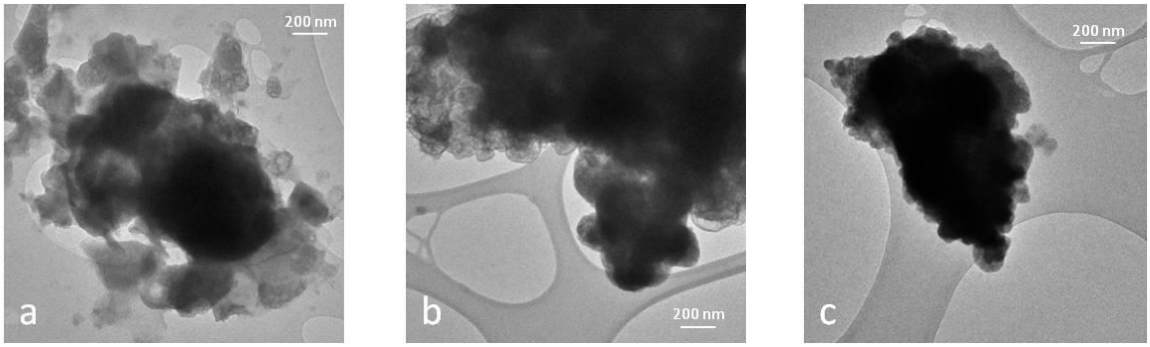

Figure 4.5 - TEM images of $LiAlH_4$ as a function of the mechanochemical treatments: a) LB0, b) LB1 and c) LB1D05.

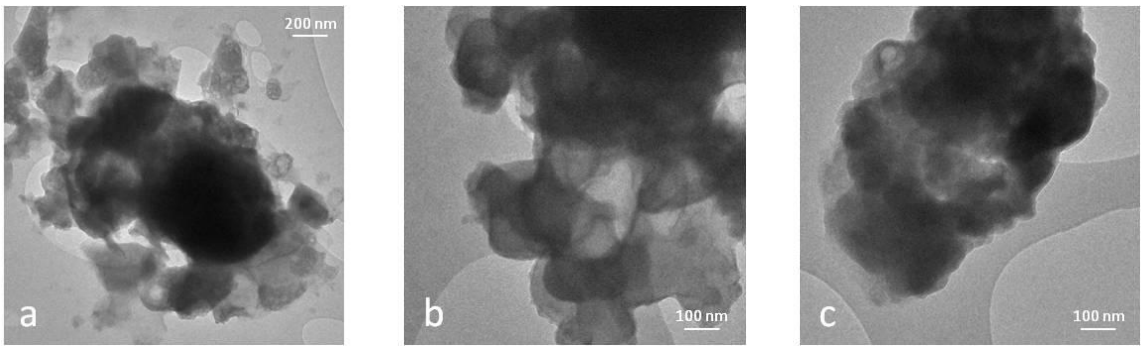

Figure 4.6 - TEM images of $LiAlH_4$ as a function of the mechanochemical treatments: a) LB0, b) LB15 and c) LB15D5.

In conclusion, preliminary sample characterization highlighted the effects of mechanochemical activation step on $LiAlH_4$. The combined analysis of XRD and FTIR analysis suggest that, after 1 hour of milling, $LiAlH_4$ is preserved as the major component of the material but the surfaces of the pristine particles are likely covered by a thick film of a low crystalline Li_3AlH_6 phase. Probably, it could be ascribed to local overheating during milling session that promotes the exothermic decomposition of $LiAlH_4$ to Li_3AlH_6. Upon 15 hours of milling, hydrogen desorption becomes important.

Furthermore, as a consequence of the additional step of ball milling with carbon, decomposition is massive. 30 minutes of milling (LB1D05) with carbon transform the LB1 sample from almost pure alanate to a mixture of the two lithium aluminum hydride phases. While, 5 hours of milling with carbon (LB15D5) leads to a complete decomposition of $LiAlH_4$ to Li_3AlH_6. Apparently carbon acts as a catalyst for hydrogen desorption, accelerating the kinetics and lowering the desorption temperature. For this purpose, LB15D5 sample has been discarded.

4.3 Electrochemical characterization

For electrochemical tests, electrodes were prepared by adding PVdF Kynar 2801 to the mixture of alanate and Super P, in order to get an "active material / SuperP / polymer" weight ratio of 5/3/2. The final mixture was pressed on 10mm diameter Cu disks with a mild pressure, in order to obtain electrodes with around 1-2 mg/cm^2 active material.
For Potentiodynamic Cycling with Galvanostatic Acceleration (PCGA) tests, electrochemical cells were assembled by facing the working electrode to a lithium metal foil counter through a Whatmann borosilicate fiber separator swollen with a 1M solution of $LiPF_6$ in ethylene carbonate – dimethyl carbonate (EC:DMC) 1:1 mixture (LP30, Merck Selectipur). Lithium reference electrode is placed perpendicularly to the assembly, soaked by an electrolyte excess. PCGA tests have been carried out by means of a Biologic VSP potentiostat, in the potential range of 2.5-0.01 V, with 10 mV steps and a cutoff current equal to C/20, calculated as the current to deliver in 20 hours the full theoretical conversion capacity.

PCGA tests have been carried out to highlight the electrochemical reactivity of lithium alanates in lithium device. Figure 4.7 reports the potential profile vs. capacity for pristine samples (LB0D0). The discharge of sample LB0D0 is characterized by an extended plateau occurring at 0.78 V vs. Li followed by a slope and by two other evident plateaus at 0.27 V and 0.15 V vs. Li. The total capacity exchanged upon discharge is 1180 mAhg^{-1}, which correspond to only 1.67 lithium equivalents incorporated compared to the 3 lithium equivalents theoretically available. Also the reversibility of the process appears to be very poor, since the capacity recovered on charge is only 184 mAhg^{-1}. Nevertheless it is worth noting that charge voltage profile shows two plateaus at 0.44 and 0.80 V vs. Li, in good conformity with the discharge process.

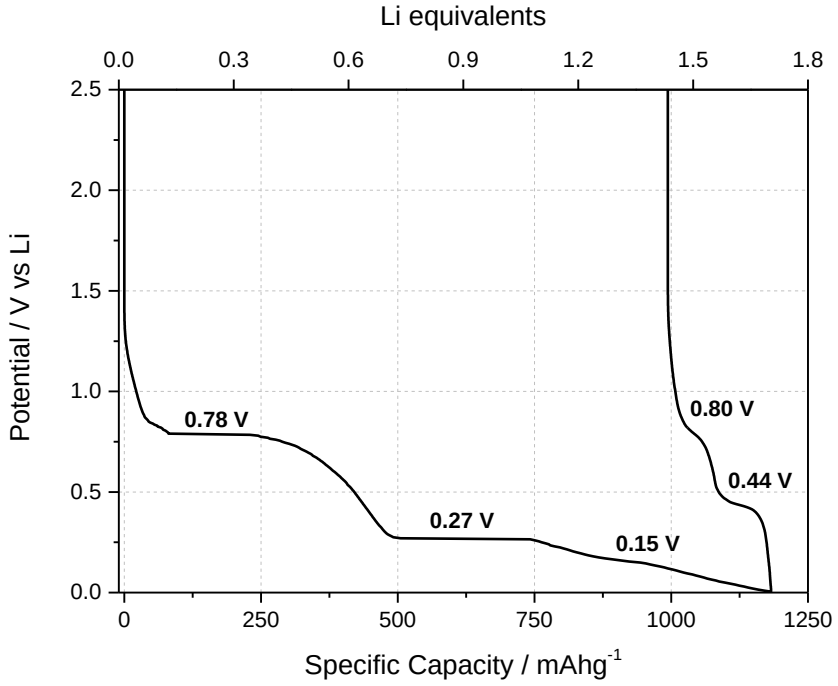

Figure 4.7 - PCGA response of pristine $LiAlH_4$ (LB0D0).

Voltage profiles of the activated alanates (LB1D0 and LB1D05) are given in figure 4.8. Discharge profiles show relevant modifications respect to the pristine sample. In the case of the LB1D0 sample, in the low-potential region, processes at 0.26 and 0.15 V are still observed, but the capacity involved is much lower. On the contrary, in the high-potential region, there is not one stable plateau as in the case of the B0D0 material, but two consecutive processes limited in capacity at about 0.85 and 0.75 V versus Li. Also, upon charging, the fingerprint of two consecutive oxidation reactions is observed.

In the case of LB1D05 sample, the voltage profile is characterized by a sloping plateau below 0.2 V vs. Li without relevant features. While, the electrochemical process around 0.8 V (including the possible decomposition of the electrolyte) is almost absent. The total capacity exchanged upon discharge is similar in value to that achieved with pristine sample. On the contrary, reversibility of the process is slightly enhanced, developing 450 $mAhg^{-1}$ through a short plateau around 0.44 V.

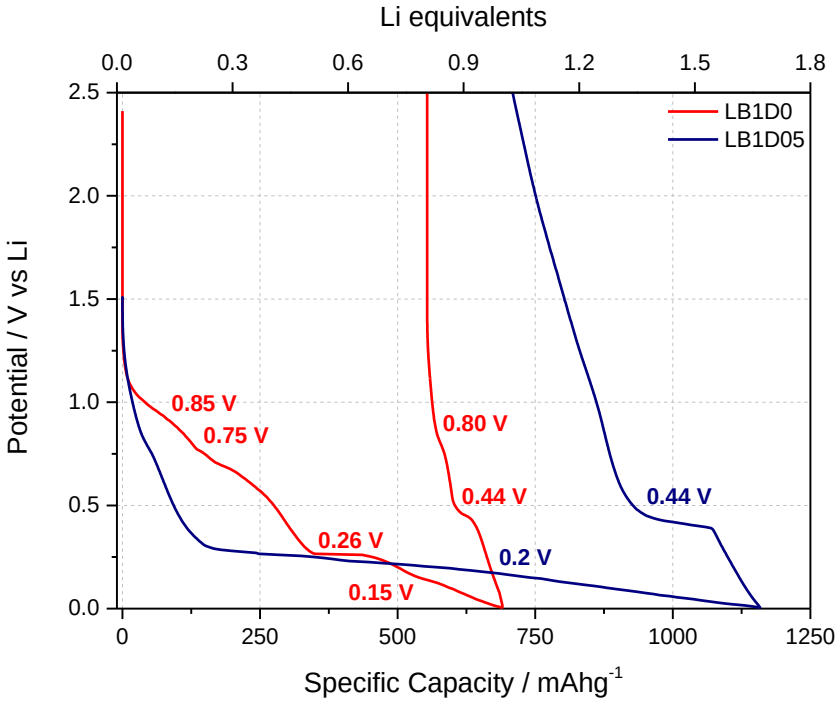

Figure 4.8 - PCGA response of $LiAlH_4$ as a function of mechanochemical treatments: after 1 hour of activation treatment (red) and after additional 30 minutes of ball milling with Super P (navy).

4.4 Study of reaction mechanism in lithium cells

In order to have a direct evidence of the conversion process in lithium cell, *ex-situ* XRD measurements have been performed at MCX beamline in the ELETTRA synchrotron radiation source, Trieste (Italy). Diffraction patterns have been recorded in the 2θ range = 20°- 40°. X-ray energy was 10 keV, corresponding to a wavelength of 1.24 Å.

LB0D0 electrodes have been discharged in lithium cell under galvanostatic conditions, with a C/20 current rate. At the end of discharge, electrodes have been recovered from the cell and washed with dimethylcarbonate. Dried materials were finally sealed in glass capillaries.

Figure 4.9 reports the diffraction patterns of partially (500 mV) and fully discharged (10 mV) $LiAlH_4$ pelletized electrodes. Pristine sample has also been reported as reference. Probably due to electrode thickness, the discharge of these pellets is smaller than those of standard electrodes.

Pristine material consists of monoclinic $LiAlH_4$ with space group $P2_1/c$. Upon whole discharge process, $LiAlH_4$ peaks decrease in intensity and broadened. The powder pattern of electrode discharged at 500 mV shows the appearance of reflections at 2θ = 17.5°, 18°, 25°, 31° and 36°, corresponding to trigonal (SG: R-3) Li_3AlH_6 phase. Again, the (111) and (200) peaks of metallic aluminum are distinguishable at 2θ = 30.7° and 35.7°, respectively. At deeper lithium loading, the peaks of the $LiAlH_4$ phase further decrease whereas those of the Li_3AlH_6 are still well distinguishable. In parallel, the aluminum peaks broaden and decrease in intensity, indicating the possible occurrence of alloying with lithium. This hypothesis is also confirmed by the rise of small peaks at 2θ = 32° and 37.6° possibly assigned to (220) and (311) peaks of the cubic AlLi (S.G.: Fd-3m) phase.

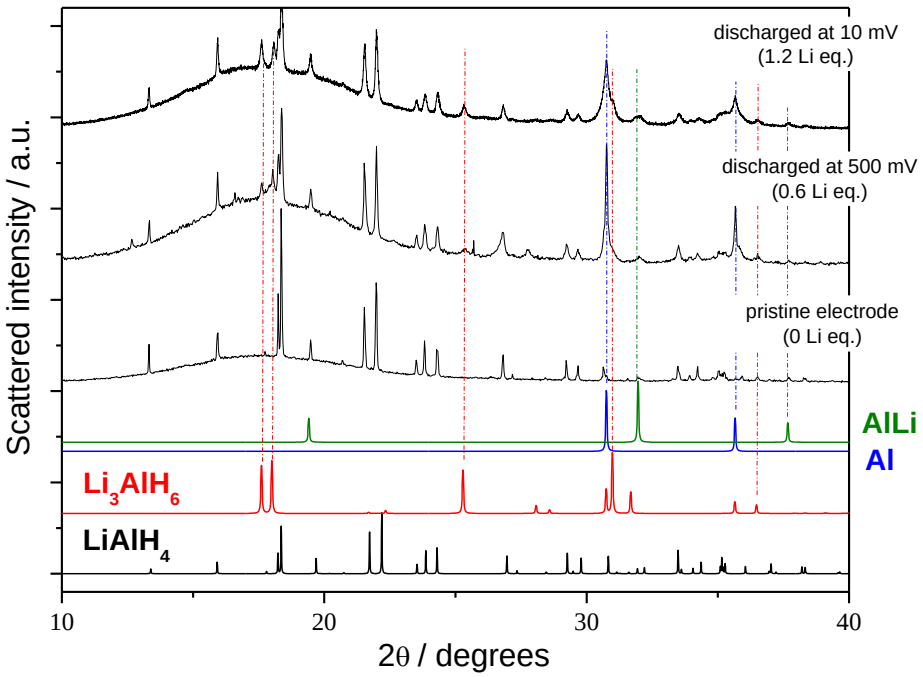

Figure 4.9 - *Ex-situ* synchrotron diffraction experiment of LB0D0 as a function of the discharge. The amount of lithium incorporated in the samples is reported in parentheses.

Comparison of *ex-situ* XRD experiments with PCGA measurements (figure 4.7) allowed to obtain a possible sequence of reactions occurring in a lithium cells.

Discharge of $LiAlH_4$ moves through a 3 steps process. The reaction begins with the formation of hexa-alanate intermediate, according to the following reaction:

$$3LiAlH_4 + 6e^- + 6Li^+ \rightarrow Li_3AlH_6 + 2Al + 6LiH \qquad (1)$$

When 0.29-0.26 V are reached, also Li_3AlH_6 decomposes in LiH and aluminum:

$$Li_3AlH_6 + 3e^- + 3Li^+ \rightleftarrows 6LiH + Al \qquad (2)$$

At potential lower than 0.16 V, the aluminum is alloyed with lithium according to:

$$Al + xe^- + xLi^+ \rightleftarrows AlLi \text{ (or } AlLi_x \text{ } x>1 \text{ phases)} \qquad (3)$$

It's interesting compare these results with DFT calculations reported in chapter 3. Upon discharge, while the reaction (1) occurs in a cell potential range compatible with thermodynamic data, reactions (2) and (3) are downshifted by an overpotential of 0.47 V and

0.15 V, respectively. Such large overpotentials could make thermodynamically plausible the occurrence of metastable reaction path with simultaneous conversion and alloying. In fact, the possible formation of the metastable AlLi phase upon conversion, instead of simple metallic aluminum, decreases the e.m.f. predicted by DFT by approximately 0.15 V.

Upon recharge only two oxidation reactions are observed at 0.44 and 0.78 V (figure 4.7). The first process can be attributed to the de-alloying from the lithium aluminides according to reaction (3), as none of the conversion reactions reported in the chapter 3 are thermodynamically plausible in this potential range. The second charge plateau is compatible with the oxidation to Li_3AlH_6 according to the reaction (2). Finally, there are not experimental evidences of the reformation of $LiAlH_4$. In fact, based on DFT calculations, this reaction occurs at 0.82V vs. Li and therefore is not possible at the observed potentials.

4.5 Study of electrode/electrolyte interface.

An important experimental finding observed is the smaller open-circuit potential (OCP), i.e. 1.55 V vs. Li, measured for electrodes based on sample B1D05 in comparison to the OCP of the other two samples not milled with the Super P additive (2.5-3 V vs. Li). The low OCP and the absence of any electroactive process at 0.8 V versus Li, which is the signature of electrolyte decomposition, can find an explanation in a highly reactive interface between the mechanochemically activated carbon-alanate composite and the LP30 electrolyte. It is well known that thanks to the lability of the Al-H bond, alanates are strong reducing agents, typically used in organic chemistry for carbonyl reduction. LP30 is based on alkyl carbonates, and thus, it may be easily reduced as soon as it comes into contact with the alanate electrode.

The study of the electrolyte/electrode interface has been tackled by means of electrochemical impedance spectroscopy (EIS) and FTIR-ATR spectroscopy.
EIS spectra have been collected on three electrode cell assembled by using a lithium alanate working electrode, and lithium metal disks both as counter and reference electrodes. LP30 electrolyte has been added, the cell closed, taken off the glovebox and quickly the impedance spectra acquisition started. Between each measurement the cells were stored at the open circuit. Figure 4.10 reports the sequence of Nyquist plots collected upon one week of storage.
The impedance data have been fitted with an equivalent circuit represented by a resistance, two couple of resistance and a capacitance parallel (RQ), and a final capacitance, according to: $R_e(R_fQ_f)(R_{ct}Q_{dl})Q_l$.

The sequence relative to LB1D05 electrode describes a rather regular evolution of a non-blocking interface to a blocking one. The as assembled cell spectrum shows one clear high frequency semicircle, followed by a second mid frequency semicircle convoluted with a very sloped line. Upon time the high frequency semicircle resistance increases from around 15 to 50 Ω, the mid frequency process is almost invariable, while the final line has a subsequently more vertical trend. This evolution is compatible with a reactive interface which is progressively passivated from electrolyte decomposition products: the low frequency semicircle represents the growing surface film, the mid frequency one is relative to the charge transfer and the line is indicative of the surface charge accumulation.

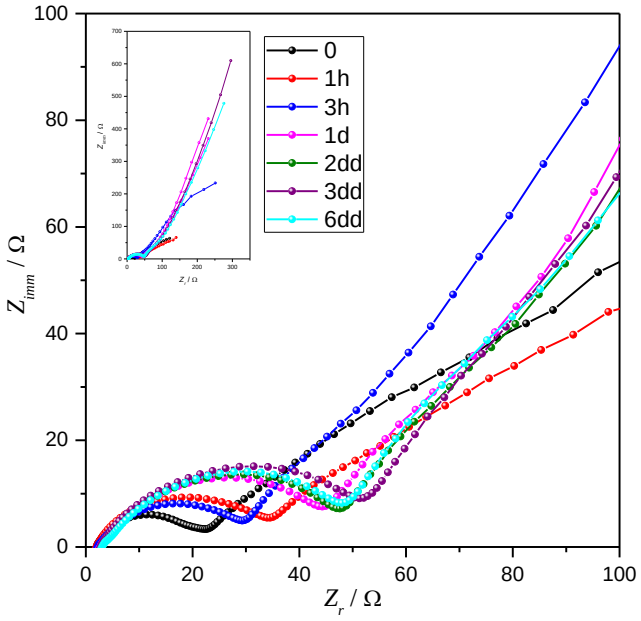

Figure 4.10 - EIS Nyquist plot of a LB1D05 based lithium three-electrode cell. 100 kHz to 50 mHz.

The chemical nature of the surface film has been investigated by FTIR-ATR spectroscopy on B1D05 based electrodes. The FTIR study of the electrode upon aging in LP30 electrolyte is shown in the figure 4.11.

The as prepared material shows the FTIR bands typical of $LiAlH_4$. Specifically, it's observable the Al-H stretching mode at 1757 and 1615 cm^{-1} and the bending of Li-Al-H at 900 and 830 cm^{-1}. Some little peaks due to Li_3AlH_6 are also visible, as the stretching frequency at 1386 cm^{-1}. Whereas bands due to $LiAlH_4$ can be observed in all samples after soaking, those attributable to Li_3AlH_6 disappear after 1 hour.

The $LiAlH_4$-based electrode after 10 minutes of aging in a EC:DMC $LiPF_6$ electrolyte shows the immediate rise of bands between 1650-1610 cm^{-1} and 1080 cm^{-1} likely due to C=O and C-O stretching modes of organic carbonates as well as an IR absorption at about 1190-1200 cm^{-1} possibly due to a C-C-O stretching mode of ester-like organic molecules [56,57].

Moving to the 1 hour aging sample, it is possible to observe the increase of all signals related to the precipitation of organic lithium carbonates and also a band above 1800 cm^{-1} possibly due to the C=O symmetric stretching in complex polymeric species, like linear anhydrides with general formula R-(C=O)-O-(X=O)-R (X= C, Al, P) [58]. On the other hand the appearance of bands at about 1270, 1000, 850 and 780 cm^{-1} suggests the parallel formation of organic phosphates (i.e. $F_{3-x}(RO)_xP=O$) [59,60]. Below 700 cm^{-1} few other weak bands are observed: these are likely related to the phosphate PF_2 bending mode as well as the Al-O

stretching and bending [61]. This picture is confirmed after 5 hours and 3 days of aging. The main change after prolonged aging is the fading of all bands related to organic phosphates apart from the PF_2 bending mode and a slight increase of the Al-O stretching and bending bands.

As above mentioned, lithium aluminum hydride is a strong reducing agent commonly used in organic chemistry synthesis. In fact it is well known that $LiAlH_4$ attacks C=O bonds leading to the formation of alcohols. In the case of esters and similar carbonyl-derived organic species it leads to the C-O bond cleavage to form alcohol in protic media. Similarly organic carbonates are reduced by $LiAlH_4$ to the respective alcohols or diols [62]. In aprotic media like anhydrous EC-DMC blends, despite specific studies are missing, the spontaneous reaction of the solvent molecules with lithium aluminum hydride probably leads to lithium alcoholates such as CH_3OLi or diolates $LiOCH_2CH_2OLi$ [63] together with other complex organic byproducts (lithium carbonates, polymeric anhydrides) and aluminum oxide. Alcoholates are hard nucleophilic species: in particular CH_3OLi is soluble in organic carbonate mixtures and may easily attack the electron poor PF_5 molecule, being the latter an unavoidable minor component of the electrolyte mixture due to the spontaneous equilibrium $LiPF_6$=LiF+PF_5 [64]. In our hypothesis the reaction sequence thus leads to the spontaneous precipitation of to fluoroalkyl phosphates, i.e. $F_3(RO)_{3-x}P=O$, that are insoluble byproducts in a EC-DMC solvent blend [14,15]. Upon aging these heterogeneous byproducts accumulates on the $LiAlH_4$ electrode surface resulting in a continuous complex film formed by insoluble organic lithium carbonates, complex polymeric anhydrides, fluoroalkylphosphates and aluminum oxide. The reaction sequence ends when this composite film is capable to prevent the reduction of further organic carbonate molecules to lithium alcoholates. The film formed is in conclusion analogous to the SEI commonly formed on the surface of all the negative electrodes, capable to prevent further electrolyte reduction, still permitting the electrodic processes evolution.

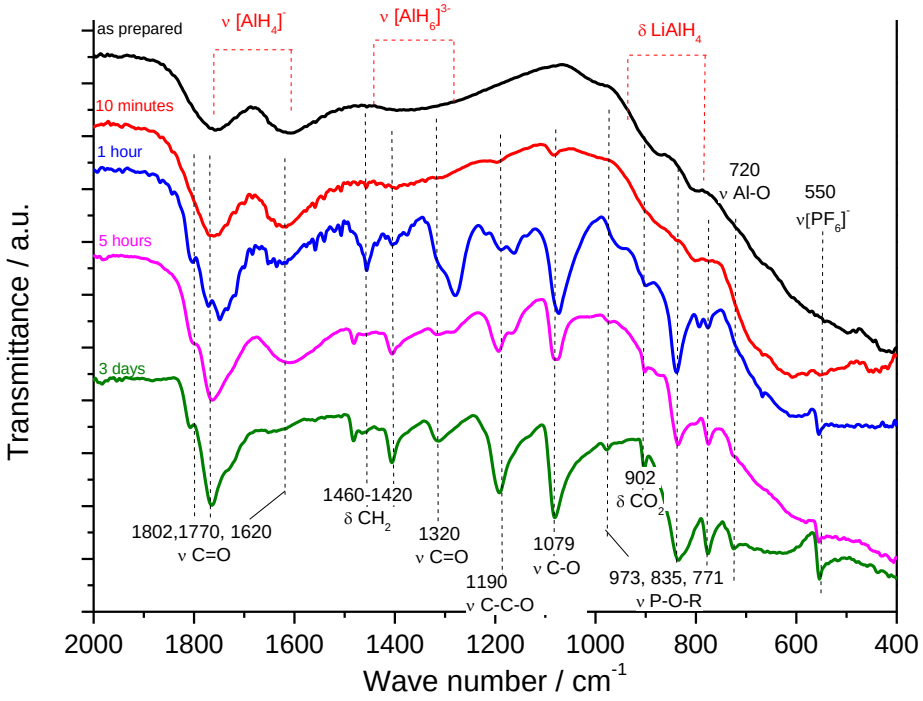

Figure 4.11 - ATR-FTIR spectra evolution of LB1D05 electrode as a function of soaking time into the LP30 electrolyte.

4.6 Conclusions

The electrochemical behavior of $LiAlH_4$ in a lithium cell has been reported. Although the high theoretical capacity, approximately 1150 $mAhg^{-1}$ are achieved upon first discharge. A short activation step, the alanate ball milling with carbon, has beneficial effects on the cell efficiency, increasing to 39% from 16% of the pristine material. On the other hand, prolonged milling time causes the complete decomposition of $LiAlH_4$ in the corresponding hexa-alanate.
In analogy with $LiAlH_4$ thermal de-hydrogenation process, Li_3AlH_6 is also the intermediate product of a multistep conversion mechanism that finally evolves towards the complete decomposition to LiH and Al. Furthermore, at deepest lithium loading lithium and aluminum can react to form the alloy compound AlLi. As expected, the whole process is only partially reversible. In fact there is no evidence about the re-conversion of Li_3AlH_6 in $LiAlH_4$.
Overpotentials play a very important role in the conversion of lithium alanates. It's well known that high overpotentials and large hysteresis are very common among the conversion reactions of oxides, phosphides, and other classes of materials. In the case of hydrides, previous reports suggested a limited hysteresis for this class of materials due to the limited overpotentials (<0.2V) observed for magnesium hydride [15–17]. Contrary to MgH_2, Li_3AlH_6 conversion is affected by a very high overpotential (>0.45V), calculated with respect to the DFT estimated thermodynamic potentials. Such a huge overpotential can have a multifactor origin probably related to 1) poor electronic conductivity, 2) surface passivation, and 3) complex reaction path. This last issue could be the key for the apparent irreversible conversion of $LiAlH_4$ into Li_3AlH_6. According to reaction (2), Li_3AlH_6 oxidation involves six electrons and three species (Li_3AlH_6, LiH, and Al) for nine overall formula units. Such complexity can justify an overpotential so huge to make the reaction incomplete in the potential window of interest. In addition to the intrinsic incomplete reversibility of the conversion reaction, the origin of the capacity inefficiency could be attributed to the huge volume variation associated with the conversion (~30%) and alloying (~100%). As a matter of fact, the better rechargeability of the electrodes based on the alanate milled with carbon suggest that carbon can act as buffer and a good mixing can improve the electrode stability.
Investigations on the reactivity of electrodes surface with electrolyte have highlighted the formation of a stable and properly conductive passivation layer. A direct chemical interaction substitutes the electrochemical decomposition of the electrolyte, implying the formation of the SEI at the expanses of the discharged capacity, but with the advantage of non-contributing to cell inefficiency.

5

Li_3AlH_6

5.1 Synthesis of the sample

The direct synthesis of Li_3AlH_6 has been performed by mechanochemistry. $LiAlH_4$ and LiH powders have been used in stoichiometric amounts, according to:

$$LiAlH_4 + 2LiH \rightarrow Li_3AlH_6 \qquad (1)$$

The mixture has been milled in a shaker mill apparatus for 15 hours under inert atmosphere. Experimental conditions used for ball milling are the same adopted for $LiAlH_4$ samples preparation.
Addition of Super P has been performed mixing it with synthesized alanate in mortar.

Sample has been label S15 to indicates duration of mechanochemical synthesis and D0 to indicates addition of Super P by physical mixing in mortar.

5.2 Physical-chemical characterization

The initial mixture of the reagents appeared light gray. After 15 hours of milling, the color became darker indicating that a reaction took place. At end of milling sessions, the powder resulted very reactive.

The nature of the as synthesized material has been investigated by synchrotron radiation diffraction and Infrared Spectroscopy.

Figure 5.1 shows diffraction data of Li_3AlH_6 sample. ICSD 99217 pattern has been used as reference [65]. Li_3AlH_6 diffraction pattern has been recorded at the MCX beamline in the ELETTRA synchrotron radiation source with an X-ray energy of 10 keV corresponding to a wavelength of 1.24 Å. Diffraction pattern has been acquired in the range of $15° < 2\theta < 70°$.

Ball milling produced pure Li_3AlH_6 phase. No peaks associated to initial compounds, i.e. LiH and $LiAlH_4$, are visible. It's worth to note the absence of metallic aluminum peaks, indicating that the milling session didn't decompose the sample. Possibly, LiH may repress the thermal decomposition of $LiAlH_4$ to give Li_3AlH_6 and H_2.

Structural and microstructural properties of the sample have been analyzed by Rietveld method.

It crystallizes according to the trigonal R-3 space group. The unit cell dimensions from the fit are a = 8.1168 Å and b = 9.5836 Å and the crystallite average dimension is 36 ± 8 nm.

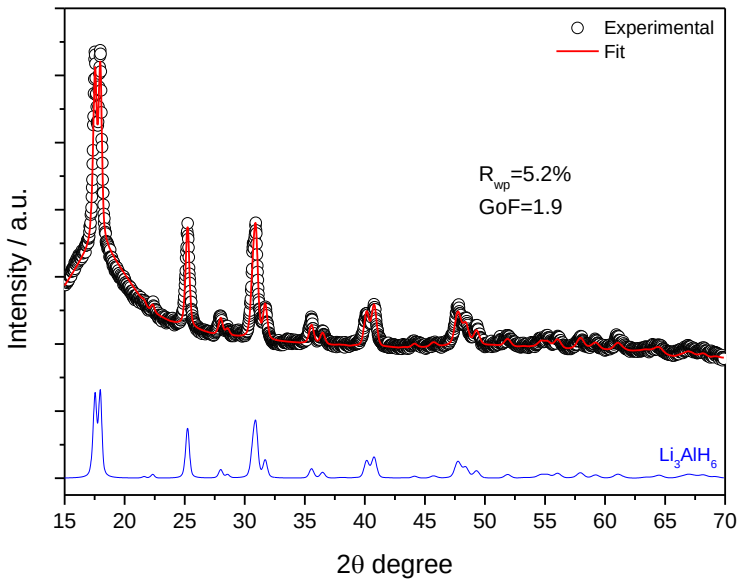

Figure 5.1 - Pattern refinement of Li_3AlH_6 phase. All peaks were indexed by ICSD 99217 pattern.

FTIR analysis has been performed by the use of a Bruker Alpha spectrometer. All spectra were recorded in the wave number range between 2000 and 400 cm^{-1}, in transmission mode, at room temperature. The sample, as fine powder, was mixed with KBr in a 1:100 weight ratio (powder to KBr respectively) and then hand pressed in pellets by a Pike die set. Figure 5.2 shows the FTIR spectrum acquired for the synthesized sample. It exhibits the typical vibrational modes associated to Li_3AlH_6. The region between 1386 and 1276 cm^{-1} is associated to Al-H stretching frequencies and the peaks at 1000, 950 and 859 cm^{-1} are the Al-H bending frequencies.

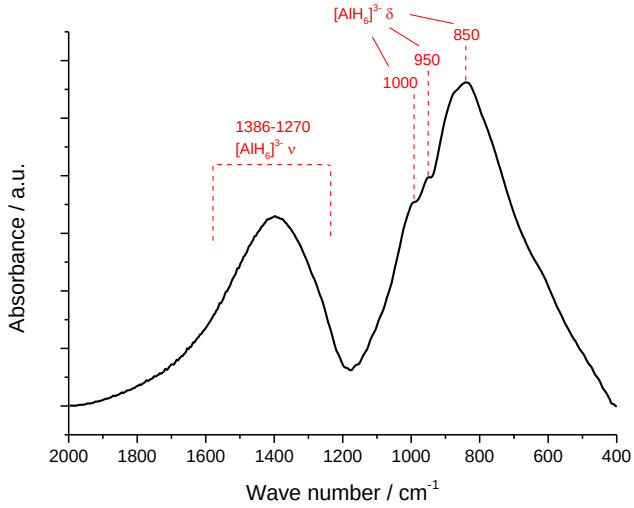

Figure 5.2 - FTIR spectrum of synthesized Li_3AlH_6

Morphological analysis reveals that Li_3AlH_6 consists of aggregates of round-shaped nanoparticles with diameters ranging from 50 to 200 nm, as shown in figure 5.3.

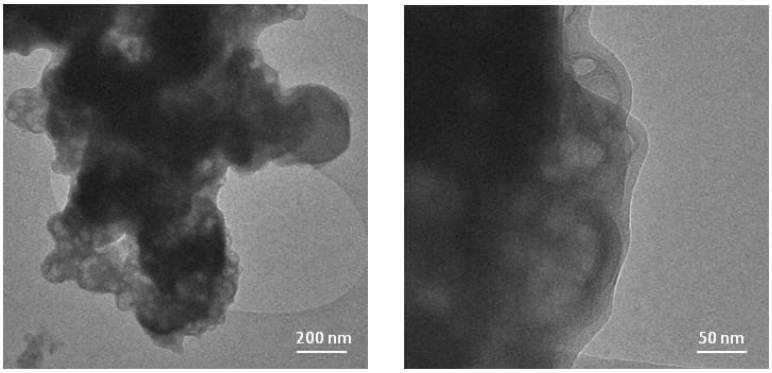

Figure 5.3 - TEM micrographs of LS15 sample.

5.3 Electrochemical characterization

Electrodes and cells have been prepared according to the procedures described in chapter 4.

In figure 5.4, there is the potential profile of the first discharge/recharge cycle of LS15D0 sample. The discharge evolves through a small process centered around 0.88 V, a stable plateau at 0.29 V, followed by a long sloping reduction down to the cut-off potential. The final delivered capacity is approximately 900 $mAhg^{-1}$ corresponding to 1.81 lithium equivalent incorporation, to be compared to the 3 lithium equivalents theoretically available. The recharge appears very poor, only 22% of the discharged capacity is recovered on charge, corresponding to 0.4 lithium equivalents extraction. Anyway, two little slopes can be detected at 0.44 and 0.78 V.

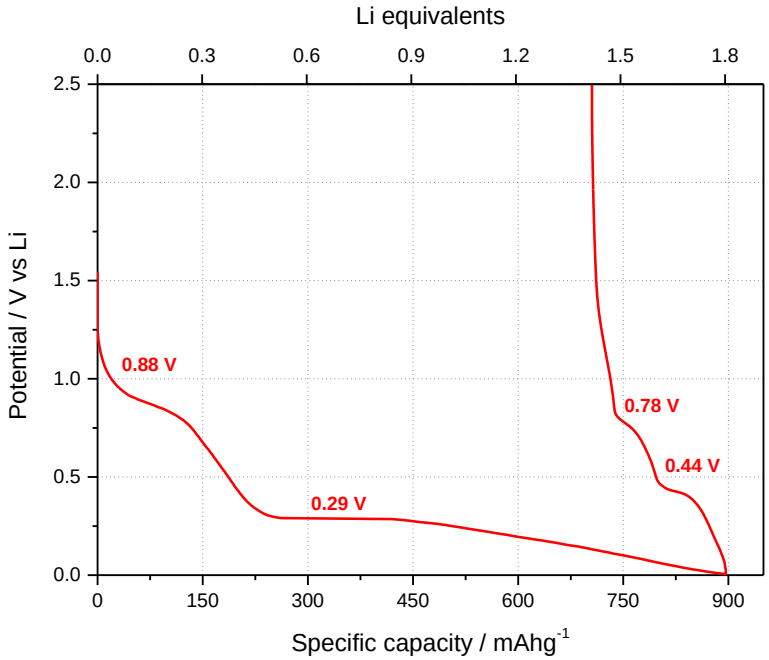

Figure 5.4 - Potential vs. Specific Capacity plot of LS15D0 sample acquired in PCGA mode.

On the basis of DFT data reported in chapter 3 and PCGA results, it's possible to outline a reaction sequence for Li_3AlH_6. The first limited reduction occurs at a potential (0.88 V vs. Li) that is not compatible with the reduction of Li_3AlH_6 to LiH + Al (predicted to 0.74 V). On the contrary, it may be related to electrolyte decomposition, which typically occurs in that potential region on the Super P surface. The plateau at 0.29 V versus Li is very similar to the plateau at 0.26 V versus Li observed for the $LiAlH_4$ sample (see Figure 4.7). This reaction may be related to the reduction of Li_3AlH_6 to LiH and Al downshifted by an overpotential of 0.45 V. Furthermore, it cannot be excluded the formation of AlLi instead of metallic aluminum. However, this reaction plateau gently becomes

sloping and ends only at the cathodic cutoff voltage without further pseudoplateaus, which is different to the case of $LiAlH_4$. Nevertheless, the charge profile is very similar to $LiAlH_4$, exhibiting the same plateaus. Therefore, it's expected a similar reaction path upon oxidation.
It is worth noting that the presence of the electrolyte decomposition around 0.88V vs. Li is a clear indication of the lower reactivity of the hexa-alanate towards the electrolyte than the $LiAlH_4$.

5.4 Conclusions

Li_3AlH_6 has been prepared by ball milling. The studies revealed that a pure phase has been obtained with this method. Electrochemical tests demonstrated that lithium hexa-alanate is active electrochemically, but its performance are very poor, developing just the 60 % of the theoretical capacity upon first discharge and low charge efficiency. As the intrinsic reversibility of the hexa-alanate has already been demonstrated, the main reason for low rechargeability must consist in the mechanical instability of the electrode and of the SEI as a consequence of volume variations. A better mixing of the hydride with the carbon additive could be a first improvement step.

SODIUM ALANATES

6

$NaAlH_4$

6.1 Samples preparation

$NaAlH_4$ samples have been prepared following the procedure described in chapter 4. The bare alanate has been labeled as NB0, while sample after activation step of 1 or 15 hours as NB1 and NB15, respectively.

Addition of Super P has been carried out by mixing with mortar and pestle for samples NB0D0 and NB15D0 and by further HEBM for sample NB1D05 and NB15D5. In table 6.1 there is the list of prepared samples.

Table 6.1 - Scheme of sodium alanate samples under investigation.

Name	Label	Time of HEBM (h)	Addition of SuperP	Time of HEBM with SuperP (h)
$NaAlH_4$	NB0	0	no	/
	NB0D0	0	yes	0
	NB1	1	no	/
	NB1D05	1	yes	0.5
	NB15	15	no	/
	NB15D0	15	yes	0
	NB15D5	15	yes	5

6.2 Physical-chemical characterization

Phase composition and crystal structure of prepared $NaAlH_4$ samples have been studied by X-ray diffraction. XRD patterns have been collected in a borosilicate capillary sample holder in a Rigaku Ultima+ Diffractometer, equipped with Cu Kα source in a theta-theta Bragg-Brentano geometry. Diffraction pattern has been acquired in the 2θ range = 15°- 60° with a step of 0.02° and a t/step of 5 sec. Diffraction pattern has been refined by Maud program [51] using ICSD 154907 as reference. Figure 6.1 shows experimental and fitted patterns for pristine material (B0).

The starting material consists of pure $NaAlH_4$. It crystallizes according to the tetragonal space group $I4_1/a$, with lattice constant a = 5.0062 Å and c = 11.3163 Å. The crystallite average dimension is equal to 110 nm.

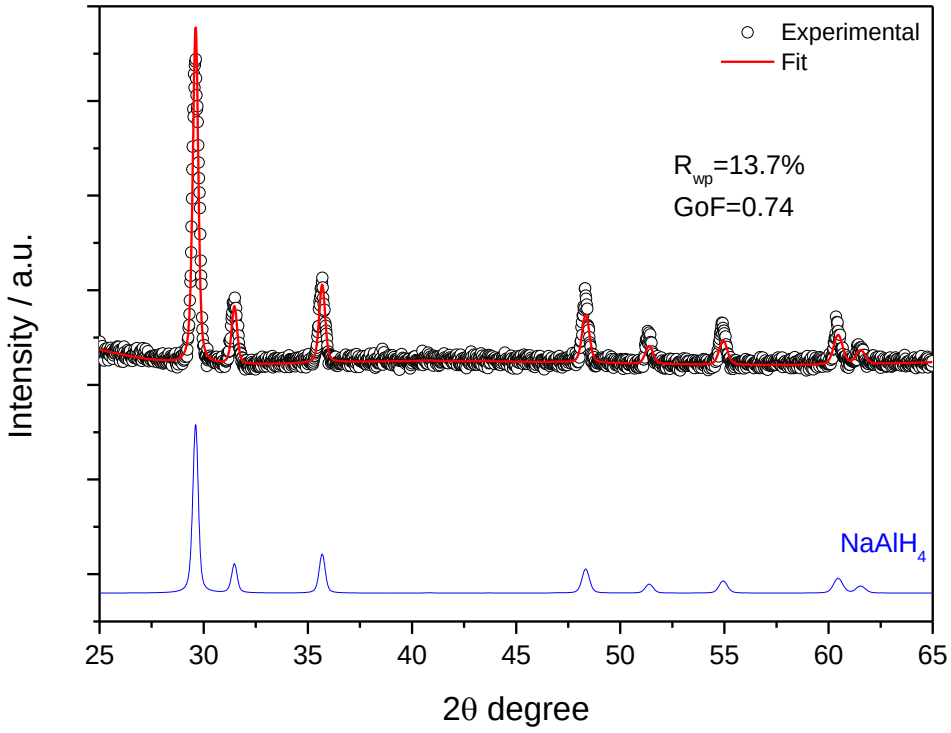

Figure 6.1 - Pattern refinement of bare $NaAlH_4$. Experimental pattern is black circle, fitting pattern is red line and reference pattern is the blue line.

Figure 6.2 reports XRD patterns collected as a function of mechanochemical treatments. 1 hour of ball milling (NB1 sample) doesn't have a significant impact on micro-cristallinity. While, 15 hours of ball milling (NB15 sample) causes decreasing in intensity of $NaAlH_4$ peaks. The analysis of peak width shows a decrease of the average crystalline domain size to 30 nm. In the NB15D5 sample,

peaks intensity is greatly decreased. Furthermore, diffraction lines present at 2θ = 38.5° and 44.7° correspond to the main (111) and (200) peaks of cubic Fm-3m aluminum.

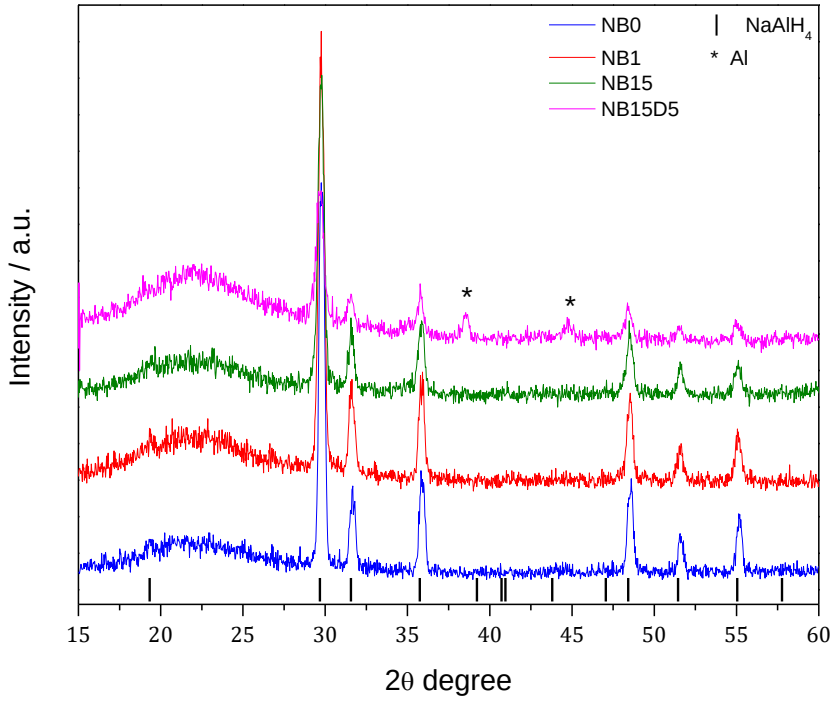

Figure 6.2 - XRD patterns of $NaAlH_4$ samples as a function of mechanochemical treatments.

To obtain further information of the milling effect on $NaAlH_4$ samples, FTIR analysis has been performed. FTIR spectra have been acquired by a JascoFTIR-300 apparatus. All spectra have been recorded at room temperature, in transmission mode, in the wave number range between 2000 and 400 cm^{-1}. Samples, as fine powders, have been mixed with CsI in a ratio of 1:100 mg (powder to CsI respectively) and then pressed in pellets by a Pike die set and hand-press. FTIR assignments have been done by comparing with literature data [55].

Figure 6.3 shows the vibrational features of samples subjected to 1 hour of ball milling (NB1 and NB1D05). Pristine sample, NB0, has been used as control sample.

B0 sample spectrum is characterized by the Al-H stretching modes centered at 1675, 1372 (weak) and two clear Na-Al-H bending modes at 904, 727 and 690 cm^{-1}. B1 have almost the same spectrum. Al-H stretching mode at 1675 cm^{-1} is slightly shifted to 1685 cm^{-1} and the little peak at 1372 cm^{-1} is broadened. In the region of bending frequencies, the shoulder at 690 cm^{-1} is more evident. NB1D05 sample (carbon added) shows the appearance of little peaks associable to vibrational modes of Na_3AlH_6. Specifically, $[AlH_6]^{3-}$ stretching modes at 1430 and 1265 cm^{-1} and bending frequencies around 1000 cm^{-1}.

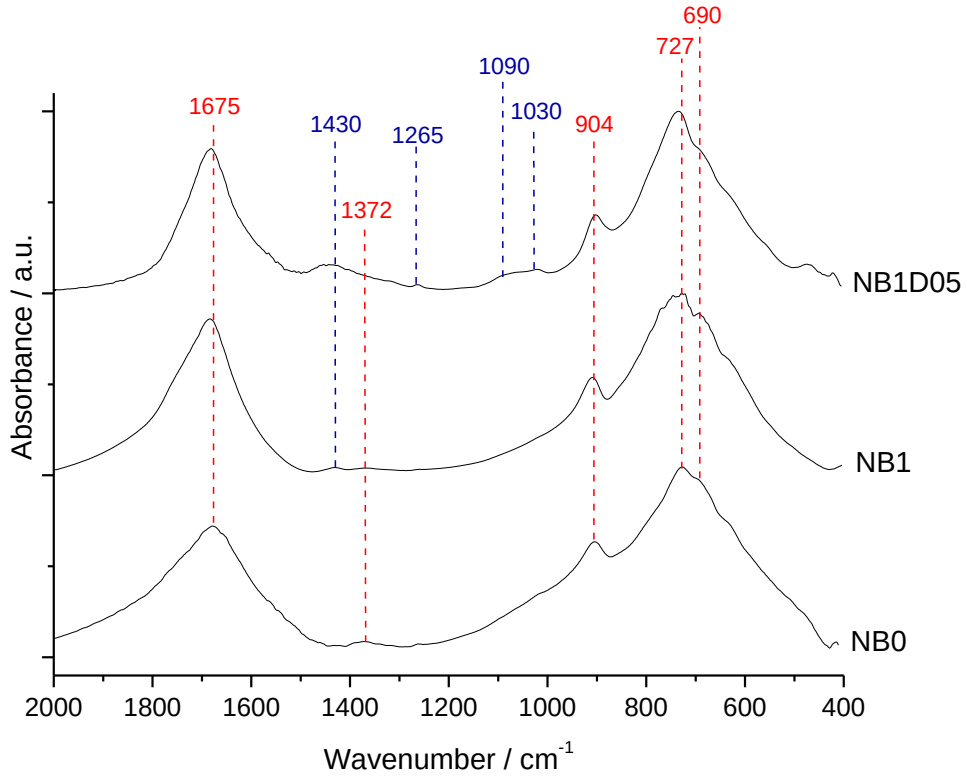

Figure 6.3 - FTIR spectra of $NaAlH_4$ samples after 1 hour of ball milling. Pristine sample (NB0) was used as reference.

FTIR spectra of the samples after 15 hours of ball milling is shown in figure 6.4. Beside the typical vibrational modes of $NaAlH_4$, NB15 and NB15D5 samples shows the typical signals of Na_3AlH_6. In the NB15 sample, just two little peaks at 1262 and 1030 cm^{-1}, corresponding to the bending mode of Na_3AlH_6, can be detected. In the NB15D5 sample, Na_3AlH_6 features become more evident: stretching at 1430 and 1262 cm^{-1} and bending at 1170, 1090 and 1030 cm^{-1} frequencies.

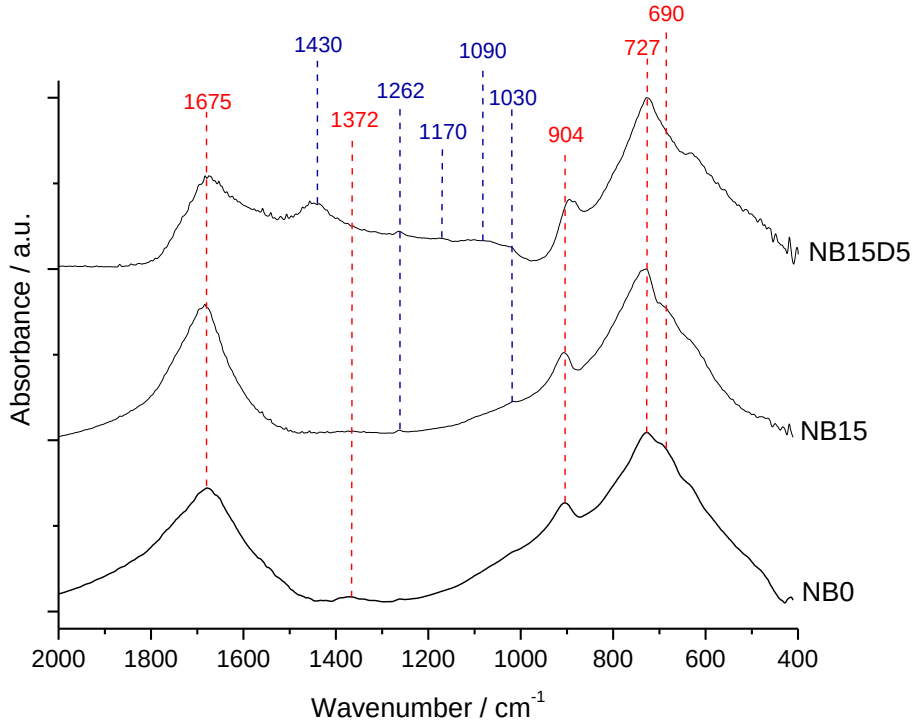

Figure 6.4 - FTIR spectra of $NaAlH_4$ samples after 15 hours of ball milling. Pristine sample (NB0) was used as reference.

From the morphological point of view, the effect of milling has been evaluated by TEM analysis. Micrographs have been collected using a FEI Tecnai 200 kV cryo-TEM instrument. In order to prevent sample damaging due to the interaction with the electron beam, TEM experiments have been carried out at 80 keV in cryo-condition by cooling the temperature of the sample holder to liquid nitrogen.

TEM micrographs are reported in figures 6.5 and 6.6. The pristine commercial sample (NB0) results constituted by regular sub-micrometric prismatic particles (figure 6.5a) with well-defined boundaries either at low and high enlargements. After ball milling, the bare alanate still presents a regular shape and the particles size progressively decreases with the extension of milling time.

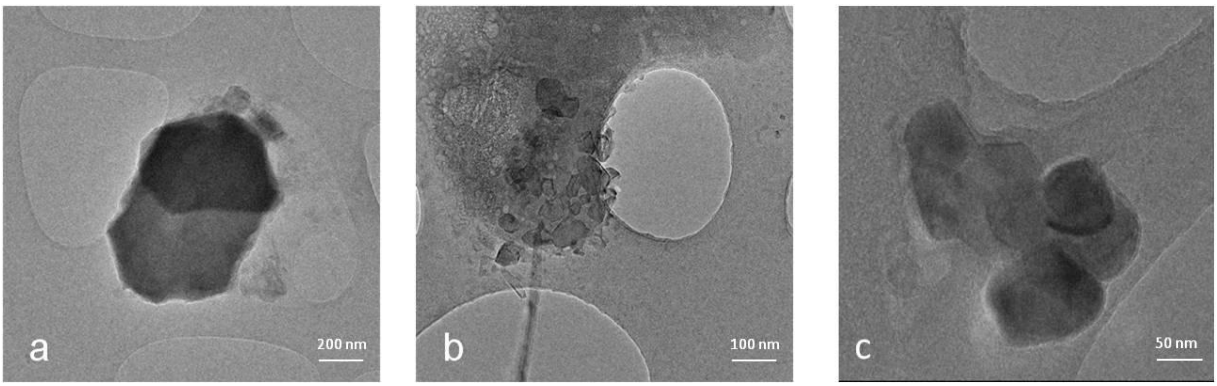

Figure 6.5 - TEM micrographs of $NaAlH_4$ samples: a) NB0, b) NB1 and c) NB15.

Samples produced by milling with Super P (NB1D05 and NB15D5) exhibit a completely different morphology. An amorphous composite is present: the pristine alanates morphology is not recognizable anymore and, interestingly, no traces of the characteristic spherical morphology of Super P is evident [17].

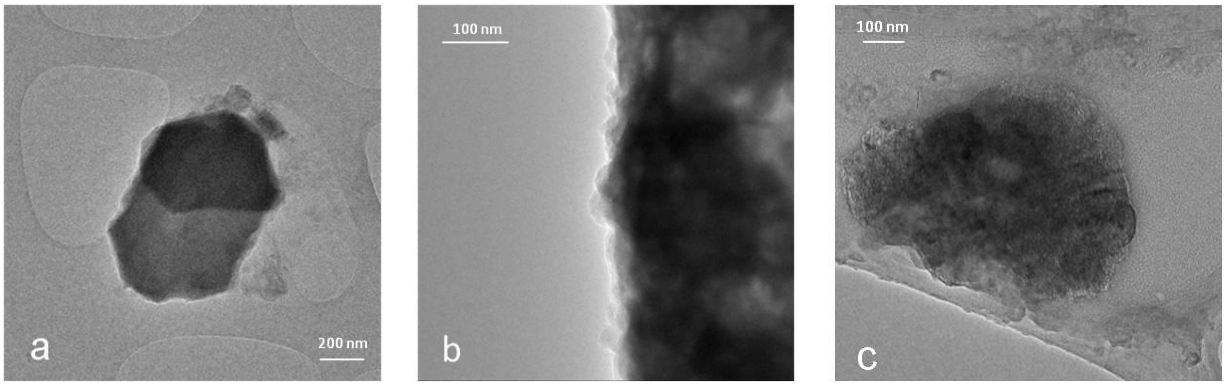

Figure 6.6 - TEM micrographs of $NaAlH_4$ samples: a) NB0, b) NB1D05 and c) NB15D5.

Preliminary analysis of the samples shows that the ball milling of the bare alanate results in a progressive decrease of the average crystallite size from 110 nm to 30 nm (mean particle diameter) for NB0 and NB15 samples, respectively. Just minor traces of the hexahydride Na_3AlH_6 are detected with FTIR spectroscopy in NB15D5, while it's probably too poorly crystalline to be observed by XRD. On the other hand, prolonged mechanochemical treatment performed in addition to Super P seems to promote the decomposition of $NaAlH_4$. The Al evidence is provided by XRD, while Na_3AlH_6 by FTIR. Clearly, the catalytic effect of carbon intimately dispersed with alanate and the local overheating developing upon milling could lead to hydrogen desorption according to the reaction:

$$NaAlH_4 \rightleftarrows 1/3\ \alpha\text{-}Na_3AlH_6 + 2/3Al + H_2 \quad (1)$$

Nevertheless, $NaAlH_4$ is preserved as main phase in B15D5 sample, in contrast with the observation on $LiAlH_4$. Therefore, only pristine and B15 samples have been used for electrochemical characterization.

6.3 Electrochemical characterization

The $NaAlH_4$ capability to sustain a lithium driven electrochemical process and the effects of the mechanochemical treatments on this have been tested carrying out PCGA tests. Details on electrodes preparation procedure are in chapter 4.

Figure 6.7 reports the electrochemical response of pristine sodium alanate. The potential profile of NB0D0 sample is characterized by three plateau around 0.41, 0.26 and 0.17 V vs. Li upon discharge. An overall specific capacity of 1800 $mAhg^{-1}$ is reached at the end of first discharge, corresponding to more than 3.5 lithium equivalents over the theoretical 4. Furthermore, it's evident also a short plateau centered around 0.8 V versus Li, corresponding to the electrolyte decomposition on the electrode surface. Finally, recharge efficiency is lower than 30%, and only one lithium equivalent is given back, through a two-step process evolving around 0.40 and 0.47 V versus Li.

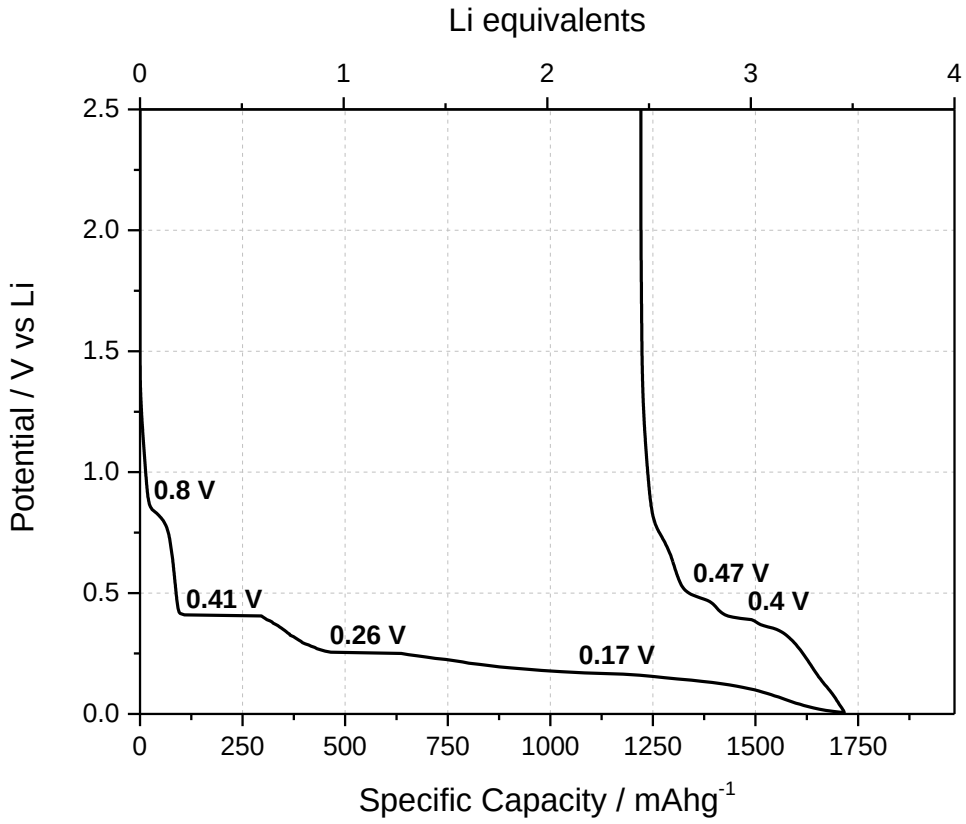

Figure 6.7 - PCGA responses of pristine $NaAlH_4$ sample (NB0D0).

The electrochemical performance of sodium alanate based electrodes as function of ball milling is given in figure 6.8. Compared with NB0D0, sample subjected to 15 hours of ball milling (NB15D0) show a similar potential profile. Discharge develops in the same three plateaus, with almost the same specific capacity. Apparently, the mechanochemical activation does not affect the reaction

sequence but widens the length of the conversion plateau, thus suggesting an improved electrochemical activity of the sodium alanate. In fact, the amount of lithium loading occurred above 0.25 V versus Li increases from 1.28 Li eq for sample NB0D0 to approximately 2 Li eq for samples NB15D0. The additional step of ball milling with the carbon have a large impact on electrochemical performance of $NaAlH_4$. NB15D5 sample is still able to react with 3.5 Li equivalents upon discharge but give back 2.5 Li equivalents upon charge. The conversion reversibility is drastically enhanced, and a much greater capacity is delivered back on charge (2.5 Li eq), with a Coulombic efficiency close to 70%.

Again, the voltage profile is strongly modified when compared to NB0D0. The electrochemical process at about 0.8 V versus Li due to the electrolyte decomposition does not occur. Upon reduction, sample NB15D5 exhibits short plateaus at 0.62, 0.37, 0.24, and finally 0.18 V versus Li. Also, the charge profile is modified and in addition to the process occurring at about 0.46 V versus Li, there is a sloping oxidation around 0.8 V versus Li.

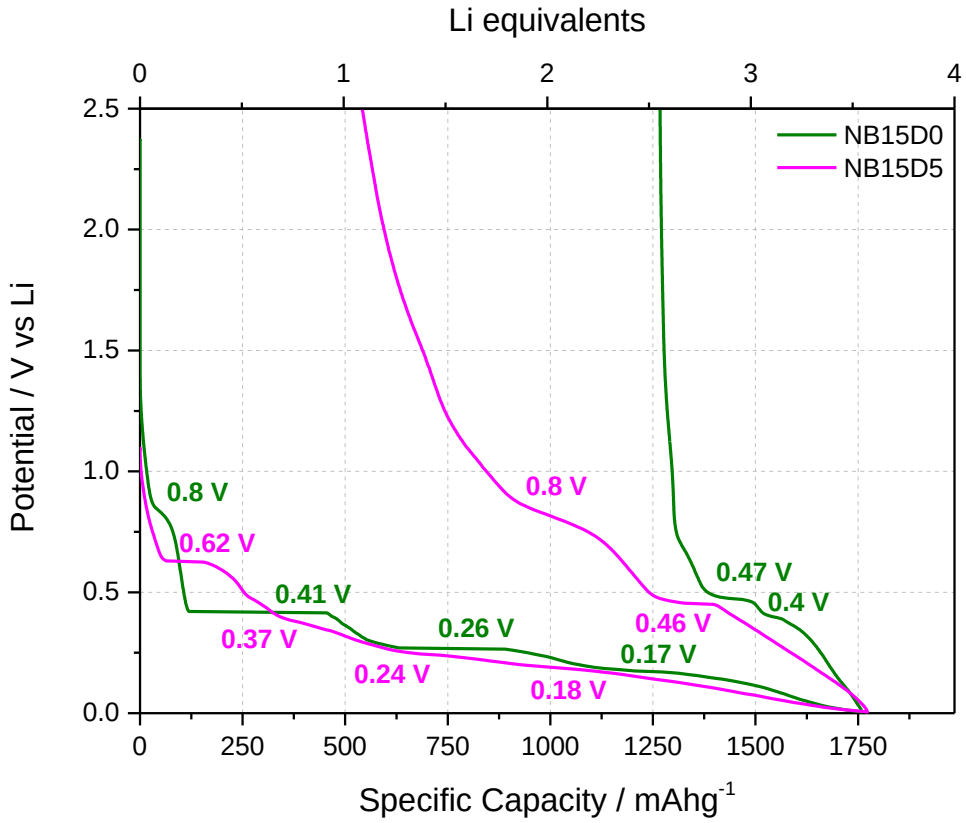

Figure 6.8 - PCGA responses of $NaAlH_4$ samples as function of ball milling time.

6.4 Study of electrode/electrolyte interface

As already described in chapter 4, all the cells assembled with ball milled materials exhibits a low open circuit voltage respect to the pristine samples and the process around 0.8 V, associated to the electrolyte decomposition, was not observed. The origin of this phenomenon could come from the interaction of electrolyte solution with electrode surface. It should be reminded that alanates are strong reducing agents used in organic chemistry to reduce carbonyl and carboxyl groups, and standard electrolyte LP30 used for all the electrochemical measure in this thesis is based on carbonates solution.

Following the procedure described in chapter 4, the superficial reactivity of NB15D5 sodium alanate with the standard electrolyte LP30 has been investigated by Infrared spectroscopy and electrochemical impedance spectroscopy. FTIR experiments have been conducted in attenuated reflection mode and the spectra have been acquired soaking alanate-based electrode in electrolyte solution for 10 minutes, 1 hour, 5 hours and 3 days and then they have been washed with dimethyl carbonate and dried under vacuum.

Figure 6.9 shows the Nyquist plots obtained from the measurement of $NaAlH_4$ electrodes stored at OCP in LP30 for a week. In analogy with $LiAlH_4$, $NaAlH_4$ interface can be described by an R(RQ)(RQ)Q circuit. The spectrum describes a not blocking interface. At t=0, impedance curve shows a semicircle in the high frequencies region, which could be attributed to the resistance of the SEI; followed by a very large semicircle convoluted with a line, in the mid-low frequencies range. The high frequency resistance is calculated to be approximately 30 Ω. After 1 day, this value constantly increases until 78 Ω and then decreases again to 30 Ω after 6 days. These fluctuations in the R_{SEI} values can be associated to an unstable film formed on the electrode surface, which continuously grows, breaks and grows again.

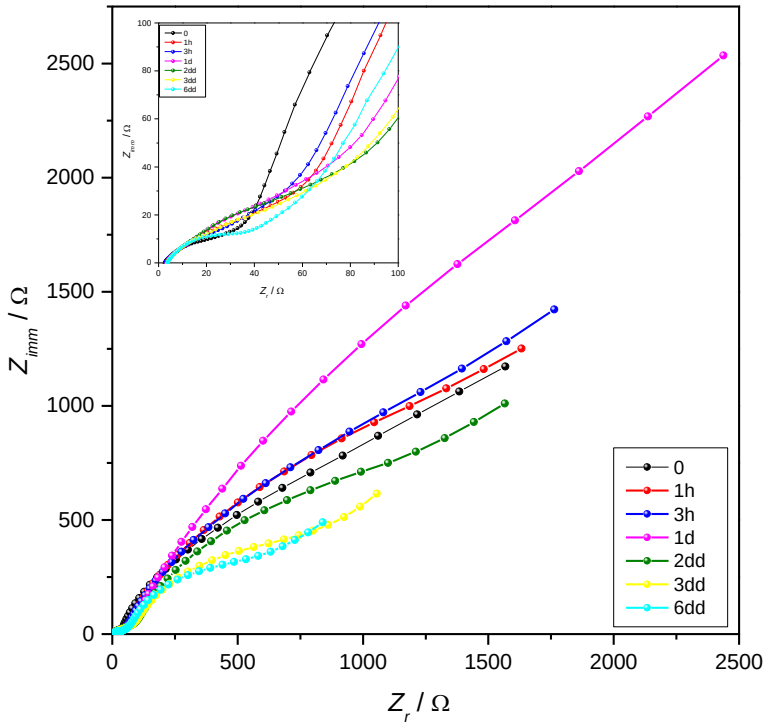

Figure 6.9 - Nyquist Plot of NB15D5 sample.

FTIR-ATR spectra as function of aging time in the electrolyte solution are given in figure 6.10. As prepared electrode has been used as reference. It exhibits the typical vibrational frequencies of $NaAlH_4$: $[AlH_4]^-$ stretching mode at 1648 cm^{-1} and the bending at 900 and 712 cm^{-1}. Beside them, Na_3AlH_6 peaks are also observable. Specifically, stretching at 1400 cm^{-1} and bending around 1189 and 1081 cm^{-1}.

LP30 decomposition starts as soon as it come in contact with $NaAlH_4$. After only 10 minutes, vibrational frequencies associated with alanates disappear and wide vibrational modes are observable from the spectrum. As already observed for lithium alanate, the electrode surface is covered by a complex film, which include insoluble organic lithium carbonates, polymeric anhydrides, fluoro-alkyl phosphates and aluminum oxides. Specifically, at 1803 and 1750 cm^{-1} are visible the stretching modes of the C=O groups and at 1272 cm^{-1} the C-O stretching relative to carbonates. It's also observable the frequencies associated to the fluoro-alkyl phosphates: νP=O at 1195 and 1159 cm^{-1}; ν P-O-C at 1066 and 968 cm^{-1}; and ν P-O at 796 and 774 cm^{-1}. Also, at 640 cm^{-1} there is the appearance of aluminum oxides stretching mode. After 1 hour, peaks appear reduced in intensities. Also, prolonging the aging time, signals constantly changes in intensities.

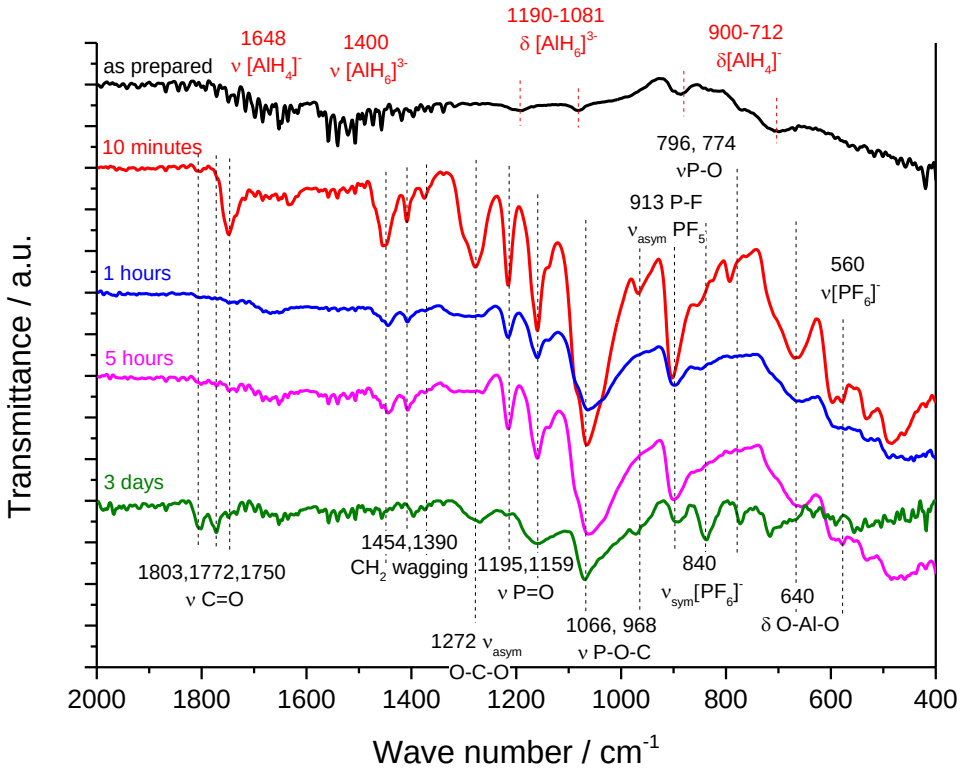

Figure 6.10 - FTIR-ATR spectra of NB15D5 upon aging in LP30 electrolyte.

In conclusion, the electrode/electrolyte interface is highly reactive. Sodium alanate, thanks to its high reducing power, largely reacts with the electrolyte solution and several reaction products are deposited on the electrode surface. This process continuously evolves upon time and surface renovation is involved. In contrast to the evidence obtained with lithium alanate, it's not evident the formation of a stable film on the electrode surface. Probably, the different behavior can be associated to the prolonged mechanochemical treatments to which $NaAlH_4$ has been subjected. The enhanced surface area resulted from prolonged time of ball milling as well as the catalytic effect of the carbon coating causes this extended superficial reactivity and not allow the deposition of a stable film.

6.5 Advanced characterization

As described above, $NaAlH_4$ showed interesting electrochemical performance, reaching almost all the theoretical capacity during first discharge. However, $NaAlH_4$ electrodes suffers from poor cycle efficiency, probably due to the severe volume expansion following the conversion reaction and it can result in damage to electrode mechanical integrity with loss of electrical contact. Mechanochemical treatments (i.e. NB15D5 sample) demonstrated the ability to mitigate these deleterious effects and charge efficiency rises to 70%. Therefore, further analyses have been performed on $NaAlH_4$ samples to better understand the role of mechanochemical treatments on the properties of $NaAlH_4$. In particular, solid state NMR has been used to examine the local structure of samples under investigation and Thermal Programmed Desorption (TPD) analysis to evaluate their hydrogen content and their desorption properties. Finally, the electrochemical features have been analyzed by combining potentiodynamic cycling with galvanostatic acceleration with electrochemical impedance spectroscopy measurements. The effects of carbon and milling have been reported by comparing NB15D5 sample with the pristine $NaAlH_4$ (NB0), $NaAlH_4$ sample ball milled for 15 hours (NB15) and the mixture of $NaAlH_4$ and Super P, obtained by hand grinding in mortar (NB0D0).

6.5-1 Solid State NMR experiments

Static and magic angle spinning nuclear magnetic resonance (MAS) measurements have been performed on a Varian Direct Drive 300 MHz spectrometer with a magnetic field of 7.1 T operating at Larmor frequencies of 79.4 MHz for ^{23}Na (spin 3/2) and 78.2 MHz for ^{27}Al (spin 5/2). Samples are highly sensitive to ambient laboratory conditions, therefore in preparation for NMR study, samples have been packed into 1.6 mm zirconia rotors inside a glove box within an Argon atmosphere. In order to maintain the integrity of the samples during measurement dry N_2 gas has been used for both MAS and purge. Data have been gathered using single pulse and rotosynchronized echo pulse sequences (*pulse* - τ - *pulse* - τ – *acquire*, τ = 50 μs). High power short pulses (1 μs) were employed in order to minimize artifacts and phase distortions in the lineshapes. Spectra are referenced to 1M NaCl aqueous solution for ^{23}Na and to 1M $AlCl_3$ aqueous solution for ^{27}Al.

The ^{23}Na and ^{27}Al MAS spectra of $NaAlH_4$ as function of ball milling are given in figure 6.11. The isotropic peaks in the MAS spectra have been analyzed as superpositions of Lorentzian/Gaussian lineshape contributions.

MAS NMR measurements confirm phase identification described above. ^{23}Na spectra for the three samples show a well defined line at -11 ppm chemical shift and spinning side bands at ± 40 kHz. The effects of milling can be highlighted in the ^{27}Al spectra. ^{27}Al spectrum of pure alanate (NB0 sample) shows a single resonance at 92 ppm representing four-coordinated Al in $NaAlH_4$. Both in NB0D0 sample and in the ball milled samples (NB15 and NB15D5) this resonance is shifted upfield to 67 ppm. ^{27}Al band corresponding to $NaAlH_4$ resonance considerably decrease in intensity and appear a peak at 1640 ppm corresponding to metallic aluminum (not shown in figure 6.11), indicating a partial decomposition of the samples as effect of ball milling with carbon.

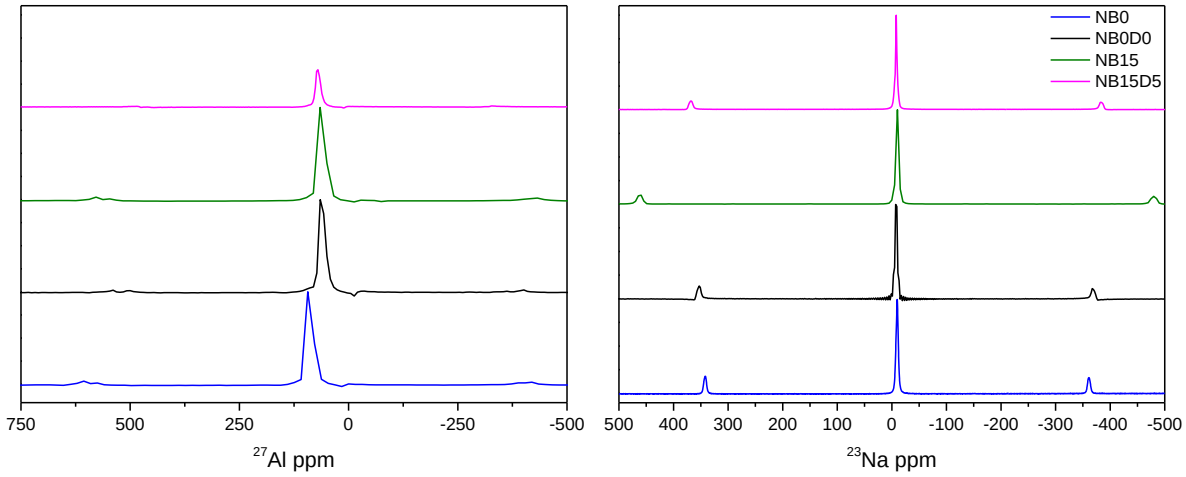

Figure 6.11 - ^{27}Al and ^{23}Na MAS NMR spectra of NB0, NB0D0, NB15 and NB15D5 samples.

Static ^{23}Na and ^{27}Al NMR has been used to investigate the local structure of $NaAlH_4$ as function of ball milling. The NMR spectra are shown in figure 6.12. ^{23}Na static lineshapes were typically broadened by 1st-order quadrupolar effects, and spectral parameters (coupling constant Q_{cc}, asymmetry parameter η, dipolar width and distributions) have been extracted via computer simulation of the experimental powder patterns. These results are summarized in Table 6.2. ^{27}Al static spectra have been analyzed according to 2nd-order quadrupolar and chemical shift anisotropy powder pattern contributions to the central transition. It is probable that some NMR signal intensity is lost due to very short T_2 (spin-spin relaxation) effects and therefore not fully represented in the spectra.

The ^{23}Na lineshape for pristine $NaAlH_4$ (NB0) shows the typical 1st-order quadrupolar powder pattern for a spin 3/2 nucleus. ^{23}Na spectrum consists of a central transition (-1/2 ↔ 1/2), two

satellites divergences (3/2 ↔ 1/2 and -1/2 ↔ -3/2) and two shoulders. For $NaAlH_4$, there is a single sodium site, where the Na^+ cation has eight nearest H neighbors at the vertices of a distorted triangular dodecahedron [67]. From another perspective, the Na^+ site is the center of an axially distorted tetrahedron where the H atoms are proximately arranged 2 per vertex. Correspondingly, the NMR shows the site to be axially symmetric (η = 0), as is evident by the divergence and shoulder features separated in frequency by $Q_{cc}/4$ [28]. The degree of structural variation is reflected in the satellite spectral features as they are extremely sensitive to the crystalline environment. Ball milling reduces the average particle size, yet as seen in the NMR satellite transitions, also creates a larger variation in bond angles about Na and Al atoms without destroying the basic crystal structure [27].

Regarding ^{27}Al powder pattern in figure 6.12, only the ±3/2 ↔ ±1/2 satellites and +1/2 ↔ -1/2 central transition are analyzed here due to poor resolution. The Al site is a tetrahedral with four H nearest neighbors (AlH_4^-); however, an EFG is present which indicates a non-spherical charge distribution. Consistent with previous measurements [68], a quadrupolar coupling constant of 3.15 MHz can be determined from the satellite positions near ± 230 kHz. The ^{27}Al central transition is convoluted by chemical shift anisotropy (CSA), 2^{nd}-order quadrupolar and dipolar effects. These contributions can be separated and analyzed via lineshape simulation. Particularly for the ball milled samples, the ^{27}Al satellite transitions are not well resolved, in comparison to the ^{23}Na case, due to distributions over a much larger Q_{cc}. As shown in figure 6.12, the dramatic effect on the central transition lineshape due to ball milling, originates mostly from distributions in the CSA, as opposed to 2^{nd}-order quadrupolar effects. This is reasonable since the EFG arises from fairly local charge distributions about the nuclear site (within 100Å), and apparently ball milling does not significantly affect the crystal structure inside this range. On the other hand, the length scale of the CSA can be relatively large (to crystallite proportions, as with the magnetic susceptibility). As seen in the ^{27}Al central transition details of samples NB15 and NB15D5, the CSA contributions to those lineshapes (e.g. the shoulders) are significantly distributed with ball milling. Attempts to perform a simple point-charge EFG computation for the Al site, in order to ascertain a lower limit length scale for ball milling effects, were not compatible with the experimental Q_{cc} value of 3.15 MHz. This is not surprising considering the degree of covalency between the Al and H atoms in the AlH_4^- tetrahedron.

In summary, NMR data show that ball milling of the alanate promotes an increase of the microstructural disorder. It seems likely that this occurs within finely produced powder and on particle surfaces as stipulated by the NMR lineshapes (large Q_{cc} and CSA distributions).

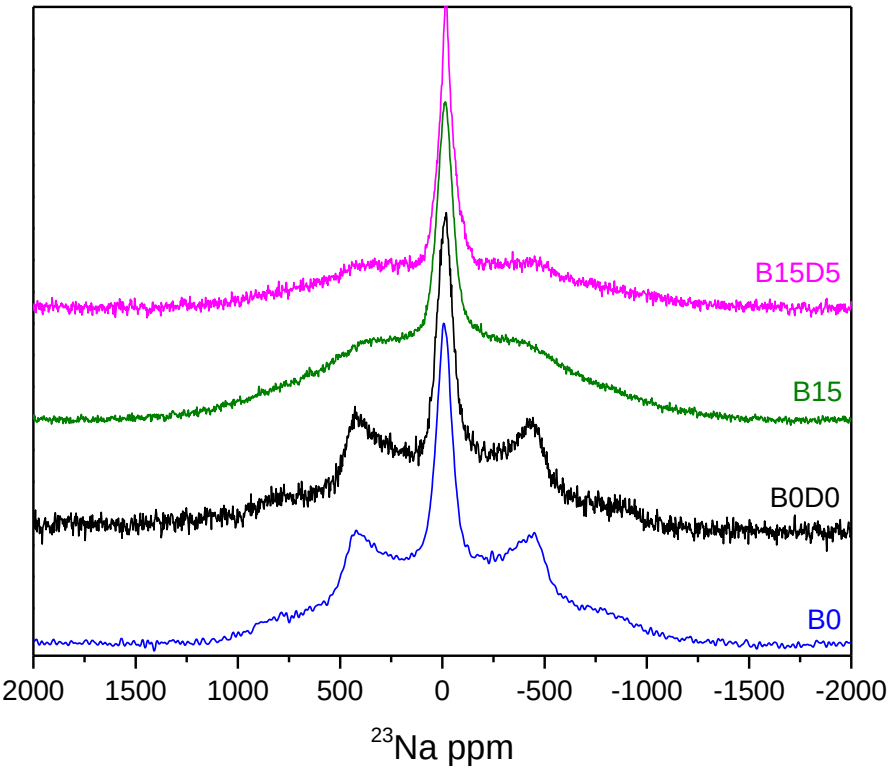

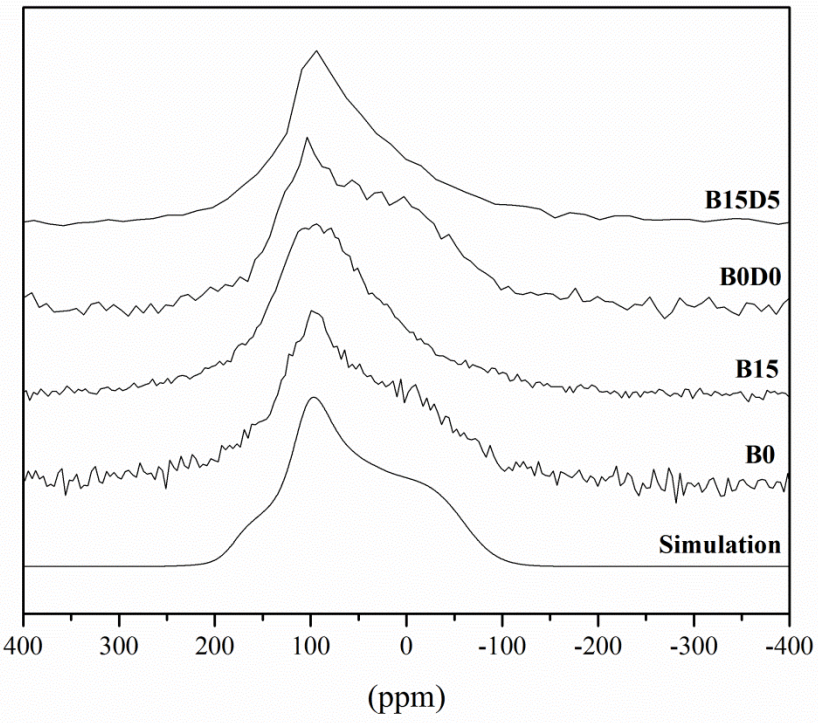

Figure 6.12 - Static ^{23}Na and ^{27}Al NMR of $NaAlH_4$ samples as function of ball milling

Table 6.2 - ^{23}Na and ^{27}Al simulation of $NaAlH_4$ samples.

	^{23}Na		^{27}Al		
Sample	**Q_{cc} [a]**	**dipolar fwhm [b]**	**Q_{cc} [a]**	**$\delta_1, \delta_2, \delta_3$ [c]**	**dipolar fwhm [b]**
NB0	0.150	8.5	3.15	200, 125, -40 (std. dev. ≈ 20)	2.2
NB0D0	0.150	8.0	3.15	200, 125, -40 (std. dev. ≈ 20)	1.5
NB15	~ 0.150 (std. dev ≈ 60)	9.0	~ 3.15	large distribution (std. dev. ≈ 200)	----
NB15D5	~ 0.160 (std. dev ≈ 60)	6.0	~ 3.15	large distribution (std. dev. ≈ 200)	----

a. quadrupolar coupling constant values in MHz and distribution (Gaussian standard deviation) values in kHz; EFG asymmetry parameter is zero for both ^{23}Na and ^{27}Al; b. dipolar fwhm in kHz and c. CSA principal components in ppm.

6.5-2 Evaluation of hydrogen content: TPD measurements

Temperature Programmed Desorption (TPD) experiments have been accomplished in order to check how the mechanochemical treatments affect the hydrogen content and its release upon heating. TPD has been carried out with a MicromeriticsAutoChem II equipped with a thermal conductivity detector (TCD). Approximately 7 mg of sample has been placed directly in the glass vial. The hydrogen desorption has been performed heating the sample up to 450 °C, using a rate of 5 °C/min, under an argon flow of 50 ml/min.

The hydrogen desorption profiles of samples under study are given in figure 6.13. According to literature [69] $NaAlH_4$ is expected to desorb through a 3-step mechanism, consisting of:

$$3NaAlH_4 \rightleftarrows Na_3AlH_6 + 2Al + 3H_2\uparrow \qquad 3.7\ H_2\ wt.\%\ ; \qquad (2)$$

$$Na_3AlH_6 \rightleftarrows 3NaH + Al + 3/2H_2\uparrow \qquad 1.85\ H_2\ wt.\%\ ; \qquad (3)$$

$$NaH \rightleftarrows Na + 1/2H_2\uparrow \qquad 1.85\ H_2\ wt.\%\ ; \qquad (4)$$

It is to be noted that this hydrogen release mechanism may be altered by kinetic limitations [45,70,71]. Results suggest that all the samples undergo to a multistage hydrogen desorption

mechanism. In fact the thermal profile is characterized by three main steps occurring in well separated temperature ranges: moreover these thermal steps are possibly constituted by the convolution of further sub-processes. For pristine sample (NB0), H_2 release starts at 182 °C, around its melting point. The amount of hydrogen released is only 0.3 wt.% H_2 with respect to $NaAlH_4$ mass. The major process, consisting of two convolute peaks, has a maximum at 293 °C. 72 % of the total H_2 content is desorbed during this step, corresponding to 5 wt.% H_2. The overall amount of hydrogen released up to 400 °C is 7 wt.% H_2 with respect to $NaAlH_4$ mass. 15 hours of ball milling (NB15) doesn't have a big impact on TPD profile. Desorption profile appears quite similar. First process exhibits a maximum at 187 °C. The amount of hydrogen released slightly rises, up to 0.5 wt.% H_2. In the range of Na_3AlH_6 desorption temperature a narrow peak appears at 304 °C with a shoulder at 291 °C, which is related to almost 5 wt.% H_2. At the end of temperature scan, NB15 sample H_2 desorption can be estimated as 7.1 wt. % with respect to $NaAlH_4$.

It is well known how carbon addition has catalytic effects on H_2 thermal desorption [72-74]. Experimental data on samples under investigation confirm significant kinetics improvements, since the whole desorption process is shifted to lower temperatures. Furthermore the relative percentage of H_2 desorbed during the low temperature step increases. Respect to the pristine NB0 sample, in the case of NB0D0 the percentage of hydrogen evolved during the first step is 0.67 wt.% H_2, corresponding to an increase from 4.3 to 9.2 % of the total amount. The hydrogen released at the end of the scan reaches the 7.1 wt.% H_2 with respect to $NaAlH_4$. Particularly interesting is the dehydrogenation behavior of the NB15D5 composite. The TPD profile is characterized by at least five processes. Below 200 °C, more than 25 % of the total hydrogen is already desorbed. Furthermore, NaH starts to decompose below 300 °C. NB15D5 releases a total amount of hydrogen corresponding at 6.9 wt.%. Compared with other sample, NB15D5 desorbs a lower amount of hydrogen because ball milling causes a partial decomposition of the sample to Na_3AlH_6 and Al, in line with diffraction and IR measurements [26]. This means that approximately 5% of $NaAlH_4$ sample is decomposed. Nevertheless desorption processes are largely accelerated.

Table 6.3 reports a summary of the analysis above described.

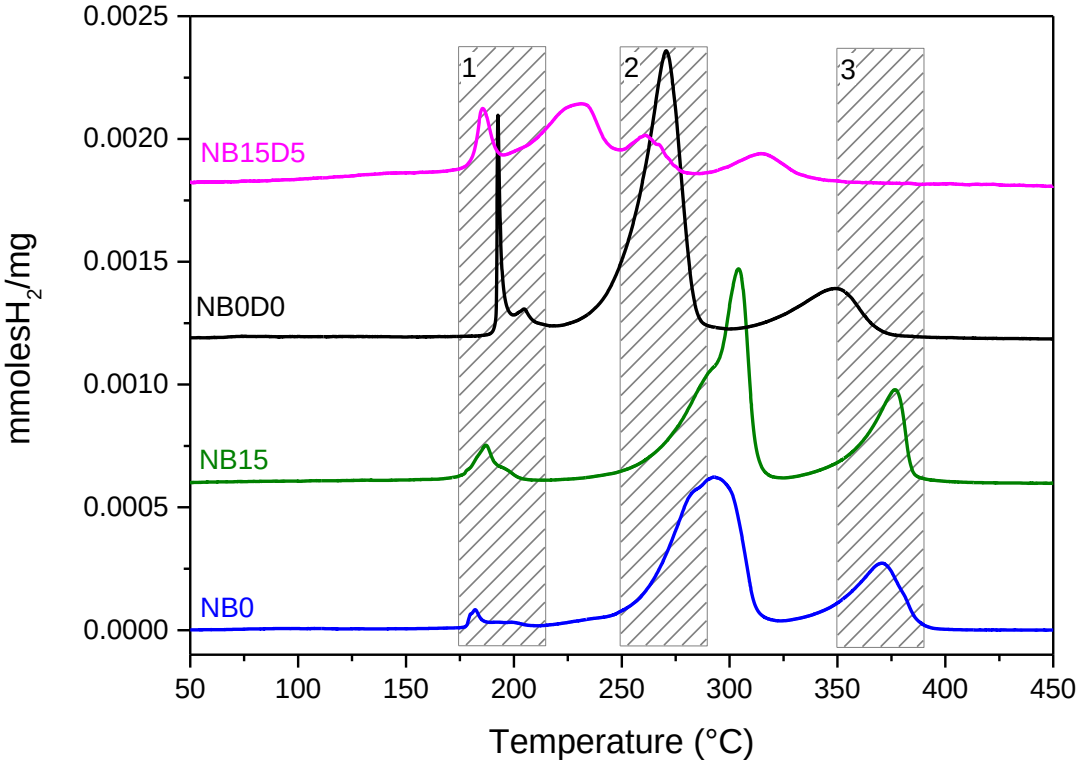

Figure 6.13 - Thermal Programmed Dehydrogenation of $NaAlH_4$ samples.

Table 6.3 - Hydrogen content calculated as H_2 weight % with respect to $NaAlH_4$ and relative temperature corresponding to the maximum of the relative hydrogen desorption intensity.

Sample	**NB0**		**NB15**		**NB0D0**		**NB15D5**	
	H_2 wt.%	**Temp. (°C)**	**H_2 wt.%**	**Temp. (°C)**	**H_2 wt.%**	**Temp. (°C)**	**H_2 wt.%**	**Temp. (°C)**
I step	0.3	182	0.53	187	0.43	193	0.75	144
					0.24	205	1	186
II Step	5	293	4.68	304	5.22	271	2.92	230
							1.1	261
III step	1.7	370	1.8	377	1.38	349	1.14	315
Total.	**7**		**7.1**		**7.27**		**6.9**	

Carbon catalytic effect arises from the electronegativity of its surface. Berseth et al. [73] demonstrated that the stability of $NaAlH_4$ originates with the charge transfer from Na to the AlH_4 moiety, resulting in an ionic bond between Na^+ and $[AlH_4]^-$ and a covalent bond between Al and H. As $NaAlH_4$ interacts with a substrate that is as electronegative as AlH_4, the ability of Na to donate the electron to form the $[AlH_4]^-$ anion is compromised and hence the covalent bond between Al and H is weakened. This weakening of the metal-hydrogen bond leads to lowering of the hydrogen desorption energy and hence to facilitate the absorption of H_2 to reverse the dehydrogenation reaction. Both NB0D0 and NB15D5 show a significant kinetics improvements respect their homologues without carbon, but it is clear that the catalytic effect is more marked for sample NB15D5, where 5 hours milling created the condition for a much more effective surface interaction between alanate and carbon.

6.5-3 Electrode kinetics in lithium cells

EIS measurements have been carried out on cells at different states of discharge: OCV, 0.2 V and 0.01 V vs. Li (i.e. at potentials intermediate to those of the observed relevant electrochemical processes as in figure 6.6). Accordingly, cells were discharged to the desired potential by small potentiostatic steps with galvanostatic acceleration (i.e. the same procedure adopted for PCGA measurement), and therefore the impedance spectra have been collected under "quasi-equilibrium" conditions. The obtained Nyquist plots are reported in Figure 6.14.

The samples under investigation appear to be different at the open circuit. Cells assembled with the NB15D5 samples behave as already described in chapter 6.4, exhibiting an OCV close to 1 V and a non blocking impedance (a huge semicircle, which closes to the real axis at low frequencies). NB0D0 material has the typical OCV ranging between 2.0-2.5 V and behaves like a blocking electrode, with a high frequency semicircle due to a native solid electrolyte interface, but already at medium frequencies the impedance is dominated by surface charge accumulation (capacitive straight line). While the mechanically treated alanate is very reactive and quickly attacks the carbonyl functional group of the alkyl carbonate electrolyte solvents, promoting their partial reduction without closing the cell circuit, the pristine material is probably protected by a native oxidized surface layer.

As the cells are discharged, their differences are somehow compensated. When the electrode potential is moved to 0.2 or 0.01 V (figure 6.14b and c, respectively), both NB0D0 and NB15D5 exhibit relatively small impedance, characterized by the sequence of the SEI and the charge transfer

semicircles, followed by a straight capacitive contribute at low frequencies, possibly due to a diffusion kinetic limitation. Indeed modeling charge transfer and diffusion in this system is rather complicated, since the conversion reactions imply, in addition to the electrolyte, the coexistence of at least 4 solid phases with the possible mobility of two small ions, i.e. Li^+ and H^-. The molecular path of the conversion reaction is well beyond the purpose of this study, and no attempt is made for an in-depth rationalization of the various kinetic steps. Nevertheless it is possible to qualitatively evaluate the evolution. The high frequency SEI semicircle slightly increases upon discharge, while the charge transfer contribution decreases. Circuital parameters obtained by spectral simulation do not differ significantly and are in the range of 18-30 Ω for R_{SEI} and 5-35 Ω for R_{ct}.

Therefore ball milling activates the alanate, but does not seem to significantly affect the kinetics of the conversion reaction.

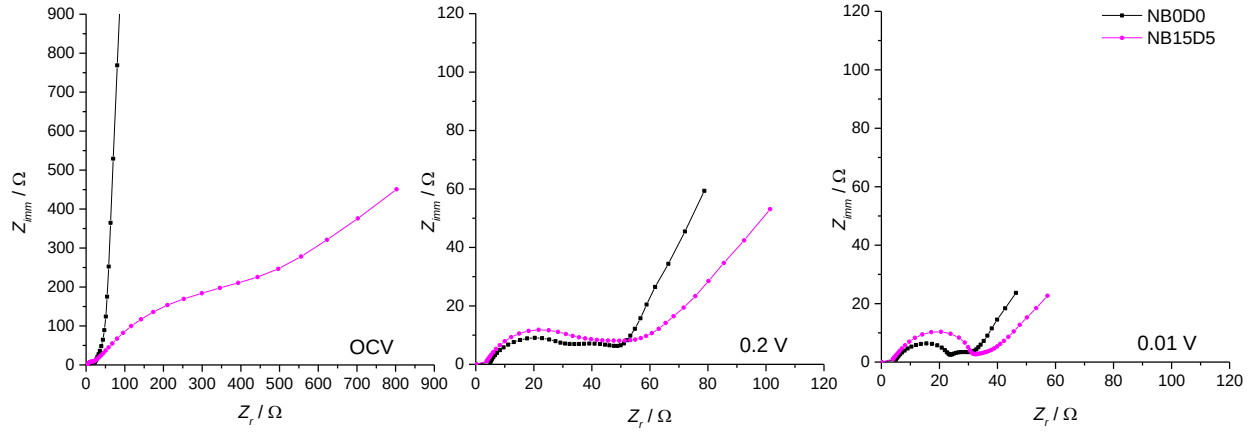

Figure 6.14 - EIS Nyquist plot recorded at a) OCV, b) 0.2 V and c) 0.01 V of NB0D0 (black) and NB15D5 (magenta) samples. Frequencies range from 10 kHz - 0.01 Hz.

6.6 Electrode cyclability

Finally, cycle life stability of sodium alanate based electrodes has been studied under galvanostatic condition. Galvanostatic charge/discharge behavior was tested using a Maccor battery test system. Cells were fabricated by sandwiching Whatman separators embedded in LP30 electrolyte with Li metal and $NaAlH_4$ as counter and working electrode, respectively. The cells were cycled galvanostatically at C/20, corresponding to a current density of 100 mA/g.

Figure 6.15a shows the voltage profile obtained for NB0D0 sample. At the end of first discharge, achieved capacity overcomes the theoretical one, reaching approximately 2200 $mAhg^{-1}$. As expected, discharge proceeds through a multistep process, including two little plateaus at 0.3 and 0.25 V, followed by a sloping plateau around 0.1 V. Processes are therefore affected by even higher overpotentials then those observed in PCGA. Furthermore, at 0.8 V it's observable the electrolyte decomposition. As occurring in PCGA measurements, charge develops only the 35% of the exchanged capacity through two slopes at 0.4 and 0.5 V, corresponding to 783 $mAhg^{-1}$.
Second discharge exhibits only a short plateau around 0.12 V, achieving less than 690 $mAhg^{-1}$, followed by a shorter charge evolving through a plateau around 0.5 V. Upon cycling, capacity continues decreasing and after 10 cycles it is below 250 $mAhg^{-1}$, as shown in figure 6.15b.

In figure 6.16, there are the results of cycling obtained for NB15D5 sample. Discharged capacity exchanged upon first cycle slightly overcomes the theoretical, reaching 2010 $mAhg^{-1}$. In line with PCGA measurements, voltage profile changed respect to pristine sample. Specifically, as already observed the process related to electrolyte decomposition around 0.8 V disappeared, while it is characterized by a plateau around 0.5 V, followed by a slope at 0.45 V and two other plateaus under 0.2 V. Also in galvanostatic mode ball milled sample shows an improved recharge efficiency, giving back approximately 1120 $mAhg^{-1}$ through two processes around 0.47 V and 0.8 V. But, in contrast with PCGA measurements, this improvement is not so large reaching only the 57%.
However, while mechanochemical treatments proved to increase charge efficiency during first cycle, they don't have impact on cycle life stability. In fact, as already observed for NB0D0 sample, capacity drastically decreases during following cycles, reaching equally 250 $mAhg^{-1}$ after 10 cycles.

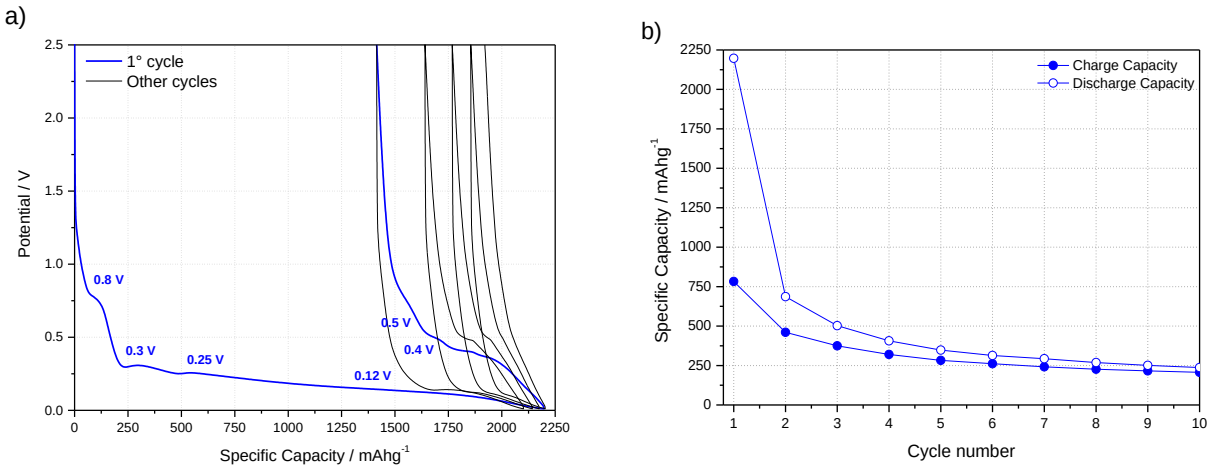

Figure 6.15 - Galvanostatic cyclation of NB0D0 sample acquired in a voltage range between 2.5 and 0.01 V at current rate corresponding to C/20: a) voltage profile and b) specific capacity versus cycle number.

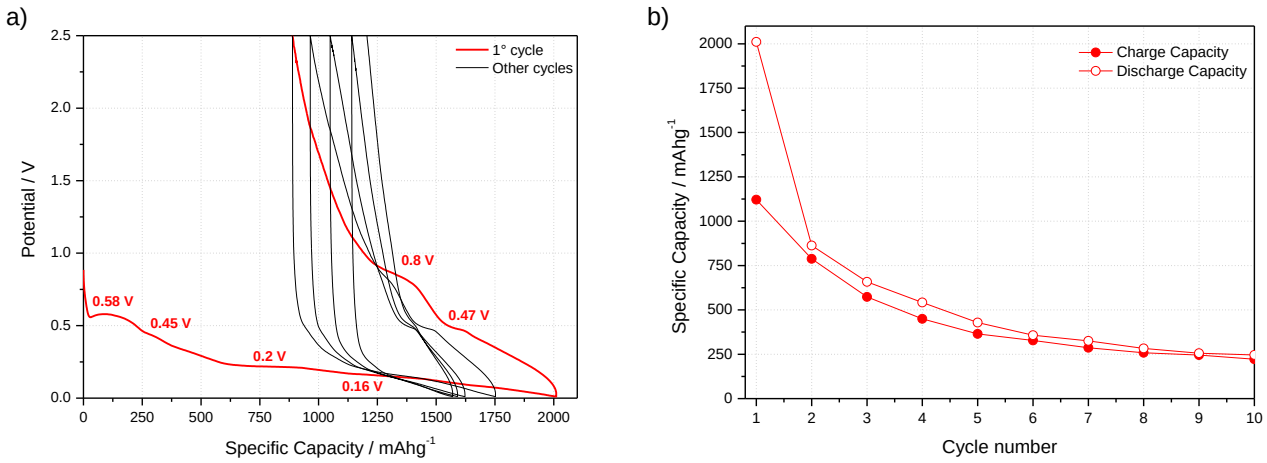

Figure 6.16 - Galvanostatic cyclation of NB15D5 sample acquired in a voltage range between 2.5 and 0.01 V at current rate corresponding to C/20: a) voltage profile and b) specific capacity versus cycle number.

6.7 Conclusions

$NaAlH_4$ has proven to be electrochemical active. Upon first discharge, through a complex process, it is able to achieve almost all the theoretical capacity (1985 $mAhg^{-1}$) corresponding to more than 3.5 Li equivalents. Unfortunately, recharge is very poor: only 30% of exchanged capacity is recovered. Inefficiency can be the effect of the theoretical concurrent sodium stripping reaction upon charge and consequent electrode's sodium depletion and of the big volumetric expansion observed upon conversion reaction. In fact, during the discharge the electrode volume increases with the lithium transfer and decreases during the lithium extraction. In the case of $NaAlH_4$, according to a full reduction, following the reaction: $NaAlH_4 + 4Li^+ + 4e^- \rightarrow 4LiH + Al + Na$, a volume modification of 72% can be expected. As a consequence, voids are created inside the electrode and disconnect the particles from each other and from the current collector at the same time.

Efficiency improvements have been obtained synthesizing an appropriate composite alanate/carbon by ball milling. In fact, NB15D5 sample is capable to give a discharge capacity value close to the theoretical one (1985$mAhg^{-1}$) with a Coulombic efficiency in the whole discharge-charge cycle of around 70%. Several methods have been used to highlight the effect of mechanochemical treatments on properties of alanate and understand how these impact on electrochemical performance. For instance, NMR provided evidences of an increase of the microstructural disorder, which turns into a kinetics advantage upon hydrogen desorption. EIS measurements highlighted the formation of a highly reactive interface between electrode and electrolyte, but any significant impedance reduction. This means that alanate is activated but, in contrast with the thermal desorption process, it doesn't result in an enhanced electrode kinetics.

In summary, ball milling seems to promote the creation of an intimately mixed carbon-hydride composite material in which carbon acting as coating agent improves the poor electronic conductivity of the active materials produced during conversion reaction, as LiH. However, mechanochemical treatments are less effective on cycle life stability and only lightly improvements have been observed in ball milled sample.

On the other hand, two main issues are still unsolved: the large volumetric changes upon conversion and high reactivity of alanate with carbonates-based electrolytes. These issues have been addressed in the last section, where two different improvement strategies will be presented.

7

Na_3AlH_6 and $LiNa_2AlH_6$

7.1 Samples preparation

Synthesis of Na_3AlH_6 and $LiNa_2AlH_6$ was attempted by High Energy Ball Milling under inert atmosphere according to the following reactions, respectively:

$$NaAlH_4 + 1.8NaH \rightleftarrows Na_3AlH_6 \qquad (1)$$

$$NaAlH_4 + NaH + LiH \rightleftarrows LiNa_2AlH_6 \qquad (2)$$

In the case of Na_3AlH_6, defective NaH starting mixtures was used because some $NaAlH_4$ tend to spontaneously convert to Na_3AlH_6 and Al due to the heat developed upon milling.
The milling was carried out using an 8000M SPEX mill for 15 hours, by the use of the procedure described in chapter 4.

Sample synthesized was added with Super P by hand grinding in mortar.

7.2 Physical-chemical characterization

As synthesized samples have been characterized in terms of structure and morphology. The obtainment of desired phase has been verified by X-ray diffraction, Infrared spectroscopy and solid state NMR. Figure 7.1 and 7.2 show the XRD pattern of Na_3AlH_6 and $LiNa_2AlH_6$ sample, respectively. The purity of the phase and lattice parameters have been determined by Maud program [51].

Na_3AlH_6 pattern has been collected in a simultaneous 120° angular dispersion X-ray diffractometer equipped with a Cu Kα1 source by using a homemade, sealed planar holder equipped with a Kapton window, in order to protect sample from air. ICSD 154909, 261353 and 240129 patterns have been used as references for Na_3AlH_6, NaH and Al respectively.

The results of pattern refinement for Na_3AlH_6 sample are resumed in table 7.1. Mechanochemical synthesis produces α-Na_3AlH_6 as major phase (95.2 wt.%). It crystallizes according to the monoclinic space group $P2_1/n$, with lattice constant a = 5.396 ± 0.002 Å, b = 5.506 ± 0.002 Å, c = 7.742 ± 0.002 Å and β = 89.8 ± 0.1. The crystallite average dimension is 38 ± nm.

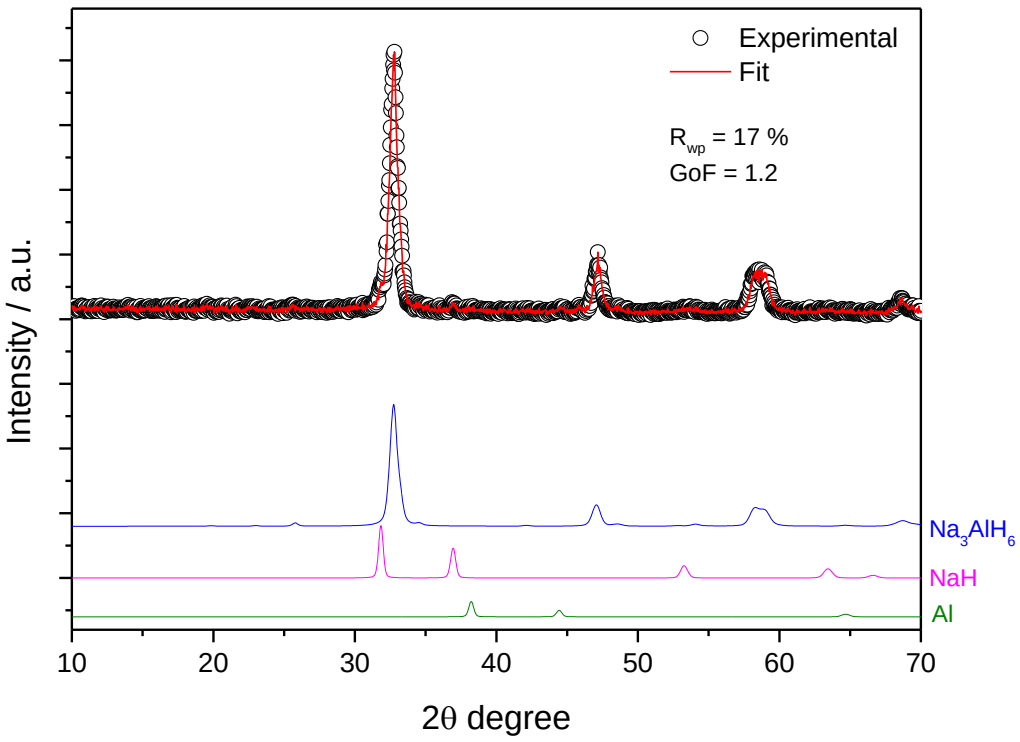

Figure 7.1 - Pattern refinement of Na_3AlH_6.

Unreacted NaH (3.8 wt.%) is still present at the end of ball milling: the (111) reflection as a shoulder at 31.8° and two little peaks at 2θ = 36.9° and 53° relative to the (200) and (220) reflections. Moreover, also three little aluminum reflections at 2θ = 38.2°, 44.3° and 64.7° can be detected in diffraction pattern to which could contribute the sample holder.

Table 7.1 - Phase composition and crystal structure of Na_3AlH_6.

Phase	Spatial group	Content (wt. %)	Lattice constants
α-Na_3AlH_6	$P2_1/n$	95.2	a = 5.396 ± 0.002 Å b = 5.506 ± 0.002 Å c = 7.742 ± 0.002 Å β = 89.8 ± 0.1
NaH	*Fm3m*	3.8	a = 4.862 ± 0.002Å
Al	*Fm3m*	1	a = 4.0753 ± 0.004 Å

$LiNa_2AlH_6$ diffraction pattern has been recorded at the MCX beamline in the ELETTRA synchrotron radiation source with an X-ray energy of 10 keV corresponding to a wavelength of 1.24 Å. Diffraction pattern has been acquired in the range of 10° < 2θ < 70°. The halo observed in the diffraction pattern is due to the glass capillary holder. ICSD 152893 pattern has been used as reference.

As illustrated in figure 7.2, the sample under investigation consists of pure $LiNa_2AlH_6$ phase. No peaks associated to initial compounds can be recognized. It crystallizes according to the monoclinic space group $P2_1/c$, with lattice constant a = 5.251 ± 0.003 Å, b = 5.265 ± 0.003 Å, c = 7.415 ± 0.003 Å and β = 89.9 ± 0.2. The crystallite average dimension is 38 ± 2 nm.

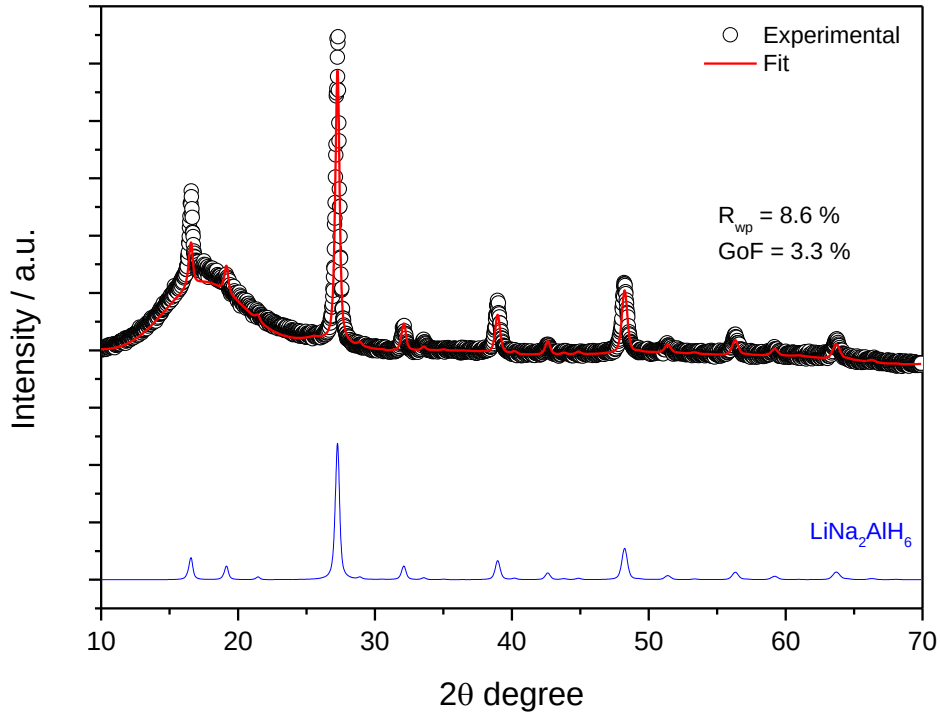

Figure 7.2 - Pattern refinement of synthesized $LiNa_2AlH_6$

In order to confirm diffraction data, solid state NMR experiments have been carried out on synthesized hexa-alanates. The ^{23}Na and ^{27}Al MAS spectra have been acquired in the same conditions described in chapter 6. Results are shown in figure 7.3.

Synthesized samples confirmed consisting mainly of pure phases. Either Na_3AlH_6 and $LiNa_2AlH_6$ exhibits a single resonance with ^{27}Al probe at -43 ppm corresponding to octahedric $[AlH_6]^{3-}$. In the ^{23}Na spectrum, $LiNa_2AlH_6$ shows a single resonance at -18 ppm and Na_3AlH_6 two resonances at 22 and -13 ppm corresponding to the two non equivalent positions in the structure of Na_3AlH_6. Also, in the case of Na_3AlH_6, direct evidence of NaH is not observable. ^{23}Na NMR signal of NaH resonates about -18 ppm, then overlapping to the broad peak at -13 ppm of Na_3AlH_6 and rendering not possible to discriminate the two different resonances.

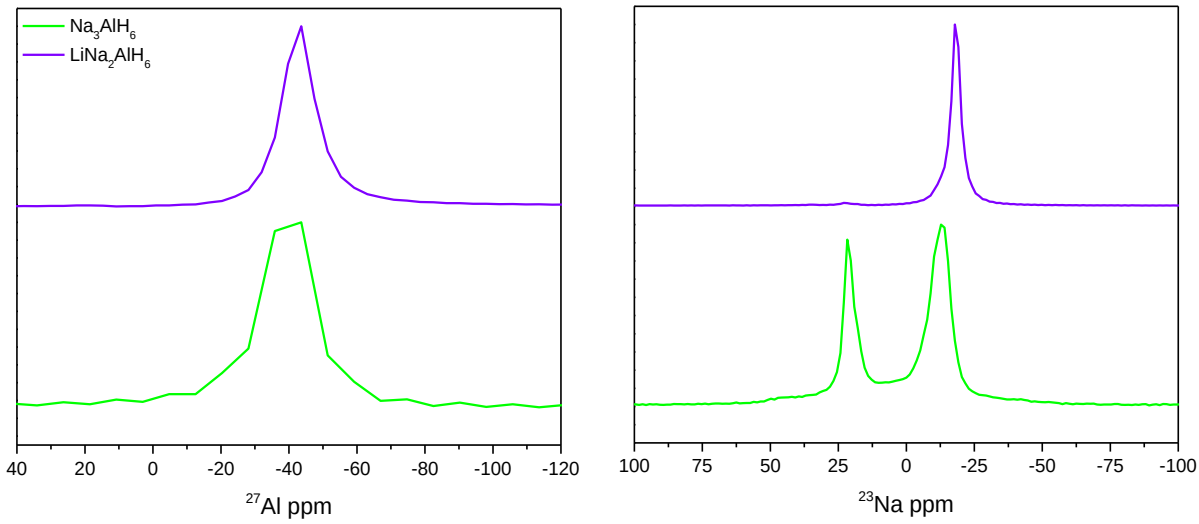

Figure 7.3 - ^{23}Na and ^{27}Al MAS NMR spectra of Na_3AlH_6 and $LiNa_2AlH_6$.

Finally FTIR spectra are given in figure 7.4. FTIR assignments have been done according to refs. [55] and [75]. Regarding Na_3AlH_6 sample, FTIR analysis confirms the formation of almost pure α-Na_3AlH_6 with minor traces of the pristine $NaAlH_4$. In fact the FTIR spectrum of the Na_3AlH_6 sample shows two bands at 1432 and 1293 cm^{-1} due to the AlH_6^{3-} stretching modes and a composite broad band centered at 840 cm^{-1} (with possible separated features at 910, 872, 837 and 796 cm^{-1}) due to the AlH_6^{3-} stretching modes, partially overlapped with smaller lines at 1772, 1682 cm^{-1} and at 725 cm^{-1} due to the vibration modes of the AlH_4^- units. Turning to the FTIR spectrum of the $LiNa_2AlH_6$ sample, it shows features similar to the Na_3AlH_6 one: two well separated composite broad bands centered at 1410 and 792 cm^{-1} likely due to the stretching and bending modes of the AlH_6^{3-} units, respectively. Also in this case possible traces of the pristine $NaAlH_4$ phase can be also highlighted thanks to the weak bands at 1767 and 1660 cm^{-1}.

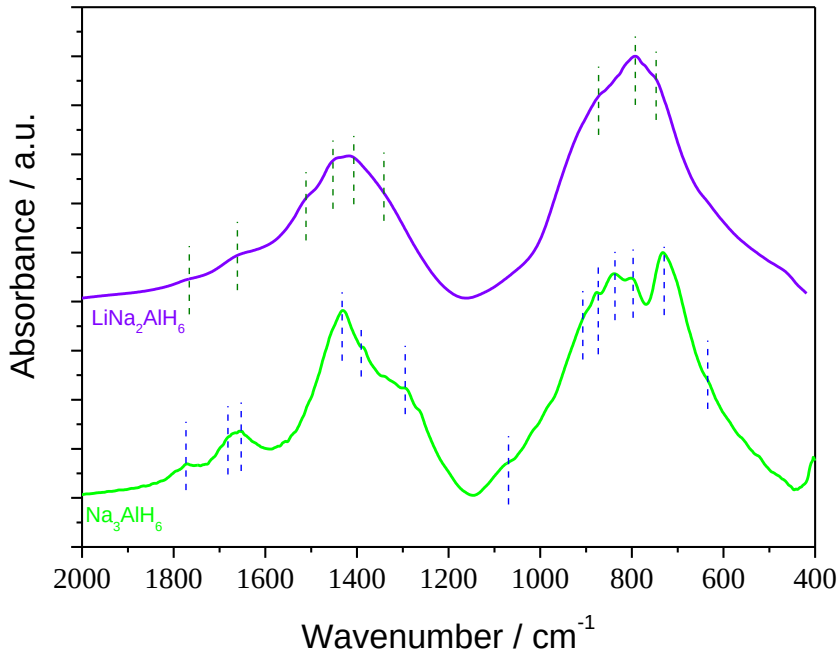

Figure 7.4 - FTIR spectra of Na_3AlH_6 (green) and $LiNa_2AlH_6$ (violet).

From the morphological point of view, the mechanochemical synthesis of the two samples results in a rather similar morphology, as shown in the TEM micrographs reported in figures 7.5. A homogeneous morphology is observed for both the α-Na_3AlH_6 and the $LiNa_2AlH_6$ samples constituted by large micrometric round-shaped particles with smooth surfaces and low phase contrast on the particle edges.

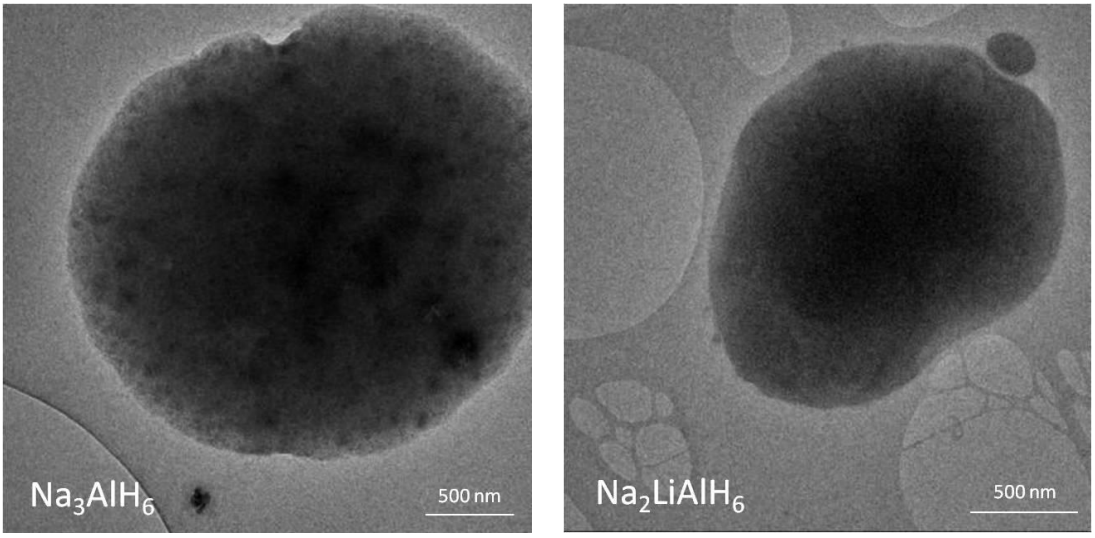

Figure 7.5 - TEM micrograph of Na_3AlH_6 and $LiNa_2AlH_6$.

7.3 Electrochemical characterization

The potential profiles of Na_3AlH_6 and $LiNa_2AlH_6$ electrodes versus the exchanged capacity are shown in the figure 7.6. The Na_3AlH_6 sample shows poor performance: less than 750 $mAhg^{-1}$ (corresponding to 2.65 lithium equivalents) over 1576 $mAhg^{-1}$ (6 Li equivalents) were exchanged upon discharge and only 202 $mAhg^{-1}$ during the following recharge. Reduction occurs upon a badly resolved plateau approximately at 0.15 V vs. Li, whereas in the following oxidation a very short process around 0.4 V vs. Li can be tentatively identified. On the contrary, the $LiNa_2AlH_6$ sample is able to achieve all the theoretical capacity, i.e. 1872 $mAhg^{-1}$ corresponding to 5 lithium equivalents, in the first reduction, through a very long plateau at 0.19 V vs. Li and a final slope to 0 V vs. Li. Upon oxidation nearly 2 lithium equivalents are returned, in two short sloping plateaus occurring at 0.38 and 0.49 V vs Li. Irreversible reduction processes occurring above 0.8 V vs. Li have been attributed to electrolyte decomposition.

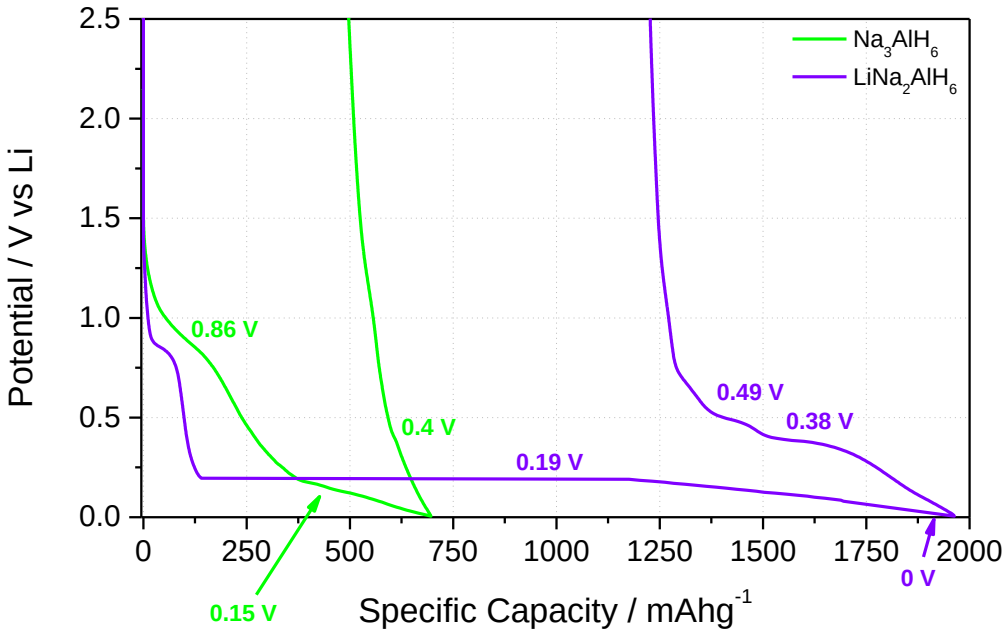

Figure 7.6 - PCGA responses obtained for the samples Na_3AlH_6 and $LiNa_2AlH_6$.

7.4 Conclusions

Na_3AlH_6 and $LiNa_2AlH_6$ have been successfully prepared by high energy ball milling. The two hexa-alanates showed completely different electrochemical performance. While $LiNa_2AlH_6$ resulted interestingly active, achieving all the theoretical capacity, Na_3AlH_6 developed less than the half of the theoretical capacity. Anyway, cell efficiency is poor for both samples, probably because no efforts for electrode optimization have been made.

8

Study of reaction mechanism in lithium cells

8.1 *Ex-situ* MAS NMR experiments

According to electrochemical tests performed in chapter 6, NB0D0 and NB15D5 samples exhibit very different voltage profiles. NB0D0 discharge develops in three plateaus around 0.41, 0.26 and 0.17 V vs. Li respectively, for an overall capacity of 1700-1800 $mAhg^{-1}$. Recharge occurs through a two steps process evolving around 0.40 and 0.47 V vs. Li, but efficiency is lower than 30%. On the other hand, for sample NB15D5, the conversion reversibility is drastically enhanced and nearly 1250 $mAhg^{-1}$ are delivered back on charge, with a Coulombic efficiency close to 70%. Upon reduction, short plateaus at 0.62, 0.37, 0.24 and finally 0.18 V vs. Li can be highlighted, while on charge, in addition to the process occurring at about 0.46 V vs. Li, there is a sloping oxidation around 0.8 V vs. Li.

In order to have first evidences of the conversion mechanism and highlight the effect of the performed mechanochemical treatment, *ex-situ* ^{23}Na and ^{27}Al MAS NMR experiments on $NaAlH_4$ samples at different stage of discharge/recharge was performed.
Specifically, NB0D0 and NB15D5 electrodes were coupled to lithium counter electrodes in pouch cells (figure 8.1). Electrochemical discharge and charge were carried out with a MACCOR cycler in galvanostatic mode at C/20 rate. Electrodes in fully discharged state (0.01 V vs. Li) and in a fully recharged state (2.5 V vs. Li) were recuperated from the lithium cells, washed with dimethyl carbonate and dried. The final powders were used to pack the NMR rotor. All manipulations were performed in an argon-filled glove box.

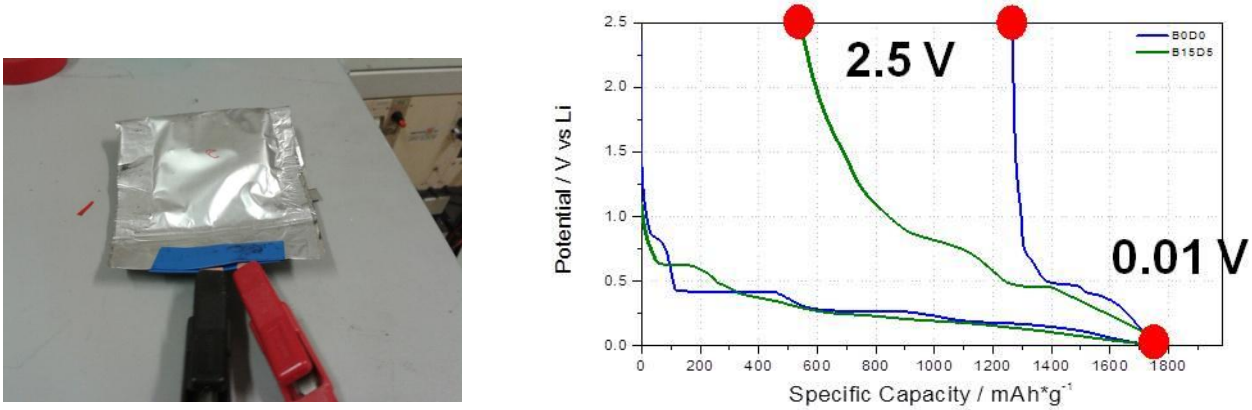

Figure 8.1 - Example of pouch cell assembled for *ex-situ* NMR measurements (on the left) and voltage profile of NB0D0 and NB15D5 samples: red circles indicate the voltage to whom electrodes have been recuperated.

NMR results obtained for NB0D0 and NB15D5 samples are given in figure 8.2.

Regarding NB0D0 discharged sample, ^{27}Al MAS spectra shows a signal at -43 ppm, which could be attributed to the overlap of Na_3AlH_6 and $LiNa_2AlH_6$ resonances. The peak at +1640 ppm is the Knight shifted metallic aluminum resonance and at +158 and +178 ppm the spectrum exhibits two intensive broadened peaks, likely due to a 4-coordinated alkyl-Al compounds [76]. In the charged sample, the resonance associated to hexa-alanates doesn't show any difference. On the contrary, resonances at +158 and +178 ppm decrease considerably in intensity while metallic aluminum signal increases in intensity. Alkyl-Al compounds probably result from the undesired reactions of metallic aluminum nanoparticles produced upon conversion and DMC used to wash the cycled electrodes. Metallic aluminum is more abundant and more highly exposed in the discharged electrode than in that recharged one, where it has partially reacted back to alanate, therefore in the discharged state it more likely interacts with the DMC producing 4-coordinated alkyl-Al compounds, while in the charged state residual aluminum more easily remains in its metallic state. Turning to ^{23}Na spectra, the discharged sample shows a little resonance near +18 ppm, which is attributed to one of the two resonances of Na_3AlH_6. Furthermore, it exhibits two convolute peaks near -13 ppm and -18 ppm with a little shoulder near -10 ppm. These might be attributed to the second resonance of Na_3AlH_6, $LiNa_2AlH_6$ and residual $NaAlH_4$ respectively. Furthermore, two Knight shifted metallic components at about +1120 ppm and +1135 ppm are present. In the spectrum of charged sample the resonance at -13 ppm increases considerably in intensity, while the peak at + 18 ppm slightly decreases in intensity. Probably, this feature derived from convolution of Na_3AlH_6 phase with $NaAlH_4$ emerging from oxidation. Also the peak at -18 ppm lightly increases in intensity. Finally, the peak of metallic sodium appears broadened and decreases in intensity, but it is still present.

NB15D5 NMR spectra show minor differences. The ^{27}Al spectrum of discharged sample shows two little and broad peaks at -43 ppm associated to hexa-alanates and at +96 ppm due to residual $NaAlH_4$. As already observed in NB0D0 sample the peak around +155 ppm could be ascribed to 4-coordinated alkyl-Al compounds. Finally, the spectrum exhibits the knight shift of metallic aluminum at +1640 ppm. Moreover, a little peak is visible at +16 ppm. This is assigned to octahedrally coordinated aluminum oxides, probably produced during the brief exposure to the air during sample transfer. When charged, the resonances of hexa-alanates almost disappear, while $NaAlH_4$ signals increase in intensity. Furthermore, as in the case of NB0D0 sample, the peak at +188 ppm disappears while metallic aluminum is more prominent. From the ^{23}Na spectra discharged sample exhibits two resonances at +18 ppm and -10 ppm in accordance with resonance of Na_3AlH_6 and $NaAlH_4$ respectively. Furthermore, contribution at -18 ppm could be attributed to $LiNa_2AlH_6$. Finally, at +1135 ppm the signature of metallic sodium can be recognized. Relatively to the charged sample, it is worth noting the complete absence of metallic sodium, while the peak of $NaAlH_4$ becomes predominant. Again, the resonances of hexahydrides phases disappear or significantly decrease in intensity.

As expected, electrochemical lithium loading in sodium alanate electrodes consists of a complex conversion mechanism, involving the formation of intermediates compounds, like hexa-alanates (Na_3AlH_6 and $LiNa_2AlH_6$), before final reduction to metallic sodium and aluminum. These measurements also confirmed the superior reversibility of NB15D5 compared to NB0D0 as already observed with electrochemical tests. In fact the low-resolution NMR spectra of the fully discharged materials suggest, for the both the NB0D0 and NB15D5 samples, an almost complete conversion of the sodium alanate to hexa-alanates, metallic sodium and aluminum. Conversely, although the fully charged materials show a reversible back-oxidation to the $NaAlH_4$ pristine phase in both samples, the efficiency of re-charge is greatly enhanced in NB15D5, as evidenced by relatively simpler NMR spectra, revealing zero alkyl-Al compounds, zero Na_3AlH_6, zero metallic Na, reduced $LiNa_2AlH_6$ and reduced metallic Al signals after charging.

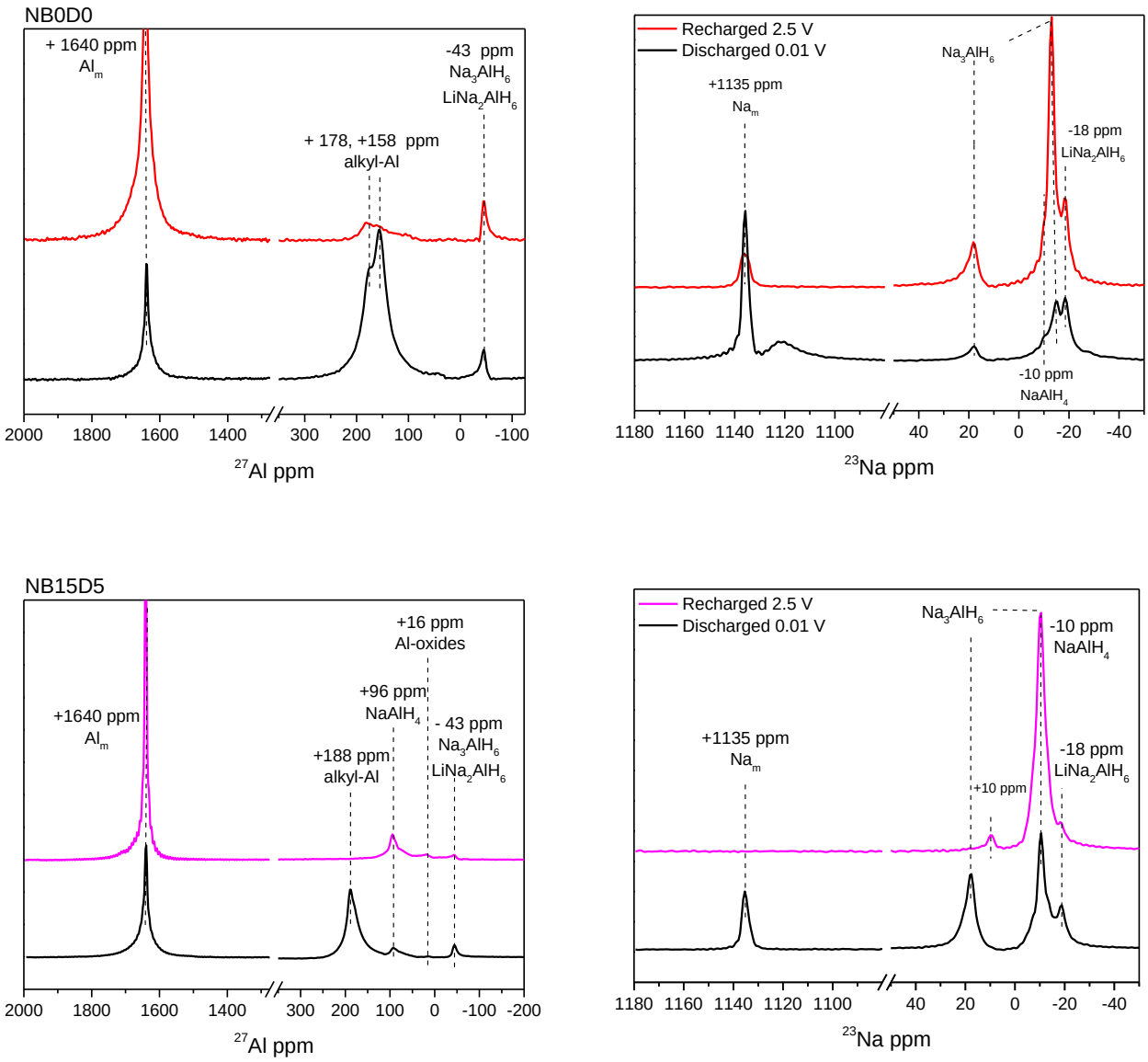

Figure 8.2 - ^{27}Al and ^{23}Na MAS NMR spectra of NB0D0 and NB15D5 samples discharged at 10 mV and recharged at 2.5 V in galvanostatic mode using a C/20 rate.

8.2 *In-situ* diffraction experiments

NMR was useful to have an insight into the conversion process of $NaAlH_4$. Experiments proved that the two samples follow the same reaction path but, as expected, they differ in the final state of charge (delivered charge capacity). However, to understand how phases evolve upon lithium incorporation/de-incorporation, in situ X-ray diffraction patterns have been acquired continuously during galvanostatic cycling measurements. A home-made electrochemical cell equipped with a top beryllium window working both as optical window and as current collector has been assembled with the electrodic mixture, Whatmann borosilicate fiber separator swollen with a standard LP30 electrolyte (1M solution of $LiPF_6$ in ethylene carbonate- dimethyl carbonate EC:DMC=1:1 mixture) and lithium metal foil as counter electrode (figure 8.3). B15D5 sample has been used for this experiment, thanks to its higher recharge capacity.

As prepared, the cell was placed in the focus of a simultaneous 120° angular dispersion X-ray diffractometer Italstructure equipped with a curved PSD detector from INEL and a Cu Kα1 source, and connected to a galvanostat, as illustrated in figure 8.3. Patterns were acquired continuously every 20 min while the electrode was discharged and charged at constant current, equal to C/20.

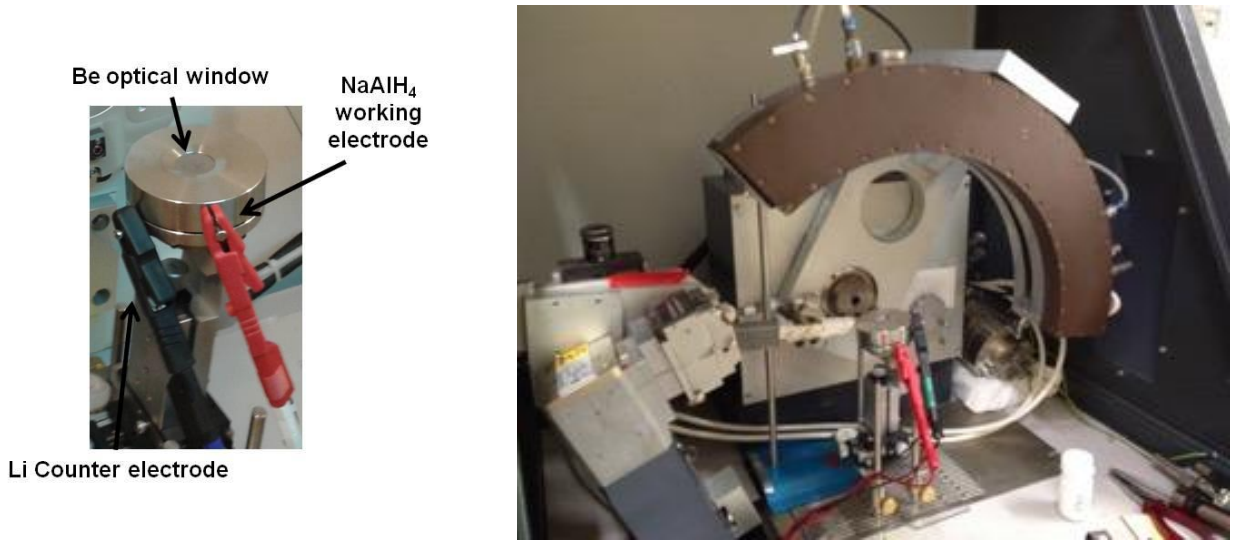

Figure 8.3 - XRD electrochemical cell (on the left) and XRD electrochemical apparatus (on the right).

Figure 8.4 reports the XRD pattern evolution of NB15D5 upon lithium incorporation in a galvanostatic discharge. The resolution of the collected patterns is rather poor for several reasons: the poor crystallinity of the ball milled powders, the low intensity of the radiation emerging from the cell associated with the low scattering factors of the lightweight elements, and the incident and

scattering beam attenuation due to the beryllium window. Nevertheless, the measurements are useful to a qualitative evaluation of the developing processes and to the identification of the involved phases.

In the open circuit condition, electrode material consists of tetragonal $NaAlH_4$ with the presence of a small amount of aluminum phase resulting from ball milling. Upon discharge, a complex reaction mechanism can be outlined involving different intermediate phases. The $NaAlH_4$ peaks monotonically decrease to 50% and 20% of the original intensity after incorporation of 1 and 2 lithium equivalents, respectively. After the incorporation of 2.75 Li eq, the $NaAlH_4$ diffraction intensity reduces to less than 10% of the original value and does not change thereafter.

At the early stage of discharge, diffraction lines assigned to aluminum continuously increase in intensity. Also, it could be note the appearance of two reflections at $2\theta = 34.2°$ and 49.4° corresponding to (220) and (400) peaks of $LiNa_2AlH_6$ respectively. After only the incorporation of 0.75 Li equivalents, very low intensity lines at 40° relative to the (220) peak of LiAl alloy can be detected. Its intensity soon stop to increase: it is possible that the alloying process involves only the pristine superficial aluminum produced during the mechanochemical treatment and not that displaced in the conversion reactions. Also, α-Na_3AlH_6 phase is observable after the incorporation of 1.5 lithium equivalent with two little peaks at 32.5° and 49.4°.

At deeper states of discharge (> 2 Li eq), $LiNa_2AlH_6$ peaks start decreasing at the advantage of the nucleation of metallic sodium. The (110) diffraction line of Na at 29.3° appears after the incorporation of approximately 2.25 Li eq, and its intensity rises monotonically up to full discharge. LiH is not observed probably for the too low scattering factors of both lithium and hydrogen. No signature of NaH can be found in the whole sequence. At the end discharge cutoff potential (i.e., 10 mV), the alanates reduction is not complete. $NaAlH_4$ has almost disappeared, while Na_3AlH_6 and $LiNa_2AlH_6$ signals are present in addition to diffraction lines of metallic aluminum and sodium.

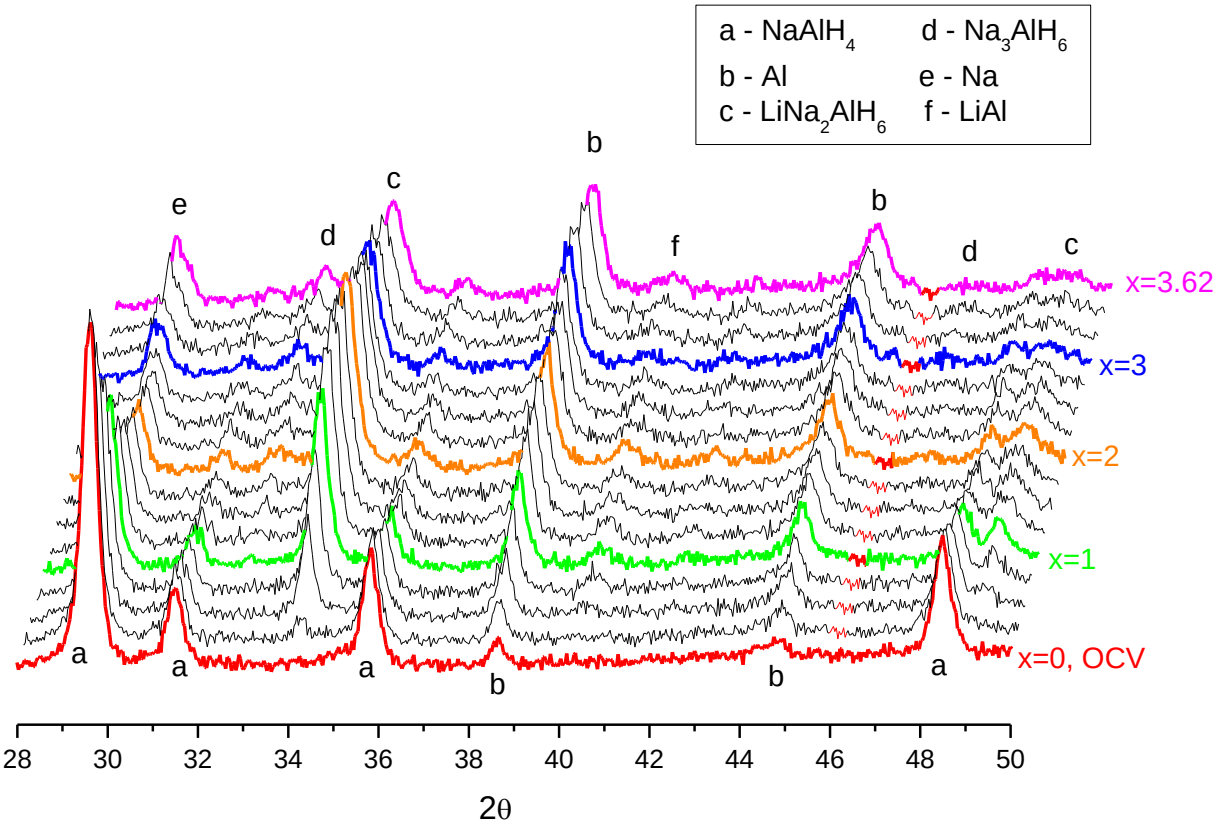

Figure 8.4 - Diffraction patterns acquired during the discharge process of NB15D5 sample.

In order to support the identification of the reactions involved in the $NaAlH_4$ discharge, also *in-situ* XRD experiments of intermediate compounds Na_3AlH_6 and $LiNa_2AlH_6$ phases have been recorded upon electrochemically driven lithium incorporation. Figure 8.5 reports a selected enlargement of the pattern sequence collected during the $LiNa_2AlH_6$ and Na_3AlH_6 discharges.

Both $LiNa_2AlH_6$ and Na_3AlH_6 discharges evolve through formation of metallic sodium. As evident from figure 8.5, diffraction patterns show the appearance of the (110) peak of sodium at 29.5°, that progressively increases until the end of discharge. Apparently, both reactions occur through an overall conversion mechanism to metals and LiH, without the formation of the intermediate NaH phase or the mutual interconversion between the two hexahydrides. Surprisingly, neither Al nor LiAl signals can be noticed. On the other hand, the ratio between Al and Na is smaller in both Na_3AlH_6 and $LiNa_2AlH_6$ compared to $NaAlH_4$ and, consequently, the amount of metallic Al produced in the various conversions is expected to be different. The complete absence of Al reflections observed in Figure 8.5 (panels a and b) also suggests that it may be produced in a poorly

crystalline or nanometric form. The conversion reactions observed by in situ XRD starting from both the sodium hexahydrides can be resumed as follow:

$$LiNa_2AlH_6 + 5Li \rightleftarrows 2Na + Al + 6LiH \qquad (1)$$

$$Na_3AlH_6 + 6Li \rightleftarrows 3Na + Al + 6LiH \qquad (2)$$

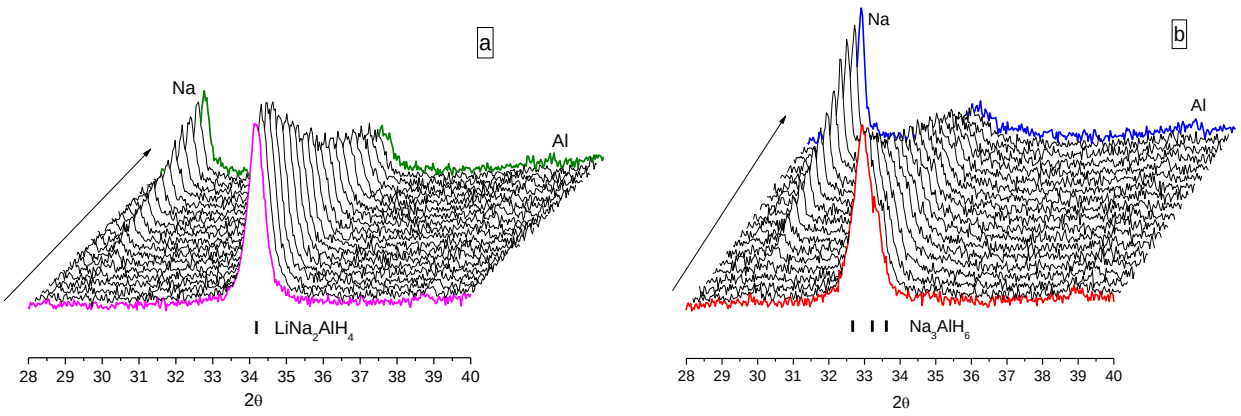

Figure 8.5 - Diffraction patterns collected during the discharge of a) $LiNa_2AlH_6$ e b) Na_3AlH_6 samples.

In summary, based on the information from the electrochemical and *in-situ* XRD measurements on $NaAlH_4$, it is possible to propose a reaction sequence occurring upon discharge. The process should involve at least three reactions:

$$2NaAlH_4 + 3e^- + 3Li \rightarrow LiNa_2AlH_6 + 2LiH + Al \qquad (3)$$

$$3NaAlH_4 + 6e^- + 6Li \rightarrow Na_3AlH_6 + 6LiH + 2Al \qquad (4)$$

$$LiNa_2AlH_6 + 5e^- + 5Li \rightarrow 2Na + Al + 6LiH \qquad (5)$$

Furthermore, the occurrence of the following two other reactions especially in the last stage of the discharge cannot be excluded:

$$NaAlH_4 + 4Li \rightarrow Na + Al + 4LiH \qquad (6)$$

$$Na_3AlH_6 + 6Li \rightarrow 3Na + Al + 6LiH \qquad (7)$$

Finally, also recharge process has been taken in account. The reactions described above are expected to reversibly occur upon charge. Moreover, sodium stripping could contribute to the observed incomplete efficiency.

The diffraction pattern collected at the end of the first charge is given in figure 8.6. NB15D5 conversion reaction is partially reversible. Metallic Al and Na as well as the Na_3AlH_6 and $LiNa_2AlH_6$ hexa-hydride peaks progressively decrease in intensity, whereas $NaAlH_4$ diffraction lines grow. At the end of the charge step, $NaAlH_4$ diffraction lines recover around 45% of their original intensity, and in parallel, the hexa-alanates phases signature disappears, while the aluminum fingerprint is still marked. Metallic Al is present in the pristine NB15D5 as an impurity produced during the intensive mechanochemical activation treatment. Nevertheless, the (111) and (200) peaks at the end of the complete discharge-charge cycle are largely more intense than in the pristine state. This indicates that part of the aluminum particles produced in the alanate conversion is apparently unable to be oxidized upon charge, giving back the $NaAlH_4$ structure. This evidence also matches well with the irreversible capacity observed in the PCGA discharge-charge test and the residual lithium equivalents kept into the electrode at the end of the first cycle (see figure 6.8).

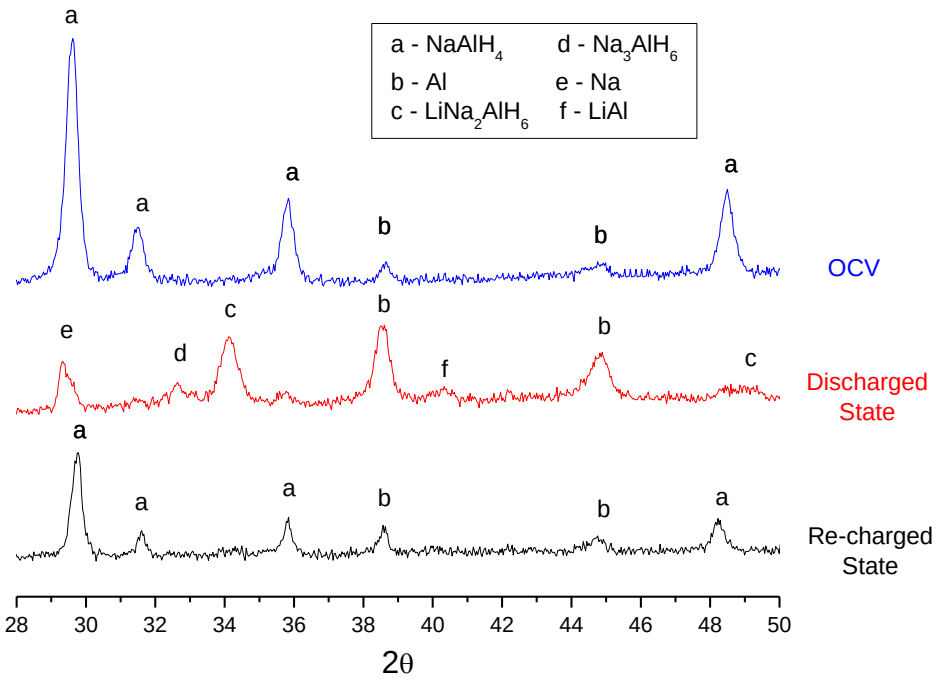

Figure 8.6 - $NaAlH_4$ diffraction patterns collected at the end of recharge (black), in the completely discharged state (red) and in open circuit condition (blue).

Finally, the experimental results can be compared with DFT calculations reported in chapter 3. The experimental reaction sequence highlighted by *in-situ* XRD differs from what expected by thermodynamic calculations. In fact, the reaction sequence derived from thermodynamics involve the formation of $LiNa_2AlH_6$ at first and then its further conversion in Na_3AlH_6 and NaH, before the

complete reduction to a mixture of metallic aluminium and sodium with lithium hydride, according to:

$$2NaAlH_4 + 3Li \rightleftarrows LiNa_2AlH_6 + 2LiH + Al; \quad 0.73\ V \quad (3)$$

$$3/2LiNa_2AlH_6 + 3/2Li \rightleftarrows 3LiH + 1/2Al + Na_3AlH_6; \quad 0.66\ V \quad (8)$$

$$Na_3AlH_6 + Li \rightleftarrows 3NaH + Al + 3LiH; \quad 0.41\ V \quad (9)$$

$$NaH + Li \rightleftarrows Na + LiH; \quad 0.43\ V \quad (10)$$

Experimentally, reaction (3) has been observed, but at lower potential (0.64 V). Besides this, also the reaction (4) occurs, although thermodynamically unfavorable; it is likely activated by a competitive surface reactivity with comparable thermodynamics overpotentials. Once converted to the $LiNa_2AlH_6$ phase, the conversion process occurs directly nucleating metallic Na according to reaction (5), whereas the thermodynamics predicts the formation of NaH as intermediate phase (9).
The mismatch between the expected and the actual reaction path must derive from kinetics issues. In fact, upon PCGA (chapters 6 and 7) were measured electrochemical equilibrium potentials for conversion reactions markedly small in comparison with any thermodynamic predictions. The occurrence of thermodynamic overpotentials have been observed and discussed for different classes of conversion materials (e.g., phosphides, oxides, and hydrides), in order to rationalize the large voltage hysteresis typically observed between electrochemical lithium incorporation and deincorporation. These overpotentials largely vary, there estimates being in the range of 150-400 V depending on ionicity of the chemical bond in the conversion material. Thermodynamic overpotentials originate by the different possible interface and surface micromechanism [13,15], and may play a crucial role in determining the reaction sequence. Indeed, these overpotentials can be large enough to reverse the expected reaction path. As a matter of fact, the occurrence of overpotentials as high as 200-300 mV upon hexahydrides reduction causes the direct nucleation of metallic sodium besides the formation of other intermediates, especially NaH.
It is worth noting that analogous overpotentials allow the conversion to be reversible. In fact, upon charge, the most thermodynamic favored process would be sodium stripping and not sodium re-inclusion into the hydride complex structure. Although stripping cannot be excluded, experimental evidences demonstrate the alanate recovery, even if not complete, while solid state NMR shows metallic sodium presence at the end of inefficient charge processes.

8.3 Conclusions

In summary, conversion reaction of sodium alanates has been experimentally demonstrated. First evidences of the process mechanism have been achieved by *ex-situ* NMR experiments. These measurements also confirmed the superior reversibility of NB15D5 compared to NB0D0 as already observed with electrochemical tests. Better evidences of the phases evolution have been obtained by *in-situ* XRD measurements during discharge/recharge of $NaAlH_4$ electrode. XRD showed how lithium incorporation into $NaAlH_4$ proceed through a multiple step process, involving the initial formation of hexa-alanates as intermediate phase and then their direct decomposition in Na and Al. Furthermore, reactions appear reversible, as evident from the restoration of $NaAlH_4$ at the end of recharge.

STRATEGIES FOR PERFORMANCE IMPROVEMENTS OF ALANATES BASED ELECTRODE

9

Synthesis and characterization of $NaAlH_4$ nanoparticles incorporated in a mesoporous carbon host

An important obstacle in the way toward application of this type of electrodes is certainly cycle life. The conversion processes entail massive structural reorganization and volumetric changes (for instance, 72% for $NaAlH_4$). These changes can lead to particle isolation and cracking as a result of electrode grinding, and to a subsequent fading of the capacity after a few cycles. Attempts to address this issue through the electrode engineering have been made for conversion reaction materials, using a number of strategies such as forming nanocomposites with nanoporous carbon [11]. Confinement strategies are commonly used in the design of hydrogen storage material, like metal hydrides [77]. Besides preserving conductivity, the presence of carbon is beneficial towards preventing grain growth and sintering by limiting the large volumetric changes encountered during lithium incorporation/de-incorporation [78,79]. Along these lines, in order to improve the performance of alanates in electrochemical cells, a nanocomposite confining alanate particles in a mesoporous carbon host matrix has been developed. A solvent-assisted infiltration method was chosen to highly disperse the hydride as well as facilitate a close contact with the carbon material [80]. The success of the infiltration method can be gauged by morphological and thermal analysis. The interaction between the carbon matrix and the sodium alanate was studied by XRD and infrared spectroscopy. Finally, electrochemical characterization is carried out by galvanostatic measurement. This study has been focused on nanoconfinement of sodium alanate in view of its encouraging results and greater manipulability in respect to lithium alanate.

9.1 Sample preparation

9.1-1 Synthesis and optimization of Carbon host

Carbon aerogels are a special class of hard carbons with a low degree of order prepared via pyrolysis of organic aerogel precursors at elevated temperature under inert atmosphere. Depending on synthesis conditions, surface area, porous volume, meso/microporosity ratio can change significantly. This leads to a remarkable potential for designing and tailoring these materials to fit specific structural features [81].

Numerous articles have appeared in the literature describing either the various synthesis and processing conditions that can be used to prepare a carbon aerogel and how these conditions affect its final structure, but results considerably diverge [82-84].

In order to prepare a suitable carbon matrix to host hydride nanoparticles (10-40 nm diameter opened pores), a rationalization of its synthetic conditions has been carried out. Specifically, the effects on surface area and porous volume of different molar ratio between resorcinol and formaldehyde (R/F), resorcinol and catalyst (R/C), resorcinol and water (R/W) and the effect of variation of temperature and duration of gelation step were taken into account.

Carbon aerogels have been synthesized by polycondensation of resorcinol with formaldehyde according to method developed by Pekala et al. [85] followed by exchange solvent and pyrolysis. In consideration of their precursors, hereafter carbon aerogels will be labeled as CRF, “Carbons from Resorcinol and Formaldehyde”.

Preparation is a multistep process which include: (1) sol-gel polymerization, (2) aging, (3) solvent exchange and (4) pyrolysis.

(1) Sol-gel polymerization: resorcinol (1,3-dihydrobenzene, $C_6H_4(OH)_2$) was dissolved in distilled water with sodium carbonate (Na_2CO_3) as basic catalyst. Formaldehyde (CH_2O) was added and the resulting solution was stirred at room temperature until homogeneous mixture was obtained. Varying the concentration ratios of different reactants has a severe effect on the resulting properties of the gel.

Resorcinol is a phenolic tri-functional monomer, reactive in the 2-, 4- and/or 6- ring positions. Resorcinol reacts with formaldehyde under alkalyne conditions to form a mixture of addition and condensation products (Figure 9.1). These intermediates further react to form a cross-linked polymer network. Reactions include (a) the formation of hydroxymtehyl (-CH_2OH) derivates of resorcinol and (b) the condensation of the hydroxymethyl derivatives to form methyl (-CH_2-) and methylene ether (-CH_2OCH_2-) bridged compounds.

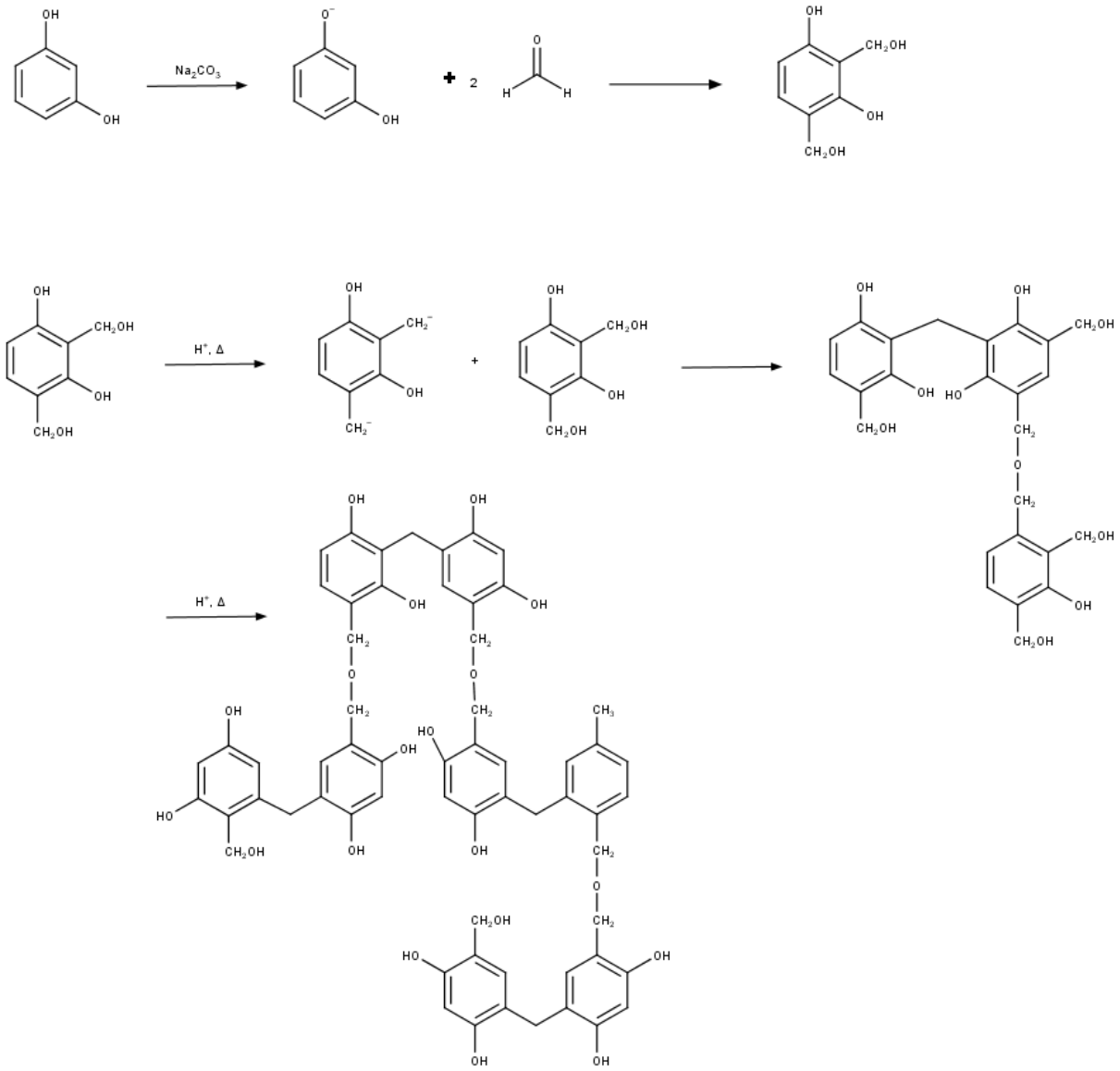

Figure 9.1 - Schematic representation of the reactions occurring during gelation step.

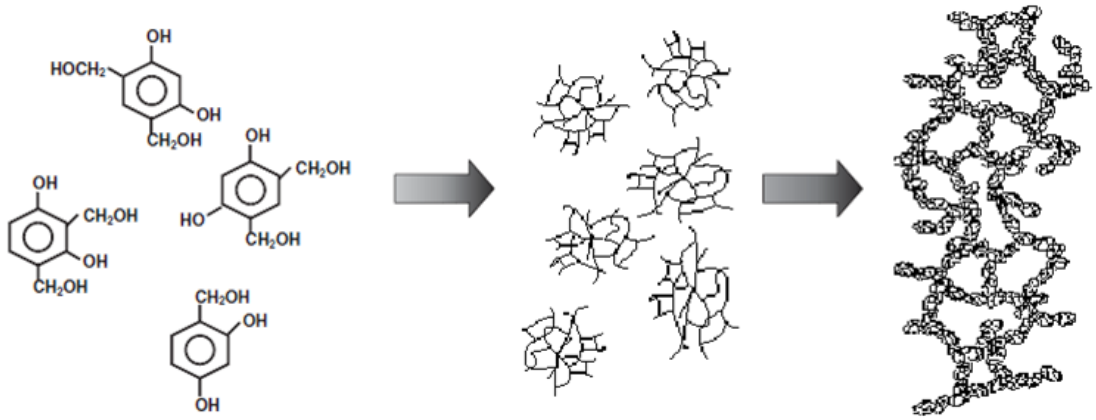

Figure 9.2 - Schematic representation of polymerization process [81].

(2) Aging: the mixture was heated in a closed container at temperature between 50-150 °C for a prolonged period. This step allows the formation of the clusters and promotes crosslinking, to finally form a solid glassy gel (Figure 9.2).

(3) Solvent exchange: water was replaced with an organic solvent (acetone) through a reiterate washing procedure.

(4) Pyrolysis: dried aerogel sample was heated in a tube furnace under argon atmosphere at 750 °C for 4 hours (heating rate of 3 °C/min).

9.1-2 Analysis of porous structure

The influence of synthesis conditions on the porous structure of obtained carbon samples has been investigated by N_2 adsorption at 77 K technique. Isotherm curves have been acquired in a Quantachrome Autosorb IQ Instrument and further analyzed using Brunauer-Emmett-Teller (BET) [86] equation to calculate surface area, t-plot [87] for microporosity analysis and Barrett-Joyner-Halenda (BJH) [88] method for mesoporosity analysis, as implemented in Quantachrome ASiQWin software. Before each measurement, the samples have been evacuated 3 hours at 300 °C.

Gelation – Gelation step is the initial polycondensation between resorcinol and formaldehyde. The main parameter affecting this process is temperature. Therefore fixed the gelation time to 1 hour, batches at different polycondensation temperature have been produced. R/C, R/F and R/W molar ratio has been kept fixed to 500, 0.5 and 0.25 respectively.

Figure 9.3 shows N_2 adsorption-desorption isotherms at 77K for carbon aerogels prepared at increasing gelation temperature.

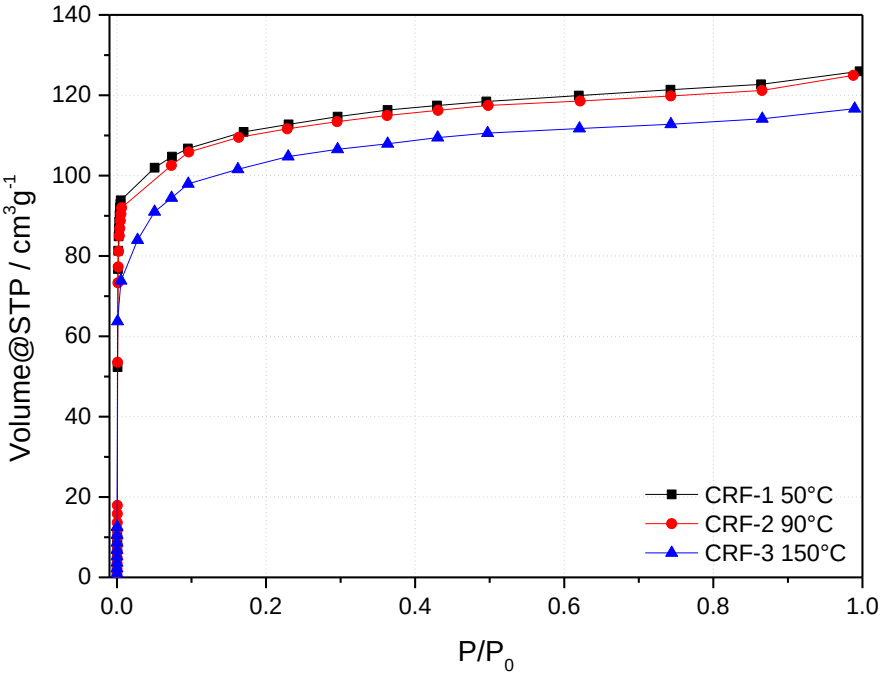

Figure 9.3 - N_2 adsorption isotherm of carbon aerogel obtained with 1 hour of gelation.

All isotherms are type I, according to IUPAC classification. This shape of the curves indicates microporous materials. They rise almost vertically at low relative pressure (adsorption take place by micropore filling), followed by an inflection point which represents the completion of the monomolecular layer. At higher relative pressure the isotherms exhibit a nearly horizontal section: once the micropores have been filled, very little adsorption takes place. Table 9.1 resumes the results obtained applying theoretical models to physisorption isotherms.

Table 9.1 - Porous characteristic of carbon aerogel obtained at different temperature of gelation.

	Temperature of Gelation	**S_{BET} (m^2/g)**	**V_{tot} (cm^3/g)**	**V_{meso} (cm^3/g)**	**V_{micro} (cm^3/g)**
CRF-1	50 °C	288	0.17	0.02	0.17
CRF-2	90 °C	394	0.19	0.03	0.16
CRF-3	150 °C	342	0.18	0.03	0.15

As evident from isotherm representation in figure 9.3, the samples don't differ significantly among each other. In all cases, micro/mesoporous volume ratio is high and total porous volume is almost identical (< 0.2 cm^3/g). However, CRF-2 sample subjected to a thermal treatments at 90 °C shows the higher surface area, equal to 394 m^2/g.

Aging - Besides the gelation step, the effects of aging process on the porosity of the carbon aerogel have been taken into account. Specifically, both temperature and time of aging have been evaluated.

At first, samples after 1 hour of gelation at 50 °C have been subjected to a gradual increase in temperature. Figure 9.4 and table 9.2 shows the results obtained after these treatments.

Increasing the temperature of aging at 90 °C, adsorption isotherms shape turns from type I (microporosity) to type IV, typical of mesoporous materials (CRF-6).

All the isotherms in figure 9.4, have the same behavior at low relative pressure. After the inflection point, the CRF-6 isotherm doesn't reach a plateau. Though a smaller slope, adsorbed volume continues to rise in the intermediate zone. Adsorption occurs in a multilayer way. Finally, when it reaches high relative pressure, the slope increases again: gas adsorbed into the pores is condensing.

The major feature of type IV isotherm is the presence of a hysteresis loop: the lower branch represents the progressive addition of adsorbent gas, while the upper branch the progressive withdrawal. The hysteresis loop is associated with the mesopores filling and emptying by capillary condensation.

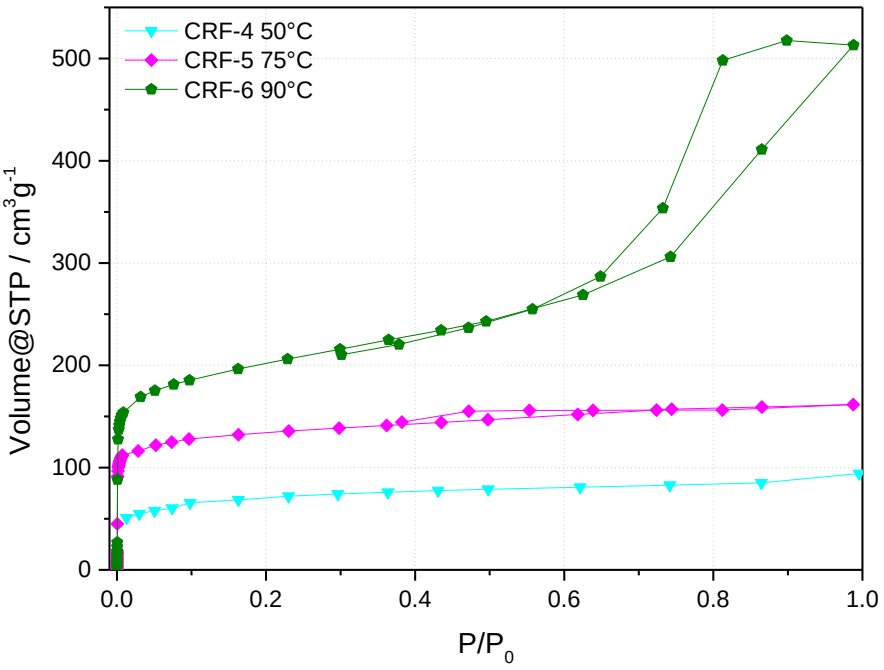

Figure 9.4 - Effect of the temperature of aging on adsorption isotherms.

The related porous parameters are listed in table 9.2. The aging at 50 °C does not improve the carbon porosity, while the aging step at higher temperature implies a consistent rise of surface area and total porous volume. Specifically, mesoporosity becomes significant: CRF-6 shows high meso/microporous volume ratio.

Table 9.2 - Influence of temperature of aging on porosity .

	Aging Time	**Aging Temperature**	**S_{BET} (m^2/g)**	**V_{tot} (cm^3/g)**	**V_{meso} (cm^3/g)**	**V_{micro} (cm^3/g)**
CRF-4	24h	50 °C	225	0.19	0.04	0.17
CRF-5	24h	75 °C	420	0.25	0.06	0.19
CRF-6	24h	90 °C	680	0.73	0.55	0.18

Subsequently, aging treatments at 90 °C has been prolonged up to 96 hours. Adsorption/desorption N_2 isotherms at 77K are shown in figure 9.5. Except for CRF-2 (1h aging) exhibiting type I curve, samples subjected to prolonged time of aging have type IV or mixed type II/IV. Hysteresis loop is also observable. It could be ascribed to type II hysteresis in according to IUPAC classification, indicating interconnected pores with variable dimension.

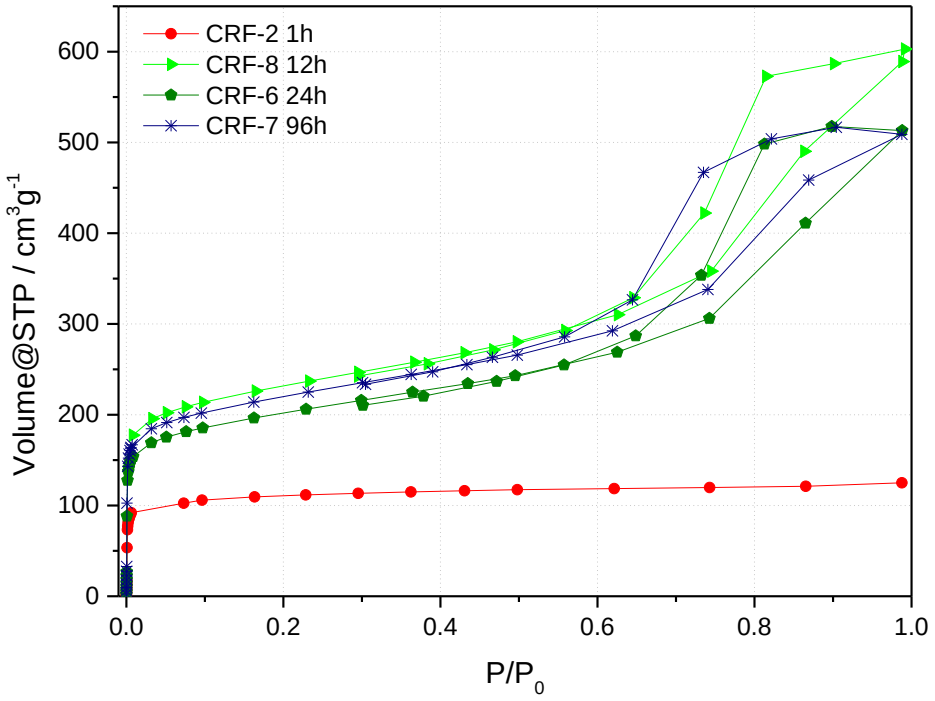

Figure 9.5 - Influence of heating time at 90 °C on N_2 physisorption at 77K.

Pore size distribution (PSD) plot as a function of 90 °C aging time is represented in figure 9.6. When subjected to 1 hour of heating treatment, carbon aerogel with PSD in the region of micropores was achieved. The rise of the aging time causes a shift to mesopores region. They show a wide range of pore width.

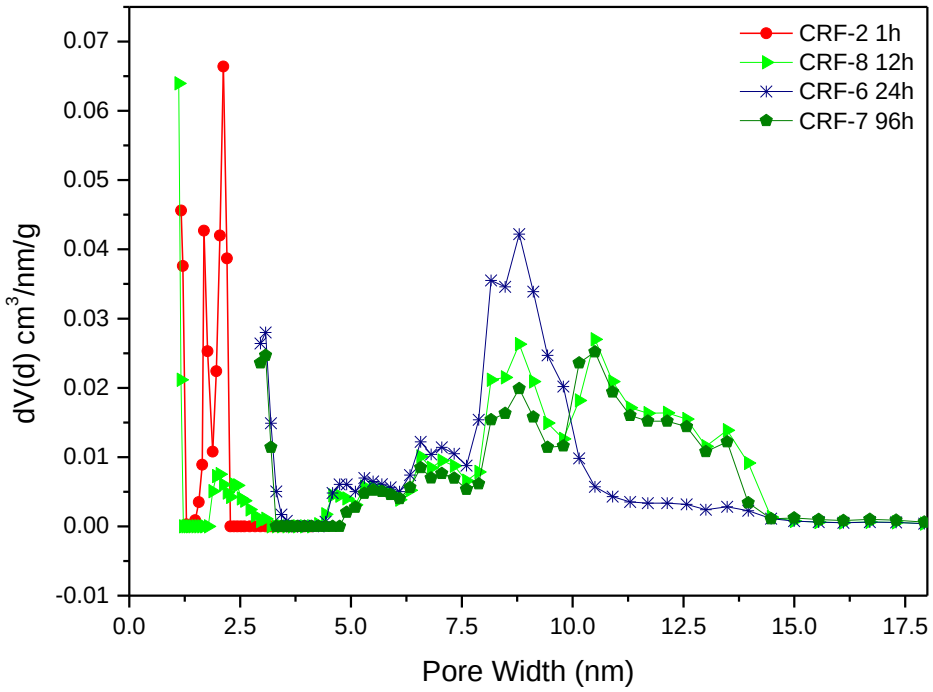

Figure 9.6 - Pore size distribution (PSD) calculated by DFT method of samples aged at 90 °C.

The complete data analysis is listed in table 9.3. 12 hours aging are necessary to obtain mesoporous carbon. Increase heating time over 12 hours produces only minor changes. In particular, microporous volume is not affected, surface area and mesoporous volume decrease slightly.

Table 9.3 - Porosity evaluation as function of time of thermal treatment.

	Gel Time (h)	**S_{BET} (m^2/g)**	**V_{tot} (cm^3/g)**	**V_{meso} (cm^3/g)**	**V_{micro} (cm^3/g)**
CRF-2	1	394	0.19	0.03	0.16
CRF-8	12	777	0.91	0.66	0.25
CRF-6	24	680	0.73	0.55	0.18
CRF-7	96	740	0.72	0.52	0.2

Resorcinol/Catalyst molar ratio (R/C) - Fixed the aging procedure as 90 °C for 12 hours, carbon with different R/C molar ratio have been prepared and porosity characteristics have been analyzed.

Figure 9.7 shows the evolution of porosity as a function of increased R/C molar ratio. Samples with higher amount of catalyst (lower R/C) are characterized by type I N_2 adsorption isotherms, suggesting microporosity prevalence.

On the contrary, decreasing catalyst quantity, isotherms become type IV, indicating development of mesoporosity and formation of larger nanopores. Application of theoretical models to curves, allowed to evaluate the effect of catalyst on porous structure as indicated in table 9.4.

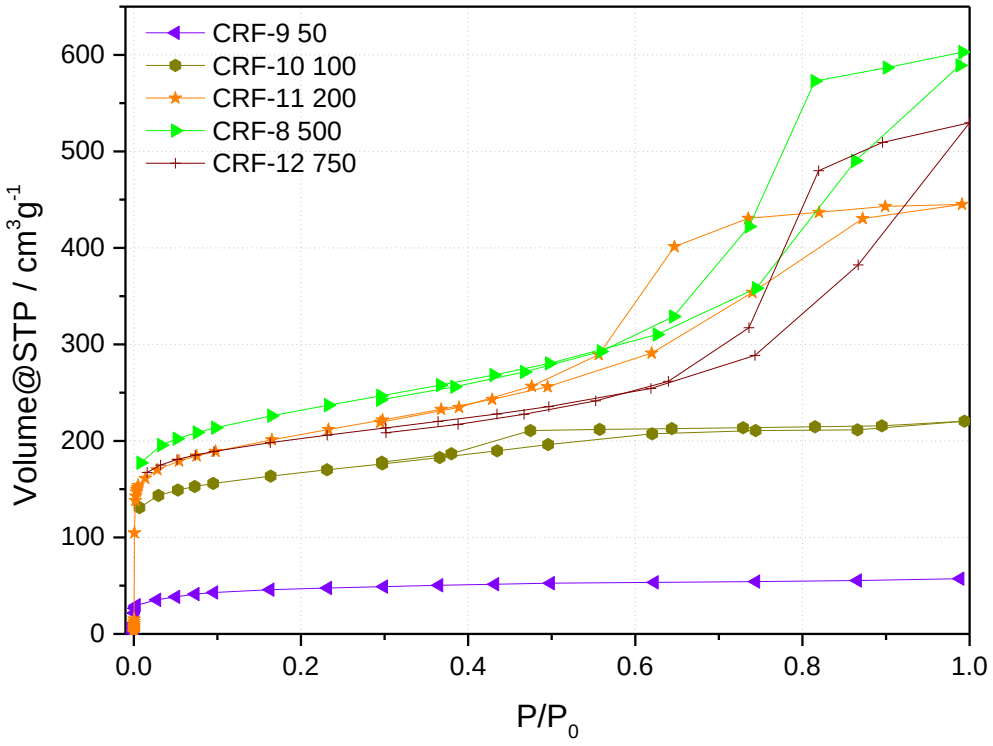

Figure 9.7 - Nitrogen adsorption isotherms as function of R/C molar ratio.

In order to have appreciable values of surface area and porous volume, R/C ratios higher than 100 are necessary. The higher value in terms of meso/microporous ratio and pore width is obtained using a R/C molar ratio equal to 500, like the sample CRF-8.

Table 9.4 - Comparison of porosity in the samples with different R/C, aged at 90° C for 12 hours.

	R/C	S_{BET} (m^2/g)	V_{tot} (cm^3/g)	V_{meso} (cm^3/g)	V_{micro} (cm^3/g)	Pores diameter (nm)
CRF-9	50	157	0.089	0.02	0.05	3.2
CRF-10	100	520	0.33	0.08	0.16	3.2
CRF-11	200	727	0.69	0.45	0.16	7
CRF-8	500	777	0.91	0.66	0.25	13
CRF-12	750	672	0.80	0.54	0.20	12

Resorcinol/Water molar ratio (R/W) - Finally, the effect of water on the synthesis has been taken in account. A sample with lower R/W has been synthesized: CRF-24, prepared using R/W molar ratio equal to 0.11. Physisorption isotherm is a mixed type II/IV isotherm (figure 9.8), related to meso-macroporous materials.

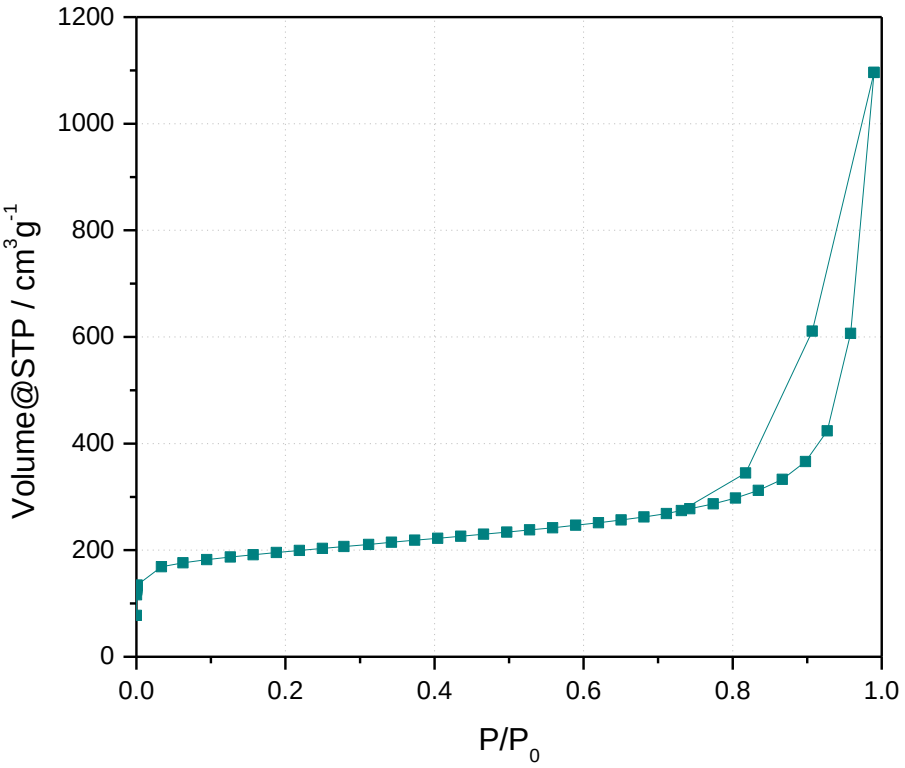

Figure 9.8 - Physisorption isotherm of CRF-24 sample.

As resumed in table 9.5, this sample shows the highest total porous volume (1.33 cm^3/g), mostly due to mesoporosity. The average pore width is increased too: 16 nm calculated by BJH method on desorption branch of isotherm. Conversely, R/W molar ratio does not affect significantly surface area.

Table 9.5 - Analysis of porosity for CRF-24 sample.

	R/W	**S_{BET} (m^2/g)**	**V_{tot} (cm^3/g)**	**V_{meso} (cm^3/g)**	**V_{micro} (cm^3/g)**
CRF-24	0.11	672	1.33	1.13	0.20

The above described experiments allowed to rationalize the aerogel synthesis and to choice the best condition to our purpose. Resuming data above:

- ✓ Gelation and aging steps greatly affect the final structure of carbon. Low temperature or aging time smaller than 12 hours, are insufficient to obtain a stable, cross-linked polymer network, which doesn't collapse during following steps. Poorly microporous carbon structure with a flat surface has been obtained in this case, as shown by scanning electronic micrographs in figure 9.9a and b. Typical "string of pearls" morphology can't be recognized in these samples. Conversely, CRF-8 in figure 9.9c exhibits porous structure consisting of spherical particles interconnected with open pores on the surface.
- ✓ The final structure of carbon aerogels depends on the size and number of resorcinol-formaldehyde clusters generated during the polymerization.
- ✓ R/C molar ratio is the principal parameter controlling the size of interconnected particles and thus the scale and size of pores in the final gel structure. Low R/C molar ratio corresponds to a poorly mesoporous carbon. Increased R/C molar ratio to 500 corresponds to high surface area and porous volume. In addition, also pore width is affected by this parameter.
- ✓ Amount of water in the initial mixture is another factor that plays crucial role in pore size distribution and porosity. Changing quantity of water during synthesis doesn't affect surface area, but rather mesoporosity and pore widths. Low R/W molar ratio is responsible of increased pores. Figure 9.9d show the micrographs of CRF-24, prepared with lower R/W molar ratio. In the same way as CRF-8, interconnected particles forming carbon structure are evident, but they exhibit larger pores.

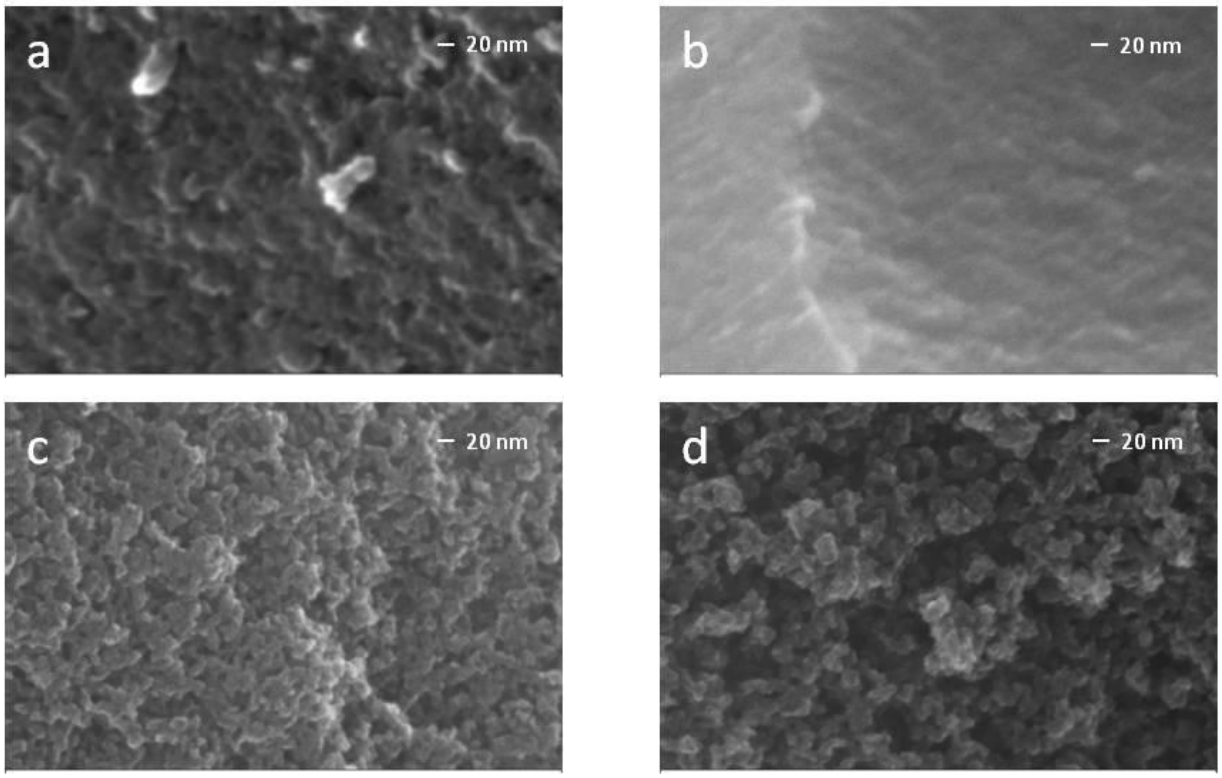

Figure 9.9 - SEM images of a) CRF-5, b) CRF-2, c) CRF-8 and d) CRF-24.

In order to infiltrate alanates into the carbon aerogel pores, the optimal condition is to have high mesoporous volume, with a pore size distribution close to 20-30 nm diameters. Therefore the matrix chosen was the CRF-24, synthesized with a R/W ratio equal to 0.11 through a single thermal treatment at 90 °C for 12h. This carbon aerogel has the highest total porous volume (1.33 cm^3/g, 85 % of which is mesoporosity) and largest pores (average pore size calculated with BJH method of 16 nm).

9.1-3 Infiltration of $NaAlH_4$ in Carbon Aerogel

In order to prepare $NaAlH_4$/Carbon nanocomposite, it was used a quantity of sodium alanate able to fill 50% of total porous volume of the carbon host, corresponding to a Carbon/$NaAlH_4$ weight ratio equal to 0.624/0.376.

Infiltration of hydride in carbon host has been carried out as follow: $NaAlH_4$ and carbon aerogel powders have been mixed in mortar, anhydrous tetrahydrofuran (THF) has been added dropwise to promote alanate dissolution and precipitation into the carbon pores. At the end, the mixture has been dried under vacuum for 5 hours to eliminate the solvent and allow the complete re-crystallization of $NaAlH_4$. $NaAlH_4$/Carbon nanocomposite obtained has been labeled as *si*. Furthermore, a sample prepared mixing the same dry quantities of $NaAlH_4$ and carbon aerogel with mortar has been used as control sample. The sample has been labeled as *ni*. Table 9.6 resumes the synthesized samples.

Table 9.6 - List of the samples under investigation

Sample	**CRF:$NaAlH_4$ molar weight**	**Preparation**
ni	0.624:0.376	Physical mixing
si	0.624:0.376	Solvent assisted impregnation

9.2 Physical-chemical characterization

The $NaAlH_4$/Carbon nanocomposite has been characterized by XRD, FTIR and TGA to get insights about the local structure and composition.

Figure 9.11 shows the diffraction patterns of samples before (*ni*) and after (*si*) infiltration. $NaAlH_4$ pristine has been used as reference. As expected, before infiltration crystallinity of $NaAlH_4$ is preserved, although peaks are considerably decreased in intensity. Once infiltrated (*si* sample), it's observable only a little peak at $2\theta = 29.7°$, which correspond to the (112) reflection of $NaAlH_4$. In addition, it can be noted the appearance of two reflections at $2\theta = 38.4°$ and 44.5° corresponding to (111) and (200) reflections of cubic Fm-3m aluminum. Probably, this is the result of partial decomposition of the alanate upon infiltration. As already observed in chapter 6, carbon has a catalytic effect on hydrogen desorption properties of alanates.

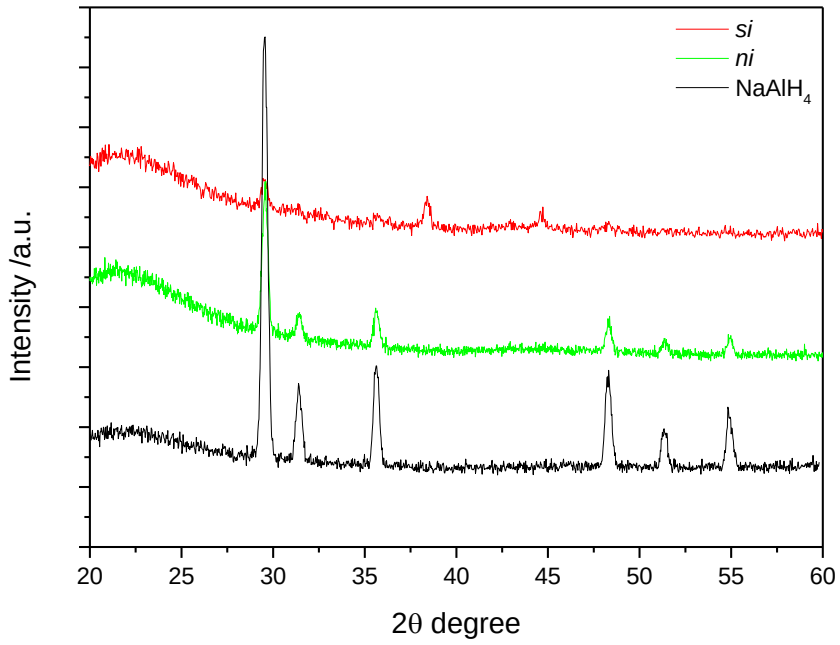

Figure 9.11 - XRD pattern of $NaAlH_4$ pristine (black), *ni* (green) and *si* (red) samples.

A collection of FTIR spectra of the samples is given in figure 12. FTIR analysis has been performed by the use of a Bruker Alpha spectrometer. All spectra have been recorded in the wave number range between 2000 and 400 cm^{-1}, in transmission mode, at room temperature. The samples, as fine powder, have been mixed with KBr in a 1:100 weight ratio (powder to KBr respectively) and then hand pressed in pellets by a Pike die set. FTIR assignment has been done by comparing with literature data [55].

CRF exhibits residual oxygenated functional group on the surface, deriving from an incomplete carbonization of the sample during the pyrolysis. At 1590 cm^{-1} is the typical asymmetric stretching mode of C=O groups. The broad peak at 1110 cm^{-1} with a shoulder at 1240 cm^{-1} corresponds to C-O stretching modes of methylene ether bridge and phenolic group, respectively. Sample *ni* exhibits typical vibrational modes of $NaAlH_4$. The peaks at 1675 and 1430 cm^{-1} and peaks at 904 and 743 cm^{-1} are associated to Al-H stretching and H-Al-H bending modes of $[AlH_4]^-$ group, respectively. Despite oxygenated functional groups in carbon aerogel, sodium alanate apparently doesn't interact with them upon simple grinding. Signals related to the carbon matrix are no evident due to their lower relative intensity. After infiltration (*si* sample), characteristic vibrational frequencies exhibited by $NaAlH_4$ are still observable. The peak at 1675 cm^{-1} due to Al-H stretching of $[AlH_4]^-$ group, which is very broad and intensive in pristine sample, is weak in *si* sample. $\delta[AlH_4]^-$ mode at 904 cm^{-1} is shifted to 877 cm^{-1} and the peak at 743 cm^{-1} is split at 727 and 693 cm^{-1}. In addition, also aluminum carboxylate frequencies are evident. C=O stretching modes are sensitive to the coordination of the aluminum atoms to oxygen, therefore asymmetrical and symmetrical C=O stretching modes located at 1587 and 1426 cm^{-1} confirm the occurred reaction between the $NaAlH_4$ and the carbon matrix to form aluminum complexes.

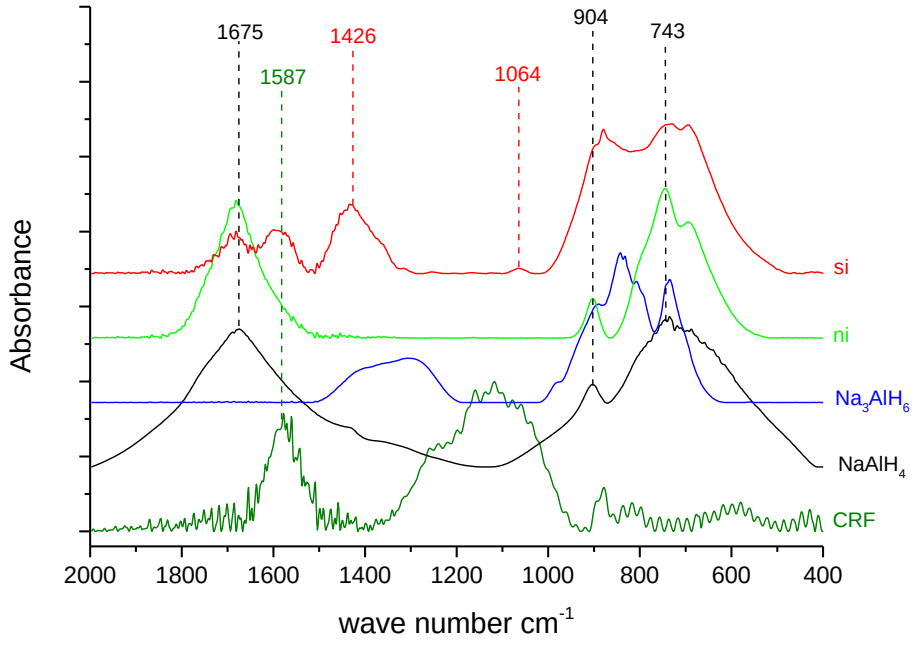

Figure 9.12 - FTIR spectra acquired in transmission mode of $NaAlH_4$/Carbon before and after infiltration. The spectra were referenced with CRF, $NaAlH_4$ and Na_3AlH_6 FTIR spectra.

In summary, the performed nanoconfinement of sodium alanate in carbon matrix is accompanied by their partial reaction and $NaAlH_4$ decomposition. Nevertheless it could produce a poorly crystalline $NaAlH_4$, strongly interacting with the carbon matrix, which characteristic spectroscopic signals, e.g. Al-H stretching, are still present, even if broadened and weakened.

The samples morphology, before and after infiltration, has been further analyzed by both Scanning Electronic Microscopy (SEM) and Transmission Electronic Microscopy (TEM), by using a LEO 130 HRSEM and transmission electron microscopy using a FEI Tecnaicryo-TEM instrument. Figure 9.13 shows the micrographs of *ni* and *si* samples. $NaAlH_4$ pristine and CRF are shown as reference materials. The CRF sample shows a large porosity (figure 9.13a-b). It consists of an open structure constituted by spherical particles, interconnected, with open pores on the surface. On the contrary, the pristine alanate sample (figure 9.13c-d) shows regular plate-like particles with variable dimensions in the range of 100nm-1μm. After hand grinding with CRF (*ni* sample, figure 9.13e-f), $NaAlH_4$ assumes stick-like shape. SEM images highlight that although the two component of the mixture, i.e. alanate and carbon matrix, are perfectly distinguishable, a certain interaction upon mixing occurs since the $NaAlH_4$ morphology is markedly altered. After infiltration, SEM image (*si* sample, figure 9.13g-h) reveals a homogeneous composite material: the alanate is deeply permeated into carbon support without evident phase separation. Moreover the superficial porosity of the host carbon appears to be decreased.

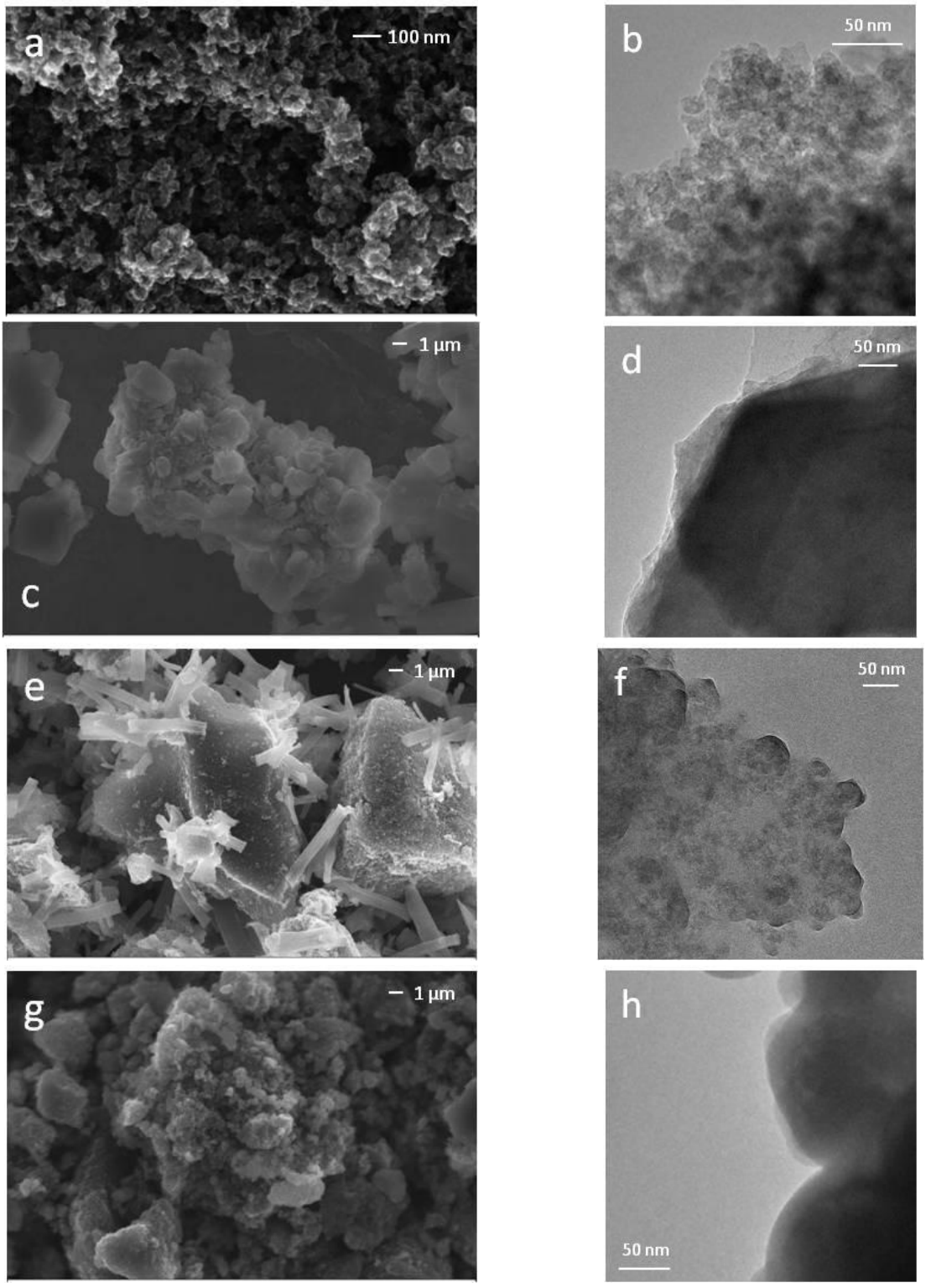

Figure 9.13 - Morphological analysis of a-b) CRF, c-d) $NaAlH_4$, e-f) *ni* and g-h) *si*. On the left there are SEM images, on the right TEM micrographs.

Finally, the net amount of $NaAlH_4$ after infiltration has been evaluated by thermogravimetric analysis (TGA). Thermal analysis was carried out in a Perkin Elmer diamond TGA/DTA. Samples were heated to 450 °C (5 °C/min) in Argon flow. Before temperature scan, in order to be sure to have eliminated residual THF from the *si* composite, the sample was kept at 50 °C in argon flow until equilibration of the weight.

Figure 9.14 shows the thermal desorption profiles of $NaAlH_4$ pristine, *ni* and *si* samples. The bulk sample releases approximately 7.2 wt.% H_2 at the end of the temperature scan through the expected multistep mechanism [89].

$$NaAlH_4 \leftrightarrows 1/3Na_3AlH_6 + 2/3Al + H_2 \qquad (1)$$

$$Na_3AlH_6 \leftrightarrows NaH + Al + 3/2H_2 \qquad (2)$$

$$NaH \leftrightarrows Na + 1/2H_2 \qquad (3)$$

The amount of H_2 released reaches almost the theoretical one (7.4 wt.% H_2 with respect of $NaAlH_4$): probably the starting material contains some traces of impurities. When mixed with CRF, hydrogen release shows a completely different thermal desorption profile. Sample *ni* starts to decompose at about 190 °C and proceed through a massive single step. At the end of temperature scan, 6.6 wt.% is loss from $NaAlH_4$, suggesting a hydrogen content decrease of 0.6 % after mixing with CRF. Probably, some of the hydrogen released upon heating reacts with the oxygenated groups in the carbon matrix and does not really leave the sample. In the case of *si* sample, weight losses start above 60-80 °C and continue in a featureless single smooth process. Up to 450 °C the hydrogen released from infiltrated sample is approximately 4 wt.% with respect to $NaAlH_4$ mass to be compared to the 6.6 wt.% of the sample before infiltration. This unexpected limited hydrogen loss can result from a larger oxidization upon infiltration beyond the expected amount originated by the intrinsic oxygen present in the carbon matrix (1.75 wt.%). It is possible that in the peculiar conditions realized for infiltration, when a saturated alanate solution is finely dispersed across an highly porous carbon, some hydrogen desorption can occur boosted by the well-known catalytic ability of nanocarbons [72,74,77]; moreover additional reactivity upon infiltration towards THF or its undetected impurities cannot be excluded. Nevertheless part of the infiltrated alanate is preserved and 54% of hydrogen is still available.

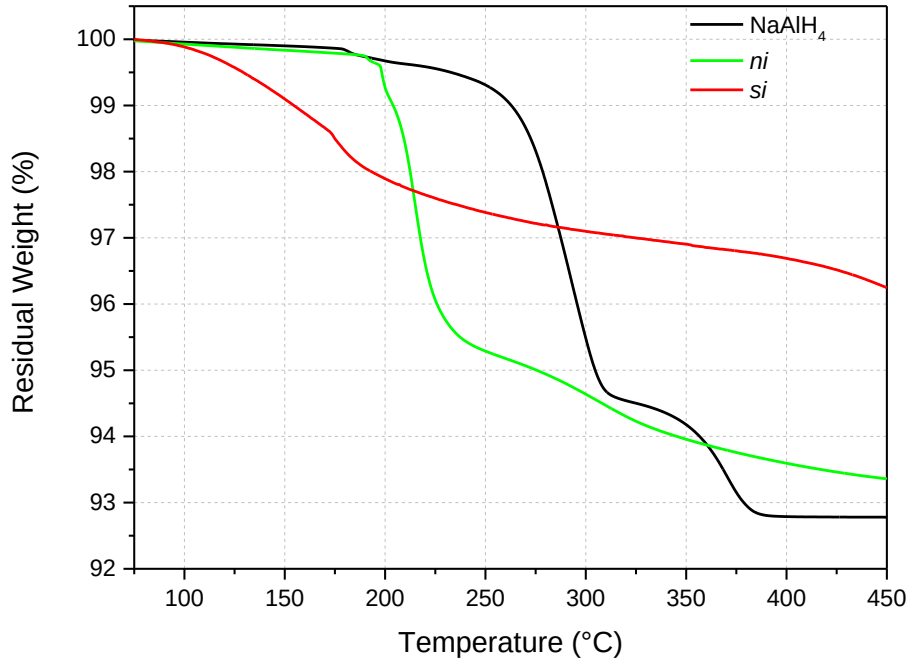

Figure 9.14. Thermogravimetric analysis of pristine $NaAlH_4$ (black), *ni* sample (green) and *si* sample (red) heated at 450 °C in Ar flow at 5 °C/min.

9.3 Electrochemical characterization

Electrochemical performance have been tested thanks to a Maccor battery cycler under galvanostatic condition in a voltage range of 0.01-2.5V and using a current density of 20 mA/g. Figure 9.15a reports the potential profiles of *ni* and *si* samples in comparison with pristine $NaAlH_4$ during a discharge/recharge cycle.

As described in chapter 6 pristine sodium alanate achieves almost 2200 $mAhg^{-1}$ during first discharge and the profile is characterized by three sloped plateau around 0.3, 0.25 and 0.12 V. Upon recharge oxidation proceeds in two steps around 0.4 and 0.5 V and the 35 % of the exchanged capacity is returned. When alanate is mixed with carbon aerogel, the total capacity exchanged at the end of discharge is lower, reaching approximately 500 and 1000 $mAhg^{-1}$ for *ni* and *si* samples, respectively. It is important to underline that the experimental capacities shown in figure 9.15 are normalized by the total mass of nanocomposite, including the CRF. Considering that the $NaAlH_4$:CRF weight ratio in the sample is about 0.37:0.64 and assuming a theoretical capacity of 1985 $mAhg^{-1}$ for $NaAlH_4$ and 200 $mAhg^{-1}$ for CRF [90], the expected theoretical capacity attributable to the $NaAlH_4$/CRF composite can be calculated as 862 $mAhg^{-1}$.

In the case of non infiltrated sample (*ni*), discharge evolves through three sloping plateau centered at 0.74, 0.32 and 0.2 V. Upon recharge just 38 % of developed capacity is returned and voltage profile is characterized by two slopes at 0.4 and 0.9 V. For infiltrated sample (*si*) reduction occurs in a similar way through three slopes centered at 0.74, 0.36 and 0.2 V; but, on the contrary, coulombic efficiency rises to 55 %, reaching 527 mAh/g at the end of first recharge through a two step process developing around 0.45 and 0.9 V. As evident in figure 9.15b, the exchanged capacity abruptly decreases upon the second cycle, even if the recharge efficiency markedly improves. Nevertheless despite the amount of cycled capacity is only a small percentage of the theoretical value, the composite can sustain cyclation differently from the bulk alanates that fails completely in few cycles.

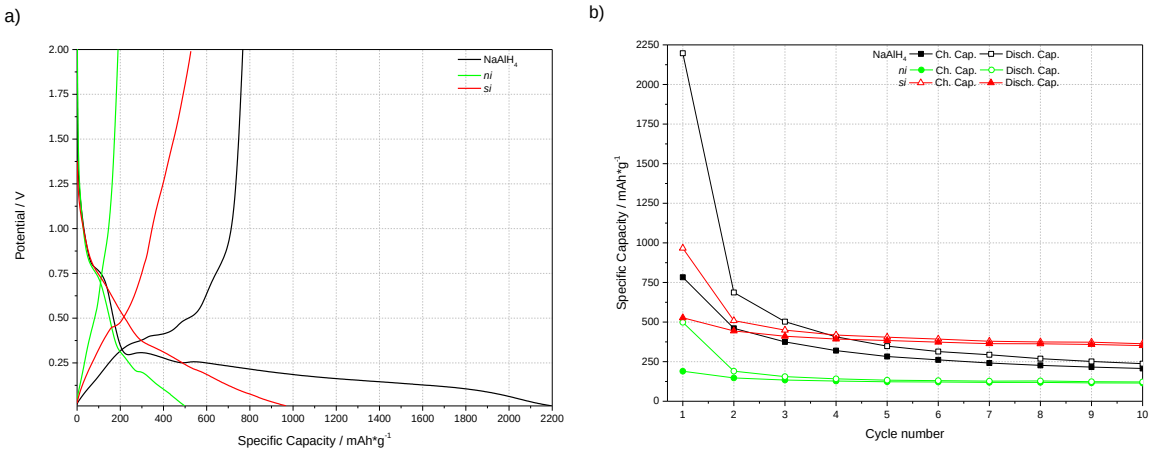

Figure 9.15 - a) Voltage-Specific Capacity profile of the first discharge/recharge and b) Specific Capacity versus Cycle number before (*ni*) and after infiltration (*si*). $NaAlH_4$ was used as reference.

9.4 Conclusions

A carbon aerogel has been used as host for alanate nanoparticles. In order to obtain the best condition for infiltration process, optimization of synthesis conditions has been carried out. As a result, a customized mesoporous carbon has been obtained consisting of spherical nanoparticles interconnected to form a nanoporous structure characterized by a total porous volume of 1.33 cm^3/g and pores of 16 nm diameters.

In order to improve the dispersion of particles into the carbon matrix, a solvent assisted method has been chosen. The result was a $NaAlH_4$/CRF nanocomposite with a homogeneous morphology consisting of alanate particles permeated into the carbon matrix. Nevertheless, the resulting nanoconfined material was highly reactive and therefore complex to manage: it easily burns upon exposure to air, and starts to desorbs hydrogen already below 100 °C. Furthermore, despite elemental analysis performed on carbon revealed just 1.75 wt.% of residual oxygen, the interactions between alanate and carbon are intensive and thermal analysis demonstrated that only 54% of the total alanate infiltrated was preserved after confinement. Although these issues, such nanocomposite demonstrated improved cyclability in a lithium cell. Apparently confinement is effective in reducing electrode pulverization following the huge volume variations to which the hydride is subjected upon lithium conversion.

In summary, alanate infiltration into a carbon aerogel appears to be a promising method to confine a hydrogen rich material capable to give a reversible conversion reaction in lithium cells. However, the optimization of the infiltration method is necessary in order to avoid the extensive decomposition of the sample. Probably, a solution could come from a better control of the solvent purity, carbon porosity, but especially from the possible grinding under reducing hydrogen atmosphere (by milling in close vials).

10

Effect of replacement of electrolyte with an ionic liquid

Another important aspect to consider in order to improve the electrochemical performance of alanates regards its chemical reactivity towards the common solvents used as electrolytes. In fact, it is well-known that alanates are strong reducing agents, typically used in organic chemistry for carbonyl reduction. Standard LP30 electrolyte used for electrochemical tests is based on alkyl carbonates, and thus, it may be easily reduced as soon as it comes into contact with the alanate electrode. For this purpose, in the previous chapters, the electrode/electrolyte interface of $LiAlH_4$ and $NaAlH_4$ has been studied by means of infrared spectroscopy and electrochemical impedance spectroscopy. Thanks to these measurements, the evidences of the formation of reduction products accumulated on the electrode surface as a result of its high chemical reactivity have been obtained. It means that a superficial film is formed on the electrode as cell is assembled, and before any electrochemical process occurs. This observation fits with the low OCV value of ball milled samples (LB1D05 and NB15D5) and with the absence of the signature of electrolyte decomposition typically observed around 0.8 V upon their discharge. Nevertheless, a different behavior has been observed with the two alanates: a stable superficial film is formed for $LiAlH_4$, able to prevent any further decomposition on the electrode surface, whereas the film formed on $NaAlH_4$ surface appears dynamic and in continuous evolution. It is worth noting that while reacting with the electrolyte, the alanate available for electrochemical conversion reaction is partially consumed.

Replacement of the LP30 with a carbonyl free electrolyte is therefore a strategy to be investigated in order to improve cell efficiency and performance in general. First attempts were made exchanging the carbonates with lower chemical reactive solvents as ethers. Unfortunately, this choice was not successful, due to high solubility of alanates in polar solvents as ethers. Therefore, it was considered to use a different type of electrolyte system as one based on an Ionic Liquid.

Ionic Liquids have attracted a lot of attention as electrolyte systems thanks to their high ionic conductivity, low toxicity as well as their high thermal, chemical and electrochemical stability [91].

For our purpose, it was chosen the N-*n*-butyl-N-methylpyrrolidinium hexafluorophosphate ($[Py_{14}]PF_6$), an Ionic Liquid consisting of an alkylmethylpyrrolidinium cation and the same anion PF_6^- contained in LP30. Specifically, $[Py_{14}]PF_6$ has been added at the standard electrolyte and three different mixtures have been prepared increasing the amount of IL from 30 to 70 wt.%. Table 10.1 reports the list of the solutions used for the study and the related properties. Then, such enriched IL solutions have been tested in a lithium cells using $NaAlH_4$ as working electrode and the effect on its performance has been evaluated. Previously studies [92] on 30% IL added solution demonstrated that it has better thermal and electrochemical properties than the pure LP30; also, the addition of ionic liquid can reduce the flammability of the volatile carbonates, improving the safety of the overall system.

Table 10.1 - Composition of the electrolyte.

Name	**LP30 wt.%**	**IL wt.%**	**$LiPF_6$ Molality**	**Ionic Conductivity σ_i/S*cm^{-1}**
LP30	100	/	0.87	$1.2\ 10^{-2}$
IL30	70	30	0.58	$2.8\ 10^{-2}$
IL50	50	50	0.41	$3.0\ 10^{-2}$
IL70	30	70	0.24	$1.9\ 10^{-2}$

10.1 Electrochemical performance

Electrochemical tests have been performed assembling two electrodes cells, following the procedure described in chapter 4. NB15D5 based electrodes and metallic lithium were working and counter electrodes, respectively. The three solutions described in table 1 have been used as electrolyte. Galvanostatic cyclations have been carried out by means of a Maccor Battery Tester, the voltage profiles have been acquired in the potential range of 2.5-0.01 V using a 100 mA/g current density.

Voltage profiles are reported in figure 10.1. Profile obtained with LP30 has been reported as reference. As evident, the total capacity exchanged at the end of first discharge decreases with the amount of ionic liquid present in the electrolyte, moving from 2010 $mAhg^{-1}$ with the pure LP30 to 840 $mAhg^{-1}$ with the addition of 70 wt.% of IL. However, despite differences in the total exchanged capacity values, first discharge profiles appear similar for the three solutions but all the processes are down shifted of 100-200 mV in relation with the increased amount of IL added to electrolyte. Such overvoltages can be originated from the lower conductivity and higher viscosity of solutions after the addition of IL that results in a slower Li^+ transference number.

Concerning charge profile, it's evident that the addition of ionic liquid has beneficial effects on the efficiency of the conversion process, that increases from 57% with LP30 to 94% with IL70 solution, see figure 10.2. Charge evolves through two plateaus around 0.4 and 0.8 V, similarly to the profile with LP30, but the addition of ionic liquid leads to an extension of the plateau around 0.8V. Interestingly, conversely to discharge process, charge is not affected by larger overvoltages.

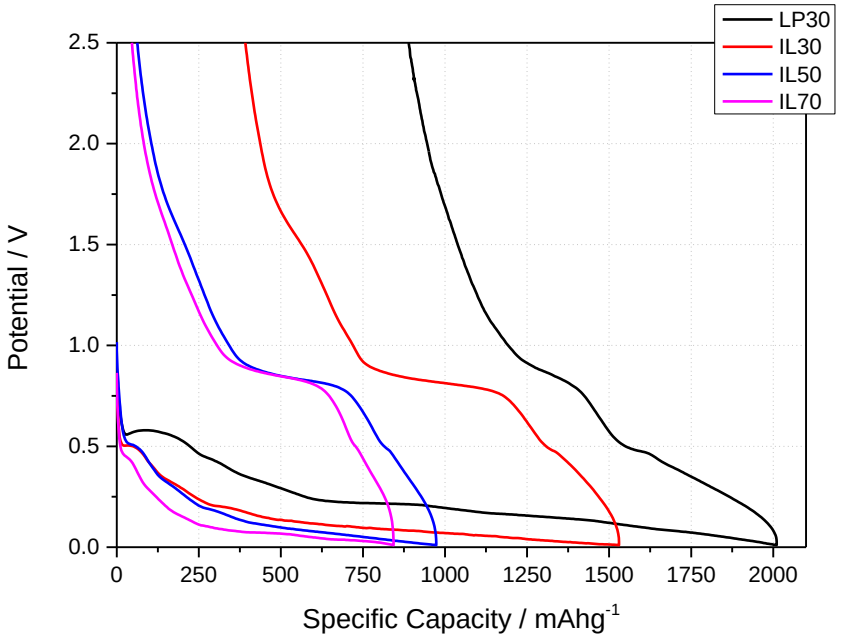

Figure 10.1 - First discharge/charge voltage profiles obtained in galvanostatic mode as function of amount of ionic liquid into the electrolyte. Results obtained with LP30 are used as reference.

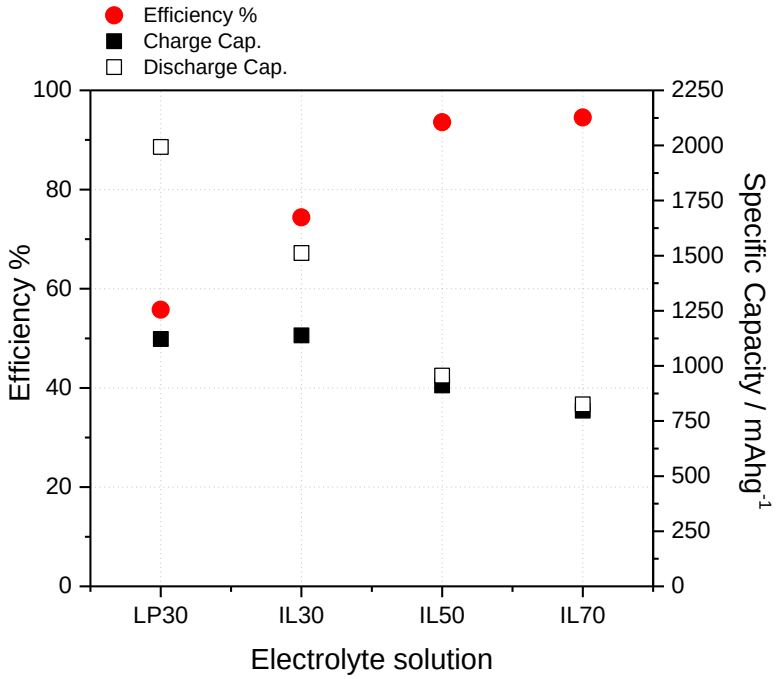

Figure 10.2 - Efficiency and Specific Capacity as function of electrolyte solution plot for the sample NB15D5.

Finally, the cyclability of sodium alanate with the three solutions has been considered. Figure 10.3 shows the specific capacity as function of cycle number obtained in a lithium cell, with the IL solutions as electrolyte compared with LP30. As evident from the figure, the first cycle efficiency improvement does not turn in any significant cycle life extension.

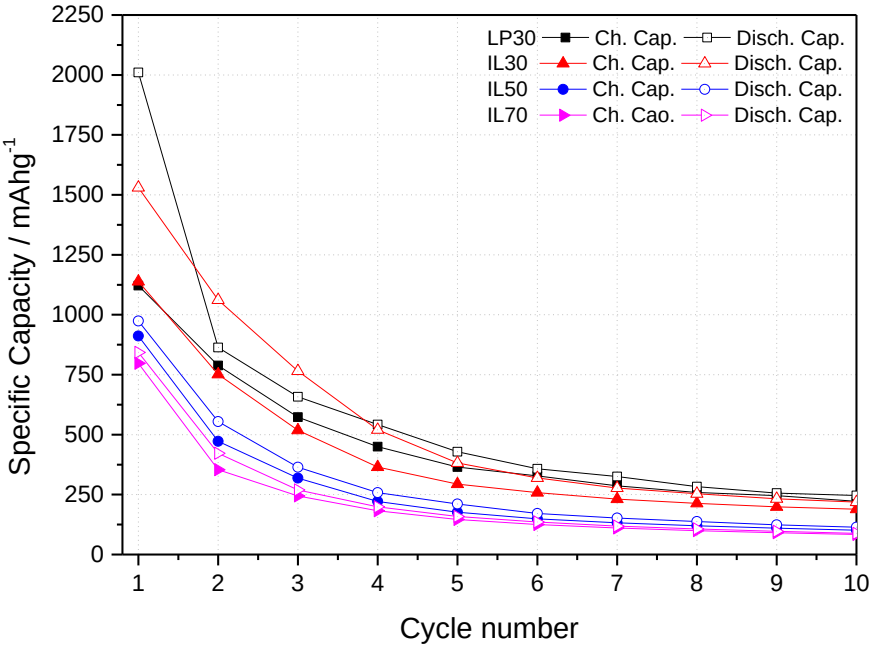

Figure 10.3 - Specific capacity vs. cycle number for NB15D5 electrodes using the three ionic liquid added solutions. LP30 has been reported as reference.

10.2 Surface reactivity

The effects of replacement of LP30 with ionic liquid on surface reactivity have been studied by electrochemical impedance spectroscopy. Following the same procedure described in chapter 4, the spectra were collected at OCV during a week.

Figure 10.4 reports the Nyquist plot of sodium alanate electrode in contact with the IL30 solution. A simple R(RQ)(RQ)Q equivalent circuit can be used to describe the observed impedance responses. The sequence describes a not blocking interface. At t=0 impedance curve is characterized by a semicircle in the high frequencies region associated to the SEI presence, followed by a large semicircle at mid frequencies relative to the electrodic process and finally a convoluted line at low frequencies. Upon time, the resistance associated with SEI constantly increases from 2 to 43 Ω. In the same way, charge transfer resistance increases from hundreds to a thousand ohm, while the final linear trend, probably indicative of a diffusion kinetics limitation, do not basically change upon time.

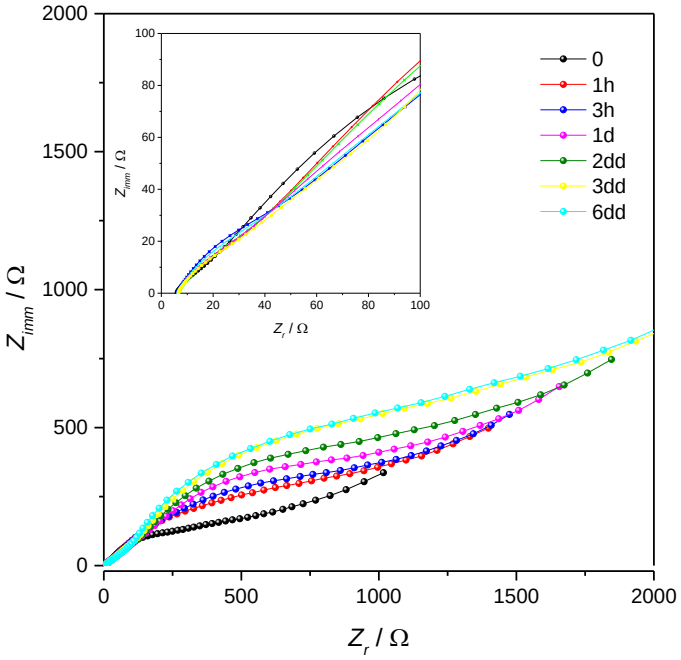

Figure 10.4 - Nyquist plots of NB15D5 sample using IL30 solution as electrolyte.

In summary, these measurements confirmed that the replacement of carbonates based electrolyte with an ionic liquid produce beneficial effects on the film formation process. This is clearly showed in figure 10.5, in which the R_{SEI} as function of time in the IL30 solution has been compared with LP30. In the case of plain alkylcarbonate based electrolyte, a 30Q

resistive film is quickly formed and is therefore subject to continuous fluctuations. Conversely the IL30 solution showed small initial R_{SEI} values that continuously increase upon time. After 1 day, such growth becomes lower and the R_{SEI} settle on 30 Ω. Anyway, the trend observed in R_{SEI} reveals that alanate still reacts largely with electrolyte but the resistivity and the instability of the SEI appears to be reduced.

Finally, the chemical nature of the interaction between alanate and IL added solution has been investigated acquiring infrared spectra in ATR mode of an electrode upon aging. Figure 10.6 reports results obtained with aging NB15D5 electrode in IL30 solution. As occurring for an LP30 soaked electrode and described in chapter 6, the electrode's surface is enriched by reduction products resulting from electrolyte decomposition. But in contrast with the experiments performed with pure LP30, the film increases gradually upon time. Specifically, after 10 minutes of aging there is the appearance of the vibrational modes related to fluoro-alkyl phosphates at 850 cm^{-1} and the Al-O bending at 650 cm^{-1}. These signals constantly increase in intensity and after prolonged time of aging it's observable also the stretching modes of P=O group at 1160 cm^{-1} and P=O-R group at 976 and 780 cm^{-1} while the intensity of peak at 850 cm^{-1} largely increase. Furthermore, stretching frequencies related to deposition of organic lithium carbonates are clearly visible at 1806, 1773 and 1306 cm^{-1}, while the C-O stretching is at 1080 cm^{-1}.

After the addition of ionic liquid, the interaction between alanate and carbonates is still high, as evident from the several products deposited on electrode surface. Anyway, the diluting with an unreactive species allows the formation of a more stable film.

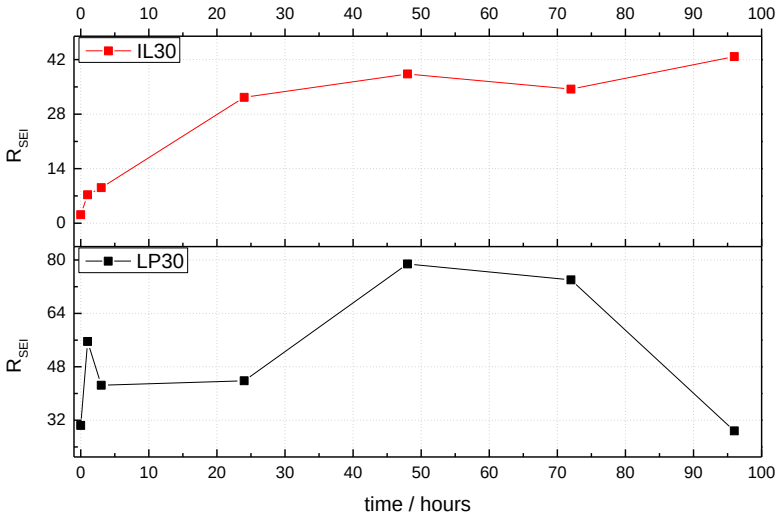

Figure 10.5 - RSEI as function of time for IL30 in comparison with LP30 was used as reference. The data have been obtained by fitting the impedance spectra with an equivalent circuit R(RQ)(RQ)Q.

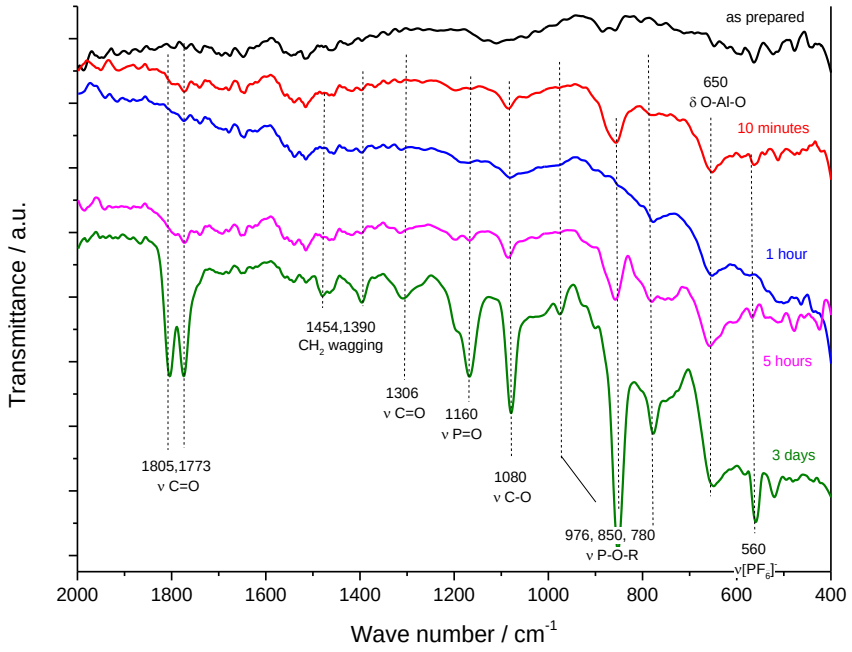

Figure 10.6 - FTIR-ATR spectra of NB15D5 upon aging in IL30 solution.

10.3 Conclusions

Increased amounts of $[Py_{14}]PF_6$ have been added to LP30 electrolyte in order to reduce the high chemical reactivity between the carbonates solution and alanates. This leads to improvements on charge efficiency of sodium alanate, though the overall capacities decrease in relation with the amounts of IL in the solutions.

Following the approach used previously, the electrode/electrolyte interface between the IL30 solution and sodium alanate has been studied by means of electrochemical impedance spectroscopy and infrared spectroscopy. From these measurements, it's evident the formation of a more stable superficial film. However, reduction products are continuously deposited on the electrode surface.

The addition of Ionic Liquid doesn't block the reactivity of alanate with the residual carbonates in the solution but the process is slower. This evidence demonstrates that the choice of an appropriate electrolyte is an important factor for the correct functioning of sodium alanate in a lithium device. Anyway, more studies addressed to develop an electrolyte with low chemical reactivity but still allowing a high ionic conduction are necessary.

Final remarks

Alanates have been proposed as a new class of materials for use as high capacity anodes for lithium ion batteries. The fundamental aspects of lithium and sodium alanate electrochemistry in lithium cell were reported for the first time and results discussed in relation to their structure and morphology. A plethora of experimental technique have been used to support the discussion, powder and electrodes x-ray diffraction (ex and in situ), FTIR spectroscopy, solid state NMR, electrochemical potentiodynamic and galvanostatic methods, electrochemical impedance spectroscopy.

The study was mainly focused on tetrahydro-alluminates $LiAlH_4$ and $NaAlH_4$. Thanks to their advantageous properties including the light molar weight and high gravimetric hydrogen densities, they are theoretically able to exchange at least 3 electrons per redox center developing high capacities values, i.e. 1985 $mAhg^{-1}$ for $NaAlH_4$ and 2119 $mAhg^{-1}$ for $LiAlH_4$. Furthermore, thermal analysis demonstrated that these compounds release hydrogen only when temperature exceeds 180 °C, make them feasible candidates for practical application in lithium devices.

In addition to these compounds, also the Li- and Na- hexa-hydrides (Li_3AlH_6 and Na_3AlH_6) and the mixed $LiNa_2AlH_6$ were taken into account. Beside their high capacities values, these compounds were important elements to have a better insight of the electrochemical behavior of the corresponding tetrahydro-alluminates. For instance, it's well known that the thermal desorption mechanism proceeds through a multistep process involving their formation. In a similar way, computational studies highlighted the occurrence of conversion processes for alanates following a similar route.

Starting from these theoretical considerations, experimental evidences of their electrochemical activity were produced. Both Li- and Na-alanates proved to be redox active. Electrochemically driven lithium incorporation proceeds through a complex conversion mechanism, involving the formation of hexa-alanates intermediates compounds before the complete reduction to the elemental metals. As regards of $LiAlH_4$, the discharge is characterized by three plateaus at 0.78 V, 0.27 V and 0.15 V vs. Li. Conversion resembles the thermal desorption process and involves the formation of Li_3AlH_6, followed by the complete reduction to LiH and Al.

A more complex mechanism was found for $NaAlH_4$ that include the formation either of Na_3AlH_6 and the mixed $LiNa_2AlH_6$ hexa-alanates as intermediates that directly reduce to the elemental metals. The $NaAlH_4$ discharge develops over three plateaus identified near 0.41,

0.26 and 0.17V vs. Li respectively, for an overall capacity of 1700-1800 $mAhg^{-1}$. Also, for both samples further alloying reaction between lithium and aluminum cannot be excluded at deepest lithium loading. Finally, reverse reaction proceeds along the same intermediate products and it occurs through a two-step process completely reversible for $NaAlH_4$ evolving around 0.40 and 0.47 V vs. Li. While, in the case of $LiAlH_4$ charge occurs through two plateaus at 0.44 and 0.80V vs. Li but it was only partially reversible.

The operative potentials of alanates are of great interest in order to envisage their application in a high energy lithium ion battery.

However, for both the samples efficiency is poor and less than 30% and 16% of the exchanged capacity is recovered upon charge in Na and Li alanate, respectively. Commonly to other conversion materials, the observed voltage profiles of alanates are characterized by a large initial irreversible capacity and poor cycle life stability. The main factors contributing to such drawbacks include: i) the structural rearrangements intrinsic in the conversion mechanism, that results in electrode pulverization and loss of electric contact, ii) the incomplete de-conversion due to the low conductivity of the compounds emerging from reduction, and iii) parasitic processes like irreversible or non-electrochemical electrolyte decomposition and sodium stripping upon oxidation. Kinetics limitations could even be at the origin of the observed incomplete reversibility of $LiAlH_4$.

First attempts to improve the electrochemical performance of these materials were done by the use of mechanochemical treatments. Ball milling was used both to reduce the alanates particle size and coat the obtained nanometric powders with a conductive carbon.

Large improvements in alanates recharge efficiency were achieved. In the case of sodium alanate, 15 hours of ball milling followed by an additional step of 5 hours grinding with carbon led to an enhanced recharge efficiency reaching 70%. On the contrary, prolonged ball milling of $LiAlH_4$ with carbon results in a complete decomposition of the sample. Anyway, a shorter mechanochemical step allows improving $LiAlH_4$ recharge efficiency to 39%.

Although mechanochemistry demonstrated to improve reversibility of the conversion process, still capacity drastically fades in few cycles. Further and more decisive technological improvements are needed to overcome the above mentioned problems. Therefore, strategies aimed to limit the volume changes upon conversion and reduce the chemical reactivity with the electrolyte were here approached. In view of the encouraging results obtained with sodium alanate, demonstrating either a complete reversibility of conversion reaction as well as high efficiency of the electrochemical process, the further optimizations was focused on $NaAlH_4$.

First strategy was addressed to the minimization of the impact of electrode volume variation during lithium incorporation/de-incorporation. For this purpose, sodium alanate was infiltrated in an optimized mesoporous carbon scaffold by the use of a solvent assisted method. The result was a $NaAlH_4$/CRF nanocomposite consisting of alanate particles homogeneously permeated into the carbon matrix. Nevertheless, alanate was subjected to a partial decomposition upon infiltration. As a consequence, electrochemical tests revealed limited exchanged capacity compared with the pristine material. But, contrarily to the latter, the nanoconfined alanate can sustain cyclation for several cycles, improving the cycle life stability of alanate.

A further route for improvement that has been attempted was the mitigation of the alanate/electrolyte interaction by replacing carbonates-based electrolyte with an ionic liquid. Experimental evidences demonstrated an extensive reactivity between ball milled sodium alanate and the standard electrolyte LP30. As consequence, an unstable superficial film deriving from the decomposition of electrolyte was deposited on electrode surface. The addition of a less reactive compound in the electrolyte solutions demonstrated to influence positively the electrochemical performance, leading to an increasing of reversibility up to 94% in relation with the amounts of ionic liquid in the solution.

In conclusion, this work demonstrated that alanates undergo to high capacity, reversible electrochemical conversion processes, suitable to be conveniently exploited in the negative compartment of a lithium ion battery. Technological problems limiting the processes efficiency and electrodes cycle life have been highlighted as well as possible strategies to solve them.

Bibliography

[1] F. M. Courtel, H. Duncan, and Y. Abu-Lebdeh, "Beyond Intercalation: Nanoscale-Enabled Conversion Anode Materials for Lithium-Ion Batteries," in *Nanotechnology for Lithium-Ion Batteries*, pp. 85–116, 2012.

[2] B. Scrosati and J. Garche, "Lithium batteries: Status, prospects and future," *J. Power Sources*, vol. 195, no. 9, pp. 2419–2430, 2010.

[3] J. M. Tarascon and M. Armand, "Issues and challenges facing rechargeable lithium batteries," *Nature*, vol. 414, no. 6861, pp. 359–367, 2001.

[4] P. G. Bruce, B. Scrosati, and J. M. Tarascon, "Nanomaterials for Rechargeable Lithium Batteries," *Angew. Chem. Int. Ed.*, vol. 47, no. 16, pp. 2930–2946, 2008.

[5] P. Poizot, S. Laruelle, S. Grugeon, L. Dupont, and J. M. Tarascon, "Nano-sized transition-metal oxides as negative-electrode materials for lithium-ion batteries," *Nature*, vol. 407, no. 6803, pp. 496–499, 2000.

[6] P. Poizot, S. Laruelle, S. Grugeon, and J. M. Tarascon, "Rationalization of the Low-Potential Reactivity of 3d-Metal-Based Inorganic Compounds toward Li," *J. Electrochem. Soc.*, vol. 149, no. 9, pp. A1212–A1217, 2002.

[7] N. Pereira, L. Dupont, J. M. Tarascon, L. C. Klein, and G. G. Amatucci, "Electrochemistry of Cu_3N with Lithium: A Complex System with Parallel Processes," *J. Electrochem. Soc.*, vol. 150, no. 9, pp. A1273–A1280, 2003.

[8] H. Li, G. Richter, and J. Maier, "Reversible Formation and Decomposition of LiF Clusters Using Transition Metal Fluorides as Precursors and Their Application in Rechargeable Li Batteries," *Adv. Mater.*, vol. 15, no. 9, pp. 736–739, 2003.

[9] Y. Wang, Z. W. Fu, X. L. Yue, and Q.-Z. Qin, "Electrochemical Reactivity Mechanism of Ni_3N with Lithium," *J. Electrochem. Soc.*, vol. 151, no. 4, pp. E162–E167, 2004.

[10] D. C. C. Silva, O. Crosnier, G. Ouvrard, J. Greedan, A. Safa-Sefat, and L. F. Nazar, "Reversible Lithium Uptake by FeP_2," *Electrochem. Solid-State Lett.*, vol. 6, no. 8, pp. A162–A165, 2003.

[11] J. Cabana, L. Monconduit, D. Larcher, and M. R. Palacín, "Beyond Intercalation-Based Li-Ion Batteries: The State of the Art and Challenges of Electrode Materials Reacting Through Conversion Reactions," *Adv. Mater.*, vol. 22, no. 35, pp. E170–E192, 2010.

[12] A. S. Aricò, P. Bruce, B. Scrosati, J. M. Tarascon, and W. van Schalkwijk, "Nanostructured materials for advanced energy conversion and storage devices," *Nat. Mater.*, vol. 4, no. 5, pp. 366–377, 2005.

[13] R. Khatib, A. L. Dalverny, M. Saubanere, M. Gaberscek, and M. L. Doublet, "Origin of the Voltage Hysteresis in the CoP Conversion Material for Li-Ion Batteries," *J. Phys. Chem. C*, vol. 117, no. 2, pp. 837–849, 2013.

[14] L. Li, R. Jacobs, P. Gao, L. Gan, F. Wang, D. Morgan, and S. Jin, "Origins of Large Voltage Hysteresis in High-Energy-Density Metal Fluoride Lithium-Ion Battery Conversion Electrodes," *J. Am. Chem. Soc.*, vol. 138, no. 8, pp. 2838–2848, 2016.

[15] D. Meggiolaro, G. Gigli, A. Paolone, P. Reale, M. L. Doublet, and S. Brutti, "Origin of the Voltage Hysteresis of MgH_2 Electrodes in Lithium Batteries," *J. Phys. Chem. C*, vol. 119, no. 30, pp. 17044–17052, 2015.

[16] Y. Oumellal, A. Rougier, G. A. Nazri, J. M. Tarascon, and L. Aymard, "Metal hydrides for lithium-ion batteries," *Nat. Mater.*, vol. 7, no. 11, pp. 916–921, 2008.

[17] S. Brutti, G. Mulas, E. Piciollo, S. Panero, and P. Reale, "Magnesium hydride as a high capacity negative electrode for lithium ion batteries," *J. Mater. Chem.*, vol. 22, no. 29, pp. 14531–14537, 2012.

[18] Y. Oumellal, A. Rougier, J. M. Tarascon, and L. Aymard, "2LiH + M (M = Mg, Ti): New concept of negative electrode for rechargeable lithium-ion batteries," *J. Power Sources*, vol. 192, no. 2, pp. 698–702, 2009.

[19] Y. Oumellal, C. Zlotea, S. Bastide, C. Cachet-Vivier, E. Léonel, S. Sengmany, E. Leroy, L. Aymard, J. P. Bonnet, and M. Latroche, "Bottom-up preparation of MgH_2 nanoparticles with enhanced cycle life stability during electrochemical conversion in Li-ion batteries," *Nanoscale*, vol. 6, no. 23, pp. 14459–14466, 2014.

[20] Y. Oumellal, W. Zaïdi, J. P. Bonnet, F. Cuevas, M. Latroche, J. Zhang, J. L. Bobet, A. Rougier, L. Aymard, "Reactivity of TiH_2 hydride with lithium ion: Evidence for a new conversion mechanism," *Int. J. Hydrog. Energy*, vol. 37, no. 9, pp. 7831–7835, 2012.

[21] S. Sartori, F. Cuevas, and M. Latroche, "Metal hydrides used as negative electrode materials for Li-ion batteries," *Appl. Phys. A*, vol. 122, no. 2, pp. 1–7, 2016.

[22] F. M. Vitucci, A. Paolone, S. Brutti, D. Munaò, L. Silvestri, S. Panero, P. Reale., "H_2 thermal desorption and hydride conversion reactions in Li cells of TiH_2/C amorphous nanocomposites," *J. Alloys Compd.*, vol. 645, Supplement 1, pp. S46–S50, 2015.

[23] D. Meggiolaro, L. Farina, L. Silvestri, S. Panero, S. Brutti, and P. Reale, "Lightweight Borohydrides Electro-Activity in Lithium Cells," *Energies*, vol. 9, no. 4, p. 238, 2016.

[24] J. A. Teprovich Jr., J. Zhang, H. Colon-Mercado, F. Cuevas, B. Peters, S. Greenway, R. Zidan, and M. Latroche, "Li-Driven Electrochemical Conversion Reaction of AlH_3, $LiAlH_4$, and $NaAlH_4$," *J. Phys. Chem. C*, vol. 119, no. 9, pp. 4666–4674, 2015.

[25] L. Silvestri, S. Forgia, L. Farina, D. Meggiolaro, S. Panero, A. La Barbera, S. Brutti, and P. Reale, "Lithium Alanates as Negative Electrodes in Lithium-Ion Batteries," *ChemElectroChem*, vol. 2, no. 6, pp. 877–886, 2015.

[26] L. Silvestri, L. Farina, D. Meggiolaro, S. Panero, F. Padella, S. Brutti, and P. Reale, "Reactivity of Sodium Alanates in Lithium Batteries," *J. Phys. Chem. C*, vol. 119, no. 52, pp. 28766–28775, 2015.

[27] L. Cirrincione, L. Silvestri, C. Mallia, P. E. Stallworth, S. Greenbaum, S. Brutti, S. Panero, and P. Reale, "Investigation of the Effects of Mechanochemical Treatment on

$NaAlH_4$ Based Anode Materials for Li-Ion Batteries," *J. Electrochem. Soc.*, vol. 163, no. 13, pp. A2628–A2635, 2016.

[28] V. P. Tarasov and G. A. Kirakosyan, "Aluminohydrides: Structures, NMR, solid-state reactions," *Russ. J. Inorg. Chem.*, vol. 53, no. 13, pp. 2048–2081, 2008.

[29] R. Zidan, "Aluminum Hydride (Alane)," in *Handbook of Hydrogen Storage*, M. Hirscher, Ed. Wiley-VCH Verlag GmbH & Co. KGaA, 2010, pp. 249–277.

[30] A. E. Finholt, A. C. Bond, and H. I. Schlesinger, "Lithium Aluminum Hydride, Aluminum Hydride and Lithium Gallium Hydride, and Some of their Applications in Organic and Inorganic Chemistry1," *J. Am. Chem. Soc.*, vol. 69, no. 5, pp. 1199–1203, 1947.

[31] R. Ehrlich, A. R. Young, G. Rice, J. Dvorak, P. Shapiro, and H. F. Smith, "The Chemistry of Alane. XI.1 A New Complex Lithium Aluminum Hydride, Li_3AlH_6," *J. Am. Chem. Soc.*, vol. 88, no. 4, pp. 858–860, 1966.

[32] N. Sklar and B. Post, "Crystal structure of lithium aluminum hydride," *Inorg. Chem.*, vol. 6, no. 4, pp. 669–671, 1967.

[33] B. C. Hauback, H. W. Brinks, and H. Fjellvåg, "Accurate structure of $LiAlD_4$ studied by combined powder neutron and X-ray diffraction," *J. Alloys Compd.*, vol. 346, no. 1–2, pp. 184–189, 2002.

[34] I. P. Jain, P. Jain, and A. Jain, "Novel hydrogen storage materials: A review of lightweight complex hydrides," *J. Alloys Compd.*, vol. 503, no. 2, pp. 303–339, 2010.

[35] H. W. Brinks and B. C. Hauback, "The structure of Li_3AlD_6," *J. Alloys Compd.*, vol. 354, no. 1–2, pp. 143–147, 2003.

[36] A. E. Finholt, E. C. Jacobson, A. E. Ogard, and P. Thompson, "Organic Reductions by Sodium Aluminum Hydride," *J. Am. Chem. Soc.*, vol. 77, no. 15, pp. 4163–4163, Aug. 1955.

[37] E. C. Ashby and P. Kobetz, "The Direct Synthesis of Na_3AlH_6," *Inorg. Chem.*, vol. 5, no. 9, pp. 1615–1617, 1966.

[38] J. W. Lauher, D. Dougherty, and P. J. Herley, "Sodium tetrahydroaluminate," *Acta Crystallogr. B*, vol. 35, no. 6, pp. 1454–1456, 1979.

[39] Bel'skii, V. K., Bulychev, B. M., and Golubeva, A. V, "A redetermination of the structure of $NaAlH_4$.," *Zhurnal Neorganicheskoi Khimii*, pp. 1528–1529, 1983.

[40] B. C. Hauback, H. W. Brinks, C. M. Jensen, K. Murphy, and A. J. Maeland, "Neutron diffraction structure determination of $NaAlD_4$," *J. Alloys Compd.*, vol. 358, no. 1–2, pp. 142–145, 2003.

[41] E. Rönnebro, D. Noréus, K. Kadir, A. Reiser, and B. Bogdanovic, "Investigation of the perovskite related structures of $NaMgH_3$, $NaMgF_3$ and Na_3AlH_6," *J. Alloys Compd.*, vol. 299, no. 1–2, pp. 101–106, 2000.

[42] B. Bogdanović, R. A. Brand, A. Marjanović, M. Schwickardi, and J. Tölle, “Metal-doped sodium aluminium hydrides as potential new hydrogen storage materials,” *J. Alloys Compd.*, vol. 302, no. 1–2, pp. 36–58, 2000.

[43] B. Sakintuna, F. Lamari-Darkrim, and M. Hirscher, “Metal hydride materials for solid hydrogen storage: A review,” *Int. J. Hydrog. Energy*, vol. 32, no. 9, pp. 1121–1140, 2007.

[44] T. N. Dymova, D. P. Aleksandrov, V. N. Konoplev, T. A. Silina, and A. S. Sizareva, *Russ. J. Coord. Chem.*, vol. 20, pp. 263–268, 1994.

[45] B. Bogdanović and M. Schwickardi, “Ti-doped alkali metal aluminium hydrides as potential novel reversible hydrogen storage materials1,” *J. Alloys Compd.*, vol. 253–254, pp. 1–9, 1997.

[46] P. Claudy, B. Bonnetot, J. P. Bastide, and L. Jean-Marie, “Reactions of lithium and sodium aluminium hydride with sodium or lithium hydride. Preparation of a new alumino-hydride of lithium and sodium $LiNa_2AlH_6$,” *Mater. Res. Bull.*, vol. 17, no. 12, pp. 1499–1504, 1982.

[47] H. W. Brinks, B. C. Hauback, C. M. Jensen, and R. Zidan, “Synthesis and crystal structure of Na_2LiAlD_6,” *J. Alloys Compd.*, vol. 392, no. 1–2, pp. 27–30, 2005.

[48] S. Orimo, Y. Nakamori, J. R. Eliseo, A. Züttel, and C. M. Jensen, “Complex Hydrides for Hydrogen Storage,” *Chem. Rev.*, vol. 107, no. 10, pp. 4111–4132, 2007.

[49] O. M. Løvvik and O. Swang, “Structure and stability of possible new alanates,” *Europhys. Lett. EPL*, vol. 67, no. 4, pp. 607–613, 2004.

[50] J. Graetz, Y. Lee, J. J. Reilly, S. Park, and T. Vogt, “Structure and Thermodynamics of the Mixed Alkali Alanates,” *Phys. Rev. B*, vol. 71, no. 18, 2005.

[51] L. Lutterotti, S. Matthies, H. R. Wenk, A. S. Schultz, and J. W. R. Jr, “Combined texture and structure analysis of deformed limestone from time-of-flight neutron diffraction spectra,” *J. Appl. Phys.*, vol. 81, no. 2, pp. 594–600, 1997.

[52] BAM Berlin PowderCell

[53] O. M. Løvvik, S. M. Opalka, H. W. Brinks, and B. C. Hauback, “Crystal structure and thermodynamic stability of the lithium alanates $LiAlH_4$ and Li_3AlH_6,” *Phys. Rev. B*, vol. 69, no. 13, p. 134117, 2004.

[54] J. R. Ares Fernandez, F. Aguey-Zinsou, M. Elsaesser, X. Z. Ma, M. Dornheim, T. Klassen, R. Bormann, “Mechanical and thermal decomposition of with metal halides,” *Int. J. Hydrog. Energy*, vol. 32, no. 8, pp. 1033–1040, 2007.

[55] J. C. Bureau, Z. Amri, P. Claudy, and J. M. Létoffé, “Etude comparative des hexahydrido-et des hexadeuteridoaluminates de lithium et de sodium. I - Spectres raman et infrarouge de Li_3- et Na_3AlH_6, et Li_3AlD_6,” *Mater. Res. Bull.*, vol. 24, no. 1, pp. 23–31, 1989.

[56] P. Verma, P. Maire, and P. Novák, “A review of the features and analyses of the solid electrolyte interphase in Li-ion batteries,” *Electrochimica Acta*, vol. 55, no. 22, pp. 6332–6341, 2010.

[57] “Infrared Spectral Interpretation: A Systematic Approach,” *CRC Press*, 1998.

[58] R. M. Silverstein, F. X. Webster, D. J. Kiemle, and D. L. Bryce, *Spectrometric Identification of Organic Compounds*. John Wiley & Sons, 2014.

[59] G. S. Groenewold, C. M. Leavitt, R. P. Dain, J. Oomens, J. D. Steill, and M. J. van Stipdonk, “Infrared spectrum of potassium-cationized triethylphosphate generated using tandem mass spectrometry and infrared multiple photon dissociation,” *Rapid Commun. Mass Spectrom.*, vol. 23, no. 17, pp. 2706–2710, 2009.

[60] S. Brutti, V. Gentili, H. Menard, B. Scrosati, and P. G. Bruce, “TiO_2-(B) Nanotubes as Anodes for Lithium Batteries: Origin and Mitigation of Irreversible Capacity,” *Adv. Energy Mater.*, vol. 2, no. 3, pp. 322–327, 2012.

[61] R. Katamreddy, R. Inman, G. Jursich, A. Soulet, and C. Takoudis, “ALD and Characterization of Aluminum Oxide Deposited on Si(100) using Tris(diethylamino) Aluminum and Water Vapor,” *J. Electrochem. Soc.*, vol. 153, no. 10, pp. C701–C706, 2006.

[62] T. Ikegami, W. S. Lee, H. Nariai, and T. Takeuchi, “Covalent molecular imprinting of bisphenol A using its diesters followed by the reductive cleavage with $LiAlH_4$,” *J. Chromatogr. B*, vol. 804, no. 1, pp. 197–201, 2004.

[63] W. E. Bachmann and A. S. Dreiding, “Reduction of a Diester to a Hydroxyester by Lithium Aluminum Hydride. Application to the Construction of Rings,” *J. Am. Chem. Soc.*, vol. 71, no. 9, pp. 3222–3223, 1949.

[64] D. Aurbach, “Review of selected electrode–solution interactions which determine the performance of Li and Li ion batteries,” *J. Power Sources*, vol. 89, no. 2, pp. 206–218, 2000.

[65] S. C. Chung and H. Morioka, “Thermochemistry and crystal structures of lithium, sodium and potassium alanates as determined by ab initio simulations,” *J. Alloys Compd.*, vol. 372, no. 1–2, pp. 92–96, 2004.

[66] D. Massiot *et al.*, “Modelling one- and two-dimensional solid-state NMR spectra,” *Magn. Reson. Chem.*, vol. 40, no. 1, pp. 70–76, 2002.

[67] P. Vajeeston, P. Ravindran, R. Vidya, H. Fjellvåg, and A. Kjekshus, “Pressure-induced phase of $NaAlH_4$: A potential candidate for hydrogen storage?,” *Appl. Phys. Lett.*, vol. 82, no. 14, pp. 2257–2259, 2003.

[68] M. H. W. Verkuijlen, P. J. M. van Bentum, E. R. H. van Eck, W. Lohstroh, M. Fichtner, and A. P. M. Kentgens, “Wide-Line Solid-State NMR Characterizations of Sodium Alanates,” *J. Phys. Chem. C*, vol. 113, no. 34, pp. 15467–15472, 2009.

[69] C. M. Jensen and K. J. Gross, “Development of catalytically enhanced sodium aluminum hydride as a hydrogen-storage material,” *Appl. Phys. A*, vol. 72, no. 2, pp. 213–219, 2001.

[70] P. Adelhelm and P. E. de Jongh, “The impact of carbon materials on the hydrogen storage properties of light metal hydrides,” *J. Mater. Chem.*, vol. 21, no. 8, pp. 2417–2427, 2011.

[71] Z. Dehouche, L. Lafi, N. Grimard, J. Goyette, and R. Chahine, “The catalytic effect of single-wall carbon nanotubes on the hydrogen sorption properties of sodium alanates,” *Nanotechnology*, vol. 16, no. 4, p. 402, 2005.

[72] A. Zaluska, L. Zaluski, and J. O. Ström-Olsen, “Sodium alanates for reversible hydrogen storage,” *J. Alloys Compd.*, vol. 298, no. 1–2, pp. 125–134, 2000.

[73] P. A. Berseth, A. G. Harter, R. Zidan, A. Blomqvist, C. M. Araújo, R. H. Scheicher, R. Ahuja, and P. Jena “Carbon Nanomaterials as Catalysts for Hydrogen Uptake and Release in $NaAlH_4$,” *Nano Lett.*, vol. 9, no. 4, pp. 1501–1505, 2009.

[74] C. Cento, P. Gislon, M. Bilgili, A. Masci, Q. Zheng, and P. P. Prosini, “How carbon affects hydrogen desorption in $NaAlH_4$ and Ti-doped $NaAlH_4$,” *J. Alloys Compd.*, vol. 437, no. 1–2, pp. 360–366, 2007.

[75] S. Gomes, G. Renaudin, H. Hagemann, K. Yvon, M. P. Sulic, and C. M. Jensen, “Effects of milling, doping and cycling of $NaAlH_4$ studied by vibrational spectroscopy and X-ray diffraction,” *J. Alloys Compd.*, vol. 390, no. 1–2, pp. 305–313, 2005.

[76] J. W. Akitt, “Multinuclear studies of aluminium compounds,” *Prog. Nucl. Magn. Reson. Spectrosc.*, vol. 21, no. 1–2, pp. 1–149, 1989.

[77] T. K. Nielsen, M. Polanski, D. Zasada, P. Javadian, F. Besenbacher, J. Bystrzycki, J. Skibsted, and T. R. Jensen, “Improved Hydrogen Storage Kinetics of Nanoconfined $NaAlH_4$ Catalyzed with $TiCl_3$ Nanoparticles,” *ACS Nano*, vol. 5, no. 5, pp. 4056–4064, 2011.

[78] F. Schüth, “Encapsulation Strategies in Energy Conversion Materials,” *Chem. Mater.*, vol. 26, no. 1, pp. 423–434, 2014.

[79] M. Winter and J. O. Besenhard, “Electrochemical lithiation of tin and tin-based intermetallics and composites,” *Electrochimica Acta*, vol. 45, no. 1–2, pp. 31–50, 1999.

[80] M. Christian and K. F. Aguey-Zinsou, “Destabilization of complex hydrides through size effects,” *Nanoscale*, vol. 2, no. 12, p. 2587, 2010.

[81] S. a. Al-Muhtaseb and J. A. Ritter, “Preparation and Properties of Resorcinol–Formaldehyde Organic and Carbon Gels,” *Adv. Mater.*, vol. 15, no. 2, pp. 101–114, 2003.

[82] M. Mirzaeian and P. J. Hall, “The control of porosity at nano scale in resorcinol formaldehyde carbon aerogels,” *J. Mater. Sci.*, vol. 44, no. 10, pp. 2705–2713, 2009.

[83] Y. Tao, M. Endo, and K. Kaneko, “A Review of Synthesis and Nanopore Structures of Organic Polymer Aerogels and Carbon Aerogels,” *Recent Pat. Chem. Eng.*, vol. 1, no. 3, pp. 192–200, 2008.

[84] H. Tamon, H. Ishizaka, T. Araki, and M. Okazaki, “Control of mesoporous structure of organic and carbon aerogels,” *Carbon*, vol. 36, no. 9, pp. 1257–1262, 1998.

[85] R. W. Pekala, “Organic aerogels from the polycondensation of resorcinol with formaldehyde,” *J. Mat. Chemistry*, col. 24, no. 9, pp 3221–3227, 1989.

[86] S. Brunauer, P. H. Emmett, and E. Teller, “Adsorption of Gases in Multimolecular Layers,” *J. Am. Chem. Soc.*, vol. 60, no. 2, pp. 309–319, 1938.

[87] B. C. Lippens and J. H. de Boer, “Studies on pore systems in catalysts: V. The t method,” *J. Catal.*, vol. 4, no. 3, pp. 319–323, 1965.

[88] E. P. Barrett, L. G. Joyner, and P. P. Halenda, “The Determination of Pore Volume and Area Distributions in Porous Substances. I. Computations from Nitrogen Isotherms,” *J. Am. Chem. Soc.*, vol. 73, no. 1, pp. 373–380, 1951.

[89] J. A. Dilts and E. C. Ashby, “Thermal decomposition of complex metal hydrides,” *Inorg. Chem.*, vol. 11, no. 6, pp. 1230–1236, 1972.

[90] “A Fe_2O_3 nanoparticle/carbon aerogel composite for use as an anode material for lithium ion batteries,” *Electrochimica Acta*, vol. 97, pp. 271–277, 2013.

[91] D. R. MacFarlane, N. Tachikawa, M. Forsyth, J. M. Pringle, P. C. Howlett, G. D. Elliott, J. H. Davis Jr., M. Watanabe, P. Simon, and C. A. Angell, “Energy applications of ionic liquids,” *Energy Environ. Sci.*, vol. 7, no. 1, pp. 232–250, 2013.

[92] A. Tsurumaki, M. A. Navarra, S. Panero, B. Scrosati, and H. Ohno, “N-n-Butyl-N-methylpyrrolidinium hexafluorophosphate-added electrolyte solutions and membranes for lithium-secondary batteries,” *J. Power Sources*, vol. 233, pp. 104–109, 2013.

Acknowledgements

This work has been carried out with the financial support of FIRB-Futuro in ricerca 2010 "*Hydrides as high capacity anodes for lithium ion batteries"*, granted by Italian Minister for University and Research.

I would like to thank my supervisor prof. Stefania Panero for giving me the opportunity to work in her research group. I was pleased to work in a such stimulating and challenging environment.

A special thank is due to dr. Priscilla Reale for her guidance and support during all my PhD, helping me in my professional growth and not only for that.

Further thank goes to dr. Sergio Brutti for the stimulating discussions and valuable suggestions and to all "hydrides" group, for bravely cooperating in the intensive way we did.

Finally, I would like to acknowledge all the researchers from the laboratory of Materials Chemistry and Technologies at ENEA, Research Center of Casaccia and prof. Steven Greenbaum and his collaborators from Hunter College of CUNY in New York (USA), who gave me the opportunity to visit and work in their laboratories.